An amplitude analysis of the $\pi^0\pi^0$ system produced in radiative J/ψ decays

Jake Vernon Bennett

Submitted to the faculty of the University Graduate School
in partial fulfillment of the requirements for the degree
Doctor of Philosophy
in the Department of Physics,
Indiana University
April 2014

Accepted by the Graduate Faculty, Indiana University, in partial fulfillment of the requirements for the degree of Doctor of Philosophy.

Doctoral Committee

Matthew Shepherd (Chair)

Ryan Mitchell

Adam Szczepaniak

April 28, 2014

Rick Van Kooten

For my children, who light up my life.

May you never stop discovering.

Acknowledgements

This work would never have been possible without the support of many people.

Beyond anything else, the love of my family has been the greatest support throughout all of my endeavors. Without this firm foundation, I could never have hoped to achieve what I have. There has never been a time in my life that I have not known that my parents, especially, are for me. Whatever I do, I know I can count on them for guidance and support. I do not think they will even realize how much of a blessing that has been.

My wife, Laura, deserves not only her own paragraph, but her own chapter. She more than anyone else has given me the support that allows me to put my all into everything I do. She has struggled with me as I overcame all of the trials and tribulations of graduate school and has never retreated from any of the roadblocks we have had to face. More than anything else, though, I must thank her for our beautiful children.

Like Newton and as with all scientific endeavors, my achievements are only possible because I have stood on the shoulders of giants. Matt Shepherd, my advisor, has given me guidance and support when I needed it most and allowed me to struggle and overcome the challenges that make me stronger as an experimentalist. I am constantly surprised by his depth and breadth of knowledge and I am truly thankful for all of his support. Likewise, the support I have received from Ryan Mitchell, who initiated me into the field of particle physics, has been invaluable. They both deserve and have my deepest thanks.

I would also like to offer thanks for the guidance given by Adam Szczepaniak, who made significant contributions to this work, and Rick Van Kooten, who has supported me in all of my endeavors at IU. Thanks are also due to Curtis Meyer, Adam Maltese, Peng Guo, Mihajlo Kornicer, Kei Moriya, and all of the other researchers at IU and beyond who have given me aid and friendship. Special thanks are also due to Jenny Stevens, Jordan Tillett and the rest of the Swain Hall staff. Operations would quickly fall apart without their efforts and expertise and I have relied upon their help many times.

A well balanced life necessitates a release from its stresses. My graduate studies would have been much less enjoyable without my classmates. Not only that, but my work would have suffered as well. Nick Timme and Jason Fry deserve particular mention. I know the friendships we developed will survive far beyond our time as graduate students. I would also like to thank Lance Garrison, Brad Schaefer, Dan Bennett, Manual Lara, and all of my other classmates for their support. Additionally, I would like to thank Pastor Woelmer and my family at the University Lutheran Church for their prayers and support.

While all of these people have dedicated enormous amounts of time and effort to helping me succeed in my graduate studies, it is only by the grace of God that I can do anything. All the glory is His alone.

Biographical Sketch

Jake was born on September 27, 1985 in Kirkland Lake, Ontario, Canada. He and his family immigrated to the United States in 1986. Jake attended Rockbridge County High School in Lexington, Virginia, where he was first introduced to research. As a high school junior, he joined Dr. David Sukow in the physics department at Washington and Lee University to study the effect of induced chaos in semiconductor diode lasers. In 2004, with his interest piqued and his high school diploma in hand, Jake set out to earn a degree in physics at Roanoke College in Salem, Virginia.

The four years Jake spent at Roanoke College were the formative years of his research career. He performed several different research projects on topics including the mathematics of a tennis serve and the growth and synthesis of carbon nanotubes. Jake would graduate as valedictorian with a B.S. in physics and mathematics in 2008. In the summer before his senior year at Roanoke, Jake joined Matthew Shepherd and Ryan Mitchell at Cornell University as part of a research experience for undergraduates. It was this project that set his feet on the path of experimental elementary particle physics and drove him to join Shepherd and Mitchell at Indiana University.

As a graduate student at IU, Jake performed hardware and data analyses under the guidance of his advisor, Matt Shepherd. These projects included a study of the timing characteristics of the forward electromagnetic calorimeter of the GlueX detector and an amplitude analysis of simulated GlueX data on the $\pi^+\pi^-\pi^+$ system. Jake earned an M.S. in physics from Indiana University in 2009. Soon thereafter, Jake would begin the dissertation work presented here. Upon receiving his Ph.D. in physics in 2014, Jake will begin a postdoctoral position at Carnegie Mellon University.

Jake was married to his high school sweetheart, Laura, in 2006. They have two daughters. Natalie was born in January 2012 and Elaina in March 2014.

Jake Vernon Bennett

AN AMPLITUDE ANALYSIS OF THE $\pi^0\pi^0$ SYSTEM PRODUCED IN RADIATIVE J/ψ DECAYS

Despite many years of study, a complete understanding of the interactions of quarks and gluons within hadronic states remains elusive. Quantum Chromodynamics (QCD) has long predicted the possibility of states in which gluonic excitations can contribute to the characteristics of the state (a hybrid) or even take the place of constituent quarks altogether (a glueball), yet no incontrovertible evidence yet exists. This is partially due to the nature of the low mass spectrum, in which broad, overlapping states make experimental methods challenging. Recent technological improvements and high statistics data sets now enable a rigorous study of regions in which experimentalists may perform fundamental tests of QCD. This dissertation presents one such study, focusing on the $\pi^0\pi^0$ spectrum. Particular emphasis is placed on the scalar meson spectrum ($J^{PC} = 0^{++}$), wherein the lightest glueball state is expected.

An amplitude analysis of the $\pi^0\pi^0$ system produced in radiative J/ψ decays is presented. A mass independent analysis of the $(1.3106 \pm 0.0072) \times 10^9$ J/ψ decays collected by the BESIII detector at BEPCII in Beijing, China is repeated under different model assumptions and experimental conditions. Additionally, the branching ratio of radiative J/ψ decays to $\pi^0\pi^0$ is measured to be $(1.147 \pm 0.002 \pm 0.042) \times 10^{-3}$, where the first error is statistical and the second is systematic. This is the first measurement of this reaction.

Matthew Shepherd(Chair)

Ryan Mitchell

Adam Szczepaniak

Rick Van Kooten

Contents

Acknowledgements **v**

Biographical Sketch **vii**

Abstract **vii**

1 Motivation **1**

2 Theoretical Background **6**

2.1 Standard model hadrons 7
2.1.1 Classification 7
2.1.2 Quantum Chromodynamics 12
2.2 The $\pi^0\pi^0$ System 13
2.2.1 The $f_0(500)$ (σ) 14
2.2.2 The $f_0(980)$ 15
2.2.3 The $f_0(1370)$ 15
2.2.4 The $f_0(1500)$ 16
2.2.5 The $f_0(1710)$ 16
2.2.6 Higher mass scalar states 17
2.2.7 Tensor states 17
2.2.8 Spin 4 states 17
2.3 Production Mechanism 18

3 Experimental Apparatus **20**

3.1 The BEPCII Accelerator 21
3.2 Introduction to the BESIII Detector 22
3.3 Charged Particle Tracking 23
3.3.1 The Solenoid Magnet 24
3.3.2 The Main Drift Chamber 25
3.4 Particle Identification 27
3.4.1 The Time of Flight System 27
3.4.2 The Muon System 29
3.5 Calorimetry 30
3.5.1 The Electromagnetic Calorimeter 30
3.6 Data Summary 32

4 Experimental Methods **34**
4.1 The Reconstruction Software . . . 35
4.2 Detector Simulation . . . 35
4.3 Extracting the Reconstructed Data . . . 36
4.4 Event Selection Criteria . . . 38
4.4.1 Optimization . . . 38
4.4.2 Background Analysis . . . 50

5 Amplitude Analysis **58**
5.1 Introduction to Amplitude Analyses . . . 58
5.2 The Mass Independent Amplitude Analysis . . . 64
5.2.1 Mass Binning . . . 67
5.2.2 The Radiative Multipole Basis . . . 67
5.3 Ambiguities in the Amplitude Analysis . . . 70
5.3.1 Trivial Ambiguities . . . 70
5.3.2 Non-trivial Ambiguities . . . 71
5.4 The Mass Dependent Amplitude Analysis . . . 71

6 Results **76**
6.1 Branching Ratio . . . 76
6.1.1 Branching Ratio Systematic Uncertainties . . . 77
6.1.2 Branching Ratio Results . . . 80
6.2 Mass Independent Analysis Results . . . 81
6.2.1 Mass Independent Fit Projections . . . 83
6.2.2 Nominal Results . . . 86
6.2.3 Permutations . . . 90
6.2.4 Alternate Results 1 . . . 95
6.2.5 Alternate Results 2 . . . 98
6.2.6 Discussion . . . 98
6.2.7 Error analysis . . . 102
6.3 Mass Dependent Analysis Results . . . 105
6.3.1 Adding an $f_0(980)$ . . . 111

7 Systematic Uncertainties **116**
7.1 Normalization . . . 117
7.1.1 Photon detection efficiency systematic uncertainties . . . 117
7.1.2 Kinematic fit . . . 123
7.1.3 Misreconstructed backgrounds . . . 124
7.2 Correlated systematic uncertainties . . . 129
7.2.1 Model dependencies in the mass independent analysis . . . 129
7.2.2 Background subtraction . . . 129
7.2.3 Cross check: $\omega\pi^0$ background . . . 129
7.2.4 Cross check: 4^{++} amplitude . . . 131

8 Conclusions **142**

A Ambiguities **150**

B Input-Output Study **159**
B.1 Single Resonance 159
B.2 Two Resonances 163
B.3 Full IO Study 163

C Photon Detection Efficiency **167**
C.1 Event Selection 168
C.2 Fitting Methods 173
C.2.1 Method 1 173
C.2.2 Method 2 174
C.3 Results 174
C.3.1 Energy and Anglular Distributions 175
C.3.2 MC Consistency Check 183
C.4 Conclusions 187

List of Tables

2.1 The quantum numbers of quarks. 9
2.2 The naming scheme for neutral flavor mesons [1]. 11

4.1 The number of events remaining after each signal isolation criterion . 50

6.1 This table summarizes the systematic uncertainties (in %) for the branching ratio of $J/\psi \to \gamma\pi^0\pi^0$. 81
6.2 The characteristics of the resonances from the mass dependent fit . . 107
6.3 The significances of the resonances in the mass dependent fit 108
6.4 The characteristics of the resonances from the mass dependent fit . . 111

C.1 The photon detection efficiency as calculated by global fits over all photon energies and angles 174
C.2 The combined results for the photon detection efficiency from fits in bins of photon energy 176
C.3 The combined results for the photon detection efficiency from fits in bins of photon angle 176
C.4 The results for the photon detection efficiency for fits with different background shapes and angular acceptance windows 183

List of Figures

2.1 A graphical representation of the light quark nonet with states labeled by their quark content. 10
2.2 A graphical representation of the (a) radiative decay and the (b) three gluon decays of the J/ψ meson. 19

3.1 A schematic representation of BEPCII 22
3.2 A schematic representation of the BESIII detector 24
3.3 A schematic representation of the MDC 26
3.4 A schematic representation of the TOF 28
3.5 A schematic representation of the MUC 29
3.6 A schematic representation of the EMC 31

4.1 The $\pi^0\pi^0$ invariant mass spectrum after minimal event selection criteria are applied 39
4.2 The χ^2 distribution from the 6C kinematic fit after minimal event selection criteria are applied 41
4.3 The χ^2 distribution (log scale) from the 6C kinematic fit before any event selection criteria are applied 42
4.4 The Dalitz-like plot after the selection criteria on the 6C kinematic fit χ^2 43
4.5 The $\gamma\pi^0$ invariant mass distribution 44
4.6 The invariant mass distribution of the radiative photon paired with one of the π^0 daughter photons 45
4.7 The generated versus reconstructed mass of the pair of π^0s from the inclusive MC sample 46
4.8 The signal efficiency of the selection criteria on the radiative photon according to an exclusive MC sample 47
4.9 The $\pi^0\pi^0$ invariant mass spectrum after all event selection criteria have been applied 48
4.10 The efficiency as a function of $\pi^0\pi^0$ invariant mass 49
4.11 The combined data set with $\gamma\eta(')$ backgrounds from an exclusive MC sample 51
4.12 The distribution of continuum events that pass the selection criteria . 52
4.13 The $\pi^0\pi^0$ invariant mass before the 6C kinematic fit 55
4.14 The $\pi^0\pi^0$ invariant mass after the 6C kinematic fit 56

4.15 A comparison of reconstructed and generated photons 57

5.1 The $\pi^0\pi^0$ mass resolution 74
5.2 The $\pi^0\pi^0$ mass resolution as a function of the radiative photon energy 75

6.1 The angular distributions with actual detector acceptance for the two ambiguous solutions in the $\pi^0\pi^0$ mass bin around 2.0 GeV 84
6.2 The angular distributions with perfect detector acceptance for the two ambiguous solutions in the $\pi^0\pi^0$ mass bin around 2.0 GeV 85
6.3 The nominal results: the intensity for each amplitude as a function of $\pi^0\pi^0$ invariant mass 86
6.4 The nominal results: the phase differences as a function of $\pi^0\pi^0$ invariant mass 87
6.5 The nominal intensity for each amplitude as a function of $\pi^0\pi^0$ invariant mass shown with the mathematically predicted ambiguities 88
6.6 The nominal phase differences as a function of $\pi^0\pi^0$ invariant mass shown with the mathematically predicted ambiguities 89
6.7 The nominal results, permutation 1 91
6.8 The nominal results, permutation 2 92
6.9 The nominal results, permutation 3 93
6.10 The nominal results, permutation 4 94
6.11 Alternate results 1: the intensity for each amplitude as a function of $\pi^0\pi^0$ invariant mass 95
6.12 Alternate results 1: comparison with the nominal results 96
6.13 Alternate results 1: pull distribution relative to the nominal results . 97
6.14 Alternate results 2: the intensity for each amplitude as a function of $\pi^0\pi^0$ invariant mass 99
6.15 Alternate results 2: comparison with the nominal results 100
6.16 Alternate results 2: pull distribution relative to the nominal results . 101
6.17 The likelihood contour of the 0^{++} amplitude parameters in a bin with small errors 103
6.18 The likelihood contour of the 0^{++} amplitude parameters in a bin with large errors 104
6.19 The results of the mass dependent fit 106
6.20 The nominal results overlaid with the mass dependent fit 108
6.21 The nominal results overlaid with the mass dependent fit for the 0^{++} amplitude and phase difference 109
6.22 The χ^2 per bin for the comparison between the nominal results and the mass dependent fit 110
6.23 The results of the mass dependent fit 112
6.24 The nominal results overlaid with the mass dependent fit with the $f_0(980)$ 113
6.25 The 0^{++} amplitude and phase difference for the nominal results overlaid with the mass dependent fit with the $f_0(980)$ 114
6.26 The χ^2 per bin for the comparison between the nominal results and the mass dependent fit with an $f_0(980)$ 115

7.1 The difference between the angular distributions of the photon detection efficiency between the inclusive MC and data samples 118
7.2 The differences between the nominal results and those with reweighting due to differences in the angular distributions 120
7.3 The difference in the photon detection efficiency between the inclusive MC and data samples as a function of photon energy 121
7.4 The differences between the nominal results and those with reweighting due to differences in the energy distributions 122
7.5 The intensity for each amplitude in the analysis with a loosened χ^2_{6C} restriction in comparison with the nominal results 123
7.6 The pull distribution for the analysis with a loosened χ^2_{6C} restriction in comparison with the nominal results 124
7.7 A test of the effect of the misreconstructed background on the mass independent results 125
7.8 A test of the effect of the misreconstructed background on the analysis on the MC sample 126
7.9 The intensity for each amplitude for the simulated results 126
7.10 The intensity for each amplitude for the simulated results with the misreconstructed background removed 127
7.11 The pull distribution for the simulated results with the misreconstructed background removed 128
7.12 The intensity for each amplitude in the nominal results is plotted here as a function of $\pi^0\pi^0$ invariant mass for data that include the $\omega\pi^0$ backgrounds 130
7.13 The pull distribution for the nominal results as a function of $\pi^0\pi^0$ invariant mass for data that include the $\omega\pi^0$ backgrounds 131
7.14 A comparison of likelihoods with and without the 4^{++} E3 amplitude . 134
7.15 A comparison of likelihoods with and without the 4^{++} M4 amplitude 135
7.16 A comparison of likelihoods with and without the 4^{++} E5 amplitude . 136
7.17 A comparison of likelihoods with and without the 4^{++} E3 and M4 amplitudes 137
7.18 A comparison of likelihoods with and without the 4^{++} E3 and E5 amplitudes 138
7.19 A comparison of likelihoods with and without the 4^{++} M4 and E5 amplitudes 139
7.20 A comparison of likelihoods with and without all three 4^{++} amplitudes 140
7.21 A comparison of likelihoods with and without the 2^{++} E3 amplitude . 141

A.1 The intensities for each amplitude as well as the phase differences between selected amplitudes are plotted here as a function of $\pi^0\pi^0$ invariant mass. The solid black markers give the results for one set of solutions while the empty red circles show the results for the ambiguous partner. The blue triangles show the predicted ambiguous partner to the solutions represented by the black markers. Similarly, the green squares predict the partners of the open red circle solutions. The fit results are consistent with the prediction. 158

B.1 The pull distributions for a set of exclusive MC samples with a single resonance in the 2^{++} wave, but fit with both the 0^{++} and 2^{++} waves . 161
B.2 The pull distributions for a set of exclusive MC samples with a single resonance in the 0^{++} wave, but fit with both the 0^{++} and 2^{++} waves . 162
B.3 The pull distributions for a set of exclusive MC samples with a resonance in each wave 163
B.4 The results of a fit to an exclusive MC sample that closely resembles the data with perfect detector acceptance and resolution 165
B.5 The results of a fit to an exclusive MC sample that closely resembles the data with actual detector acceptance and resolution 166

C.1 The two photon invariant mass distribution used for the photon detection efficiency study before additional selection criteria 169
C.2 The two photon invariant mass distribution used for the photon detection efficiency study after all selection criteria have been applied . . . 170
C.3 The kinematic window used for the photon detection efficiency study 172
C.4 A comparison of the two photon invariant mass distribution for the inclusive MC and data samples 177
C.5 The two photon invariant mass distribution fits for the inclusive MC used for the photon detection efficiency study 178
C.6 The results of photon detection efficiency study in bins of photon energy 179
C.7 A comparison of the photon detection efficiency of the inclusive MC and data samples as a function of photon energy 180
C.8 The results of photon detection efficiency study in bins of photon angle 181
C.9 A comparison of the photon detection efficiency of the inclusive MC and data samples as a function of photon angle 182
C.10 The results of MC consistency checks of the photon detection efficiency as a function of photon energy 184
C.11 The results of MC consistency checks of the photon detection efficiency as a function of photon angle 185
C.12 A comparison of the photon energy distributions for the inclusive MC and data samples 186

Chapter 1

Motivation

While the Standard Model of physics has yielded remarkable successes, a complete understanding of the fundamental interactions of particles remains elusive. The light scalar meson spectrum, for example, remains relatively poorly understood despite many years of scientific investigation. This lack of understanding is due in part to the nature of the structures in this region. States that are narrow and well separated in an invariant mass spectrum can be described quite well by a particular function, for example a Gaussian or Breit-Wigner function. In contrast, the broad, overlapping states that are present in the light scalar spectrum are poorly described by the most accessible analytical methods [1]. A rigorous study of the particle interactions in this region can yield useful information on the fundamental interactions of particles.

While significant progress has been made recently, the nature of the scalar states remains uncertain. This may be due in part to the use of simple parameterizations of resonances, such as the Breit-Wigner parametrization, which only provide good approximations for narrow, well separated states. The application of such a parameterization to data with broad, overlapping states has several drawbacks. For example, overlaps of resonances may result in an apparent shift in the Breit-Wigner parameters of a given resonance [1]. All of this makes identification and interpretation of such states quite challenging.

The scalar meson spectrum has been studied in many ways, including πN scattering [2], $p\bar{p}$ annihilation [3], central hadronic production [4], ψ' [5], J/ψ [6, 7, 8], B [9], D [10], and K [11] meson decays, $\gamma\gamma$ formation [12] and ϕ radiative decays [13]. The PDG lists nine f_0 states. These include the $f_0(500)$ (or σ), the $f_0(980)$, the $f_0(1370)$, the $f_0(1500)$, the $f_0(1710)$, the $f_0(2220)$, and the $f_0(2330)$ [1]. Two additional states, the $f_0(2020)$ and the $f_0(2100)$, are listed with the caveat "needs confirmation".

Knowledge of the low mass scalar meson spectrum is important for several reasons. If one is interested in probing the most fundamental of interactions, $\pi\pi$ scattering is an attractive medium as it allows for testing of chiral perturbation theory to one loop [14]. Additionally, the lightest glueball states are expected to be scalars [15, 16, 17]. The observation of such states would be an excellent test of QCD. Unfortunately, glueballs may mix with bound states of quarks, making identification of glueballs experimentally challenging. A practical method for observing glueballs is to look for overfilled nonets, wherein all isoscalar quark bound states have been associated with observed mesons and an additional meson is also observed. Such an analysis requires a thorough understanding of the properties of each state.

The glue-rich environment created by the annihilation of the charm and anti-charm quarks within the J/ψ is an excellent laboratory in which to search for glueballs. Radiative decays of the J/ψ, in particular, are expected to produce a clean spectrum for such a search. The conservation of parity in strong and electromagnetic interactions, along with the conservation of angular momentum, restricts the quantum numbers of a $\pi\pi$ resonance produced in this channel to $J^{PC} = 0^{++}, 2^{++}, 4^{++}$, etc. This restriction simplifies an amplitude analysis since fewer amplitudes are accessible. An added benefit of an analysis of this channel is the range of the mass spectrum accessible by radiative J/ψ decays. Thus an amplitude analysis of radiative J/ψ decays provides an excellent laboratory in which to study the scalar meson spectrum. The neutral channel is of particular interest due to the lack of large backgrounds like $\rho\pi$, which provides a challenge for an analysis of the charged channel [18].

In addition to these considerations, radiative decays of the J/ψ to $\pi^0\pi^0$ are simplified relative to other three body decays, because the radiative photon does not interact with the $\pi^0\pi^0$ pair. This means that the final state interaction is entirely contained in the piece of the amplitude that describes the $\pi^0\pi^0$ interaction. Of course, rescattering effects in the final state, for example KK to $\pi^0\pi^0$, may still exist. Unfortunately, it is not possible to separate the part of the amplitude for this decay associated with the production process from that of the final state interactions. Finally, an analysis of radiative J/ψ decays has the added benefit of a high statistics data sample, $(1.3106 \pm 0.0072) \times 10^9$ events, from the BESIII experiment.

The possible $\pi^0\pi^0$ intermediate states of J/ψ radiative decays include several glueball candidates such as the $f_0(1500)$ and the $f_0(1710)$, though the existence of $f_0(1500)$ in this decay is uncertain due to low statistics [18]. Radiative J/ψ decays may be used to test interpretations of states such as the $f_0(1370)$ and $f_0(1710)$, which may be interpreted as a bound system of vector mesons [19, 20]. The existing branching fractions for the $f_0(1710)$ to $\pi\pi$ and KK in radiative J/ψ decays to $\pi\pi$ [18] and KK [21] appear inconsistent with those from J/ψ decays to $\omega\pi\pi$ [7] and ωKK [8]. Additionally, in some molecular and quark models, the suppression of the $f_0(1370)$ relative to the $f_0(1710)$ in radiative J/ψ decays is contrary to expectations [20]. The authors of Ref. [20] claim that a possible explanation for this is that the structure near 1.765 GeV/c^2 should not be attributed to the $f_0(1710)$. A high statistics study of the scalar spectrum in radiative J/ψ decays would be useful to clarify this picture.

Model predictions on the nature and mixing of scalar $q\bar{q}$ and glueball states vary. One prediction [22] suggests that the $f_0(1710)$ is mostly $s\bar{s}$, while the $f_0(1370)$ and $f_0(1500)$ share roughly equal amounts of glue, though mixing is not necessarily required [23]. Another suggests that the $f_0(1500)$ is dominantly $s\bar{s}$, while the $f_0(1710)$

carries the largest glueball component. Stronger evidence of the existence and relative size of scalar states in radiative J/ψ decays may be of use in better constraining these interpretations. For example, if the $f_0(1500)$ and/or $f_0(1710)$ consist primarily of glue, they should be copiously produced in the glue-rich J/ψ decay. A pure glueball state is expected to decay into $\pi\pi$, $\eta\eta$, $\eta\eta'$ and KK with relative ratios 3:1:0:4 [23].

The strongest evidence for glueballs require the knowledge of the production of candidate states in various environments. For example, glueball states should be favored over $q\bar{q}$ states in radiative J/ψ decays, but the opposite should be true in $\gamma\gamma$ fusion [24]. Neither the $f_0(1500)$ nor the $f_0(1710)$ have significant signals in this channel [25]. Studies of these final states in radiative J/ψ decays are therefore useful. Other expectations for glueball states include their being favored over $q\bar{q}$ states in central scattering processes like pp as well as their production in $p\bar{p}$ annihilation [26]. A thorough study of the scalar states in each of these processes is therefore necessary to determine their nature.

J/ψ radiative decays to $\pi^+\pi^-$ have been analyzed previously by the MarkIII [27], DM2 [28], and BES I [29] experiments. Decays to $\pi^0\pi^0$ were also studied at Crystal Ball [30] and BES I [31], but these analyses were severly statistics limited, particularly for the higher mass states. Each of these analyses claimed evidence for the $f_2(1270)$ and some possible additional states near 1.710 GeV/c^2 and 2.050 GeV/c^2. More recently, the BES II experiment studied these channels and implemented a partial wave analysis [18], but this analysis, like its predecessors, was limited by complications from large backgrounds as well as low statistics. Prominent features in this analysis include the $f_2(1270)$, the $f_0(1500)$, and the $f_0(1710)$. The BW mass and width of each of these structures is measured. Due to statistical limitations, the $\pi^0\pi^0$ channel was studied only as a cross check on the analysis of the charged channel.

The amplitude analysis presented here on the $\pi^0\pi^0$ spectrum in radiative J/ψ decays is performed using a mass independent method, which attempts to introduce as few model dependencies as possible. In particular, the final state interactions are not parametrized according to a model, but are absorbed into the complex fit parameters in a maximum likelihood fit. By binning the data set in terms of $\pi^0\pi^0$ invariant mass and performing a fit in each bin, it is possible to extract the function that describes the final state interactions as a function of invariant mass. These results may be useful for more complete analyses of the scalar spectrum. The data set consists of the approximately $(1.3106 \pm 0.0072) \times 10^9$ J/ψ decays collected by the BESIII collaboration in 2009 and 2012.

In addition to the mass independent analysis, a mass dependent approach is implemented. This allows for a comparison with previous studies of this reaction and shows that the mass independent method gives results that are consistent with a mass dependent parameterization. In the mass dependent analysis, the part of the amplitude that describes the final state interactions is parameterized with a set of interfering Breit-Wigner line shapes. The information on the scalar and tensor spectra from the mass independent results provide a useful handle for the number and type of resonances to be included in the mass dependent fits.

Chapter 2

Theoretical Background

Nearly all of the experimental data that has been gathered concerning the properties and interactions of subatomic particles can be explained in the framework of the Standard Model of Particle Physics [1]. Despite some shortcomings, such as the fact that it can only describe three of the four fundamental forces of nature, for the past century new experimental data has conformed closely to this framework. One notable example is the recent discovery of a Higgs-like particle at the Large Hadron Collider, perhaps the world's best know particle accelerator [34, 35].

According to the Standard Model, all of the conventional matter in the universe consists of different combinations of fundamental particles called fermions, along with several force mediating bosons. The word fundamental in this context means that we believe these particles are indivisible (unlike the atom, whose name actually means indivisible). These fermions can be further divided into quarks and leptons, which interact via four fundamental forces; gravity, electromagnetism, and the strong and weak nuclear forces. These forces are mediated by particles called gauge bosons. That is, the interaction is accomplished with the exchange of these mediating particles.

The Standard Model provides a theoretical framework that describes how particles interact under the electromagnetic, strong and weak forces. The duty of the experi-

[1]For a general review of this topic, see for example Ref. [32] or Ref. [33]

mental particle physicist, then, is to test the theoretical predictions that emerge from the Standard Model and other theories and to rigorously investigate any unexpected discoveries. Experimental evidence can provide validation or refutation for a theory or perhaps support a modification of the original theory to encompass the observed behavior. The interplay between theory and experiment is what ultimately leads to the best understanding of nature.

2.1 Standard model hadrons

Both quarks and leptons may be organized into generations of matter, with higher generation particles being unstable and eventually decaying into their first generation counterparts. For this reason, most of what we imagine as ordinary matter consists of the lowest generation of quarks (less than whimsically named up and down) and leptons (the electron and electron neutrino). The higher generations of these particles exist only in high energy environments such as stars or particle accelerators. For each particle there also exists an antimatter partner, which are generally labeled with a bar for quarks ($\bar{u}$) and with the appropriate sign for charged leptons. When a matter particle meets its antimatter partner, for example an electron (e^-) and a positron (e^+), the two annihilate into energy. This is a useful mechanism for creating high energy environments, which have the potential to produce new, interesting particles that may consist of higher generation quarks or leptons.

2.1.1 Classification

The six flavors of quarks may be divided into two categories; light quarks (up, down, and strange) and heavy quarks (charm, bottom, and top). Each quark flavor other than u and d is ascribed a property which is conserved in all interactions other than weak interactions. For example, the charm quark (c) carries charm. This means that subatomic particles that contain these types of quarks prefer to decay in specific ways. For example, charmonium states like the $\psi(3770)$ prefer to decay through a $D\bar{D}$ pair. Since the $\psi(3770)$ does not carry charm, the charmed D mesons must carry opposite charm quantum numbers. This is a useful characteristic for studies of charmed mesons.

Interestingly, quarks never appear by themselves. Rather, they are the constituents of a group of subatomic particles called hadrons. Baryons, like the proton or neutron, are comprised of three quarks. Mesons, like the pion, instead contain one quark and one anti-quark. While the theory of quarks and gluons (discussed below) does not proscribe hadrons with greater numbers of quarks, most experimental evidence is consistent with meson states consisting only of quark anti-quark pairs. Recent studies that contradict this notion have generated a great deal of interest in the field of meson spectroscopy.

Subatomic particles like hadrons can be classified in other ways. The basic idea is to group particles according to their characteristics. For example, particles have an intrinsic quality called spin. Those with half integral spin are called fermions and those with integral spin are called bosons. This classification is useful because fermions and bosons behave differently. Fermions obey the Pauli exclusion principle, which states that identical fermions cannot occupy the same quantum state, while bosons are exempted for this restriction. The quantum state of a particle is given by a descriptive set of parameters called quantum numbers, which also provide a useful means of classification.

In high energy physics, the most useful identifying characteristics of mesons are the quantum numbers J^{PC}. The total angular momentum of the meson, J, is a combination of its spin S and orbital angular momentum L. The other two quantum numbers relate to the effect of some basic symmetry operations. Parity, P, relates to the properties of the meson under the reversal of each spatial component. The parity of a meson is given by the product of -1^L and the intrinsic parities of the constituent quarks (by convention fermions are given $P = +1$). The third quantum number of interest is C, which describes the effect of charge conjugation. This is essentially the reversal of the charge and magnetic moment of a particle. Not all meson have a charge conjugation quantum number, because the symmetry operation may change its species. For example, applying charge conjugation to the π^- will turn it into a π^+.

Another useful property of hadrons is called isospin. Isospin is an approximate symmetry that is conserved in strong interactions due to the fact that the two lightest quarks (up and down) are approximately degenerate in mass. The symmetry is broken due to the small difference in mass of the up and down quarks. It is isospin symmetry that explains why the proton and neutron have such similar masses (the difference is on the order of 0.14% of the neutron mass). A proton consists of two up quarks and one down quark, while the neutron contains only one up quark and two down quarks. Isospin symmetry implies that the proton and neutron can be viewed as different states of the same particle. In mathematical terms, they are said to be part of the doublet, the fundamental representation, of an SU(2) Lie group. In this sense, the proton and neutron both have isospin 1/2. The projection, I_z, of the isospin for the proton is 1/2, while that for the neutron is $-1/2$. Table 2.1 gives the isospin and other identifying features of the quarks.

	u	d	c	s	t	b
Electric charge (Q)	$\frac{2}{3}$	$-\frac{1}{3}$	$\frac{2}{3}$	$-\frac{1}{3}$	$\frac{2}{3}$	$-\frac{1}{3}$
Isospin (I)	$\frac{1}{2}$	$\frac{1}{2}$	0	0	0	0
Isospin z-component (I_z)	$\frac{1}{2}$	$-\frac{1}{2}$	0	0	0	0
Strangeness (S)	0	0	-1	0	0	0
Charmness (C)	0	0	0	1	0	0
Bottomness (B)	0	0	0	0	-1	0
Topness (T)	0	0	0	0	0	1

Table 2.1: The quantum numbers of quarks.

By applying these mathematical tools to the light quarks, one can envision mesons as elements of an SU(3) symmetry group [1]. This set is commonly labeled $SU(3)_f$ to emphasize that is applied to the approximate symmetry under the interchange of the light quark types, called flavors. In this sense, two combinations of a quark and antiquark (3 x 3) are possible; the singlet and the octet (1 + 8). Together these are called a nonet (Fig. 2.1). In reality, this symmetry is badly broken because the strange quark is significantly more massive than the up and down quarks. Nevertheless, the organization this brings to the "particle zoo" is very helpful.

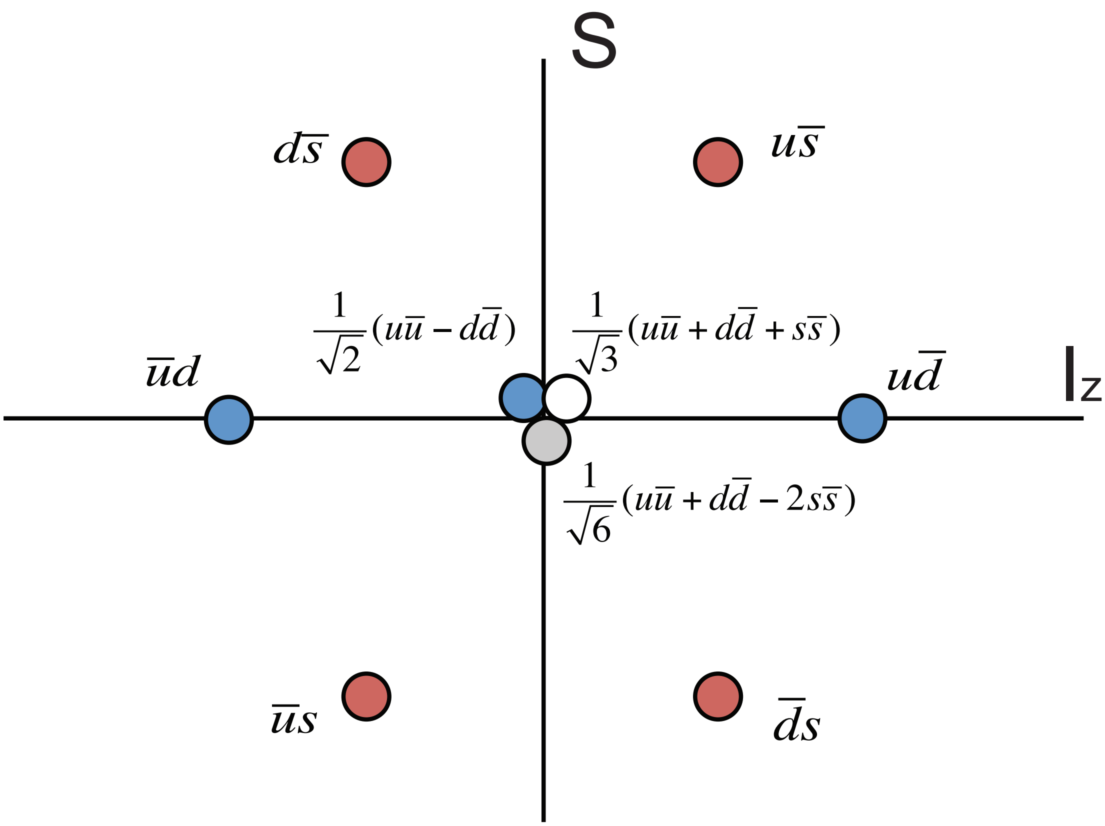

Figure 2.1: A graphical representation of the light quark nonet with states labeled by their quark content.

Given the basic structure of a meson and the restrictions of the Pauli exclusion principle, the possible states for a meson containing u and d quarks include

$$
\begin{aligned}
&|I=1, I_z=1>=|u\bar{d}> \\
&|I=1, I_z=0>=\frac{1}{\sqrt{2}}|u\bar{u}-d\bar{d}> \\
&|I=1, I_z=-1>=-|\bar{u}d>\ .
\end{aligned}
\tag{2.1}
$$

For the simplest case of mesons with total angular momentum 0 and odd parity (-), these states relate to the π^+, π^0, and π^- mesons respectively. In a similar way, it is possible to describe an isospin zero partner of the pions, which is called the eta_8 ($\frac{1}{\sqrt{6}}(u\bar{u}+d\bar{d}-2s\bar{s})$), as well as the isospin zero singlet state, the η_0 ($\frac{1}{\sqrt{3}}(u\bar{u}+d\bar{d}+s\bar{s})$). These together with these and the isospin 1/2 Kaons, the pions are part of the pseudoscalar nonet. The name pseudoscalar references the fact that, while these states are scalars ($J=0$), parity operations on these states are similar to those of a vector (the wavefunctions change sign under spatial inversion).

While certain particles like the ω and ϕ retain their historical names, neutral flavor mesons, with strangeness and heavy quark flavor equal to zero, are named according to a particular scheme (Tab 2.2). For example, isovector (I=1) scalar (J^{PC}=0^{++}) particles are labeled with an a and given a subscript which designates the total angular momentum of the state. Isoscalar (I=0) scalar states are instead labeled as f (or f') states. The analysis presented here focuses on a study of the isoscalar scalar spectrum (I^GJ^{PC}=0^+0^{++}), and so is primarily concerned with the f states.

$^{2S+1}L_J =$	$1(L \text{ even})_J$	$1(L \text{ odd})_J$	$3(L \text{ even})_J$	$3(L \text{ odd})_J$
$u\bar{d}$, $u\bar{u}-d\bar{d}$, $\bar{u}d$	π	b	ρ	a
$u\bar{u}+d\bar{d}$ and/or $s\bar{s}$	η,η'	h,h'	ω,ϕ	f,f'
$c\bar{c}$	η_c	h_c	ψ	χ_c
$b\bar{b}$	η_b	h_b	Υ	χ_b

Table 2.2: The naming scheme for neutral flavor mesons [1].

2.1.2 Quantum Chromodynamics

The interactions of hadrons are described by a non-abelian field theory called Quantum Chromodynamics (QCD). In a similar way that Quantum Electrodynamics (QED) ascribes to electrons an electric charge, which is mediated via the exchange of photons, QCD ascribes to the quarks an additional property called color charge, which is mediated via gluons. The reason quarks must carry color charge is because of symmetry considerations for quarks within hadrons (recall quarks are fermions). The contrast between QED and QCD is that, while photons are not electrically charged, gluons carry color charge and therefore may interact with other gluons. This greatly complicates the theory because higher order interactions, consisting of gluon loops, make significant contributions to each process. In fact, a simple prediction using the sum of the masses of constituent quarks would give masses of particles like the proton that are wildly inconsistent with experimental data.

One of the important characteristics of QCD is the notion of quark confinement. The strength of the force between quarks is great at relatively large quark separation (or low energies), confining the quarks to hadrons. It is only in the short distance (high energy) limit that the binding is weakened, a concept called asymptotic freedom. This variability in the coupling of quarks within hadrons presents a challenge to theoretical treatments of QCD. Perturbative analyses, in which a prediction is calculated by adding successively more complex interactions, fare poorly at all but the highest energies. One method to overcome this difficultly is to perform the calculations in a finite area under specific conditions, a process called Lattice QCD (LQCD) [36]. Unfortunately, theoretical and technological barriers necessitate that lattice calculations use quark masses that are often greater than those found in nature.

The self-interacting nature of gluons also suggests that hadrons may exist in which the gluonic field within a hadron carries some angular momentum (a hybrid) or even in which no quarks are present and the hadron is composed entirely of gluons (a glueball). Mesons of this type may have quantum numbers that are inaccessible to their conventional counterparts. Observation of a meson with exotic quantum numbers is conclusive evidence for mesons that cannot consist of a simple quark-antiquark pair.

Not all mesons containing gluonic excitations are readily apparent as non-conventional states. The lowest lying glueball state is expected to have scalar quantum numbers (0^{++}). An observation of a state matching this prediction is experimentally challenging, because the glueball may mix with the conventional states. That is, each state within the spectrum may have some fractional composition of a glueball state and some from conventional quark states. In fact, the challenges to hadron spectroscopy in this region also extend to LQCD calculations. The existence of broad and low mass resonances (like the σ) make calculations in this region very complicated. No LQCD calculations in the low mass scalar spectrum have been published to date [36]. This makes experimental data vital for a good understanding of states in this spectrum.

2.2 The $\pi^0\pi^0$ System

The nature of meson states with scalar quantum numbers has been a topic of great interest for several decades. Despite the availability of a large amount of data on $\pi\pi$ and KK scattering in this region, the existence and characteristics of these states remain controversial. Nonetheless, coupled channel studies using the K-matrix formalism have recently produced some excellent measurements [37]. Additionally, dispersive analyses have been directed toward understanding the scalar meson spectrum in the lowest mass region [38]. With the inclusion of data from radiative decays, an interpretation of the scalar meson states may become more clear.

The Particle Data Group (PDG), provides a compilation of experimental results. In the 2013 edition of the PDG [1], seven f_0 states are listed. These include the broad

$f_0(500)$ or σ (which was previously listed as the $f_0(600)$), a very narrow $f_0(980)$, an $f_0(1370)$, an $f_0(1500)$, and $f_0(1710)$, an $f_0(2200)$, and an $f_0(2330)$. Also listed are two additional states, the $f_0(2020)$ and $f_0(2100)$, which are given the caveat "needs confirmation." Other states in this region may include the $f_0(1790)$, which is observed in J/ψ decays to $\phi\pi^+\pi^-$, distinct from the $f_0(1710)$ [6]. Some studies also introduce other states in an attempt to better interpret the experimental and theoretical results. A brief description of some of these states follows. For a more detailed description of the current theoretical and experimental standings of scalar meson states, see for example Ref. [23] or Ref. [39].

2.2.1 The $f_0(500)$ (σ)

The σ has been studied in $\pi\pi$ S-wave phase shift data from πN scattering [40, 41], near threshold K_{e4} [11, 42], $\pi\pi$ to $K\bar{K}$ rescattering [43, 44], $p\bar{p}$ annihilation at rest [45, 3] and in central collision [46], D^+ decays to $\pi^+\pi^-\pi^+$ [10], J/ψ decays to $\omega\pi^+\pi^-$ [7], and $\psi(2S)$ decays to J/$\psi\pi^+\pi^-$ [47, 5]. Despite this plethora of experimental study, the history of the $f_0(500)$ or σ meson is rife with controversy. This may be due in part to its complicated structure, particularly its phase motion, which is unlike a traditional resonance [23].

The PDG listed the σ as "not well understood" until 1974. It was subsequently removed in 1976 and then reappeared in 1996 as the $f_0(600)$. Studies in heavy meson decays led to listing the $f_0(600)$ as "well established" in 2002 even though the mass range extended from 400 to 1200 MeV and the width from 500 to 1000 MeV[48]. More recently, the consistency of dispersive results has led to a much narrower estimate of the mass to be between 400 and 550 MeV and the width between 400 and 700 MeV [38]. The name was also changed to the $f_0(500)$ in the more recent versions of the PDG [1].

2.2.2 The $f_0(980)$

In contrast to the σ meson, the existence of the $f_0(980)$ is not controversial. Nevertheless, its measurement and interpretation provide significant challenges. This is due in part to its proximity to the threshold for $K\bar{K}$ production, to which it strongly couples. This produces a cusp-like effect of the $f_0(980)$ lineshape. Study of the $f_0(980)$ is further complicated by its interference with nearby broad states like the σ.

The $f_0(980)$ has been studied in $\pi^- p$ decays to $\pi^0\pi^0 n$ [49], ϕ decays to $f_0\gamma$ [50, 51], and $\gamma\gamma$ to $\pi\pi$ [12]. It is often described as being a $K\bar{K}$ molecule [52], but may have a much more complicated structure [53]. The PDG quotes a mass of 980 $\pm$ 20 MeV and a width range between 50 and 100 MeV [1].

2.2.3 The $f_0(1370)$

The $f_0(1370)$ meson is a very broad state whose existence has been somewhat controversial. It was called the $\epsilon(1300)$ upon its discovery in experiments on $\pi\pi$ to KK scattering [54, 44] and decays dominantly to four pions [114]. Some interpret the lack of convincing phase motion around 1370 MeV/c^2 as evidence that the $f_0(1370)$ is not a resonant state. Analyses on CERN-Munich data have found no evidence for the $f_0(1370)$, instead describing the low mass spectrum with only the $f_0(980)$, $f_0(1500)$, and an $f_0(1670)$ scalar glueball state [55, 56]. Other studies have shown that the existing data, including $p\bar{p}$ annihilation and J/ψ decays, are consistent with an $f_0(1370)$ [57].

The PDG does not quote a mass for the $f_0(1370)$, rather listing a range for the pole position of (12001500)i(150250) MeV [1]. A Breit-Wigner fit in J/ψ decays to $\phi\pi^+\pi^-$ gives a mass of 1350 $\pm$ 50 MeV and a width of 265 $\pm$ 40 MeV [6]. In comparison, studies in $p\bar{p}$ annihilation give masses between 1330 and 1360 MeV with widths between 200 and 450 MeV [39].

2.2.4 The $f_0(1500)$

With a mass and width of 1505 ± 6 MeV and 109 ± 7 MeV respectively, the $f_0(1500)$ branching ratio to $\pi\pi$ is about 35%, while its decay through 4π makes up about half of the total decay [1]. In radiative decays to $\pi^+\pi^-$, a previous Breit-Wigner fit yielded a mass of $1466 \pm 6 \pm 20$ MeV [18], significantly lower than the PDG mass. In contrast, studies in central pp production yield masses closer to 1510 MeV [25].

The $f_0(1500)$ state is one of the prime candidates for a scalar glueball. The branching ratio of the $f_0(1500)$ to $K\bar{K}$ is small [58], but the upper limit from $\pi^+\pi^-$ suggests a mainly $s\bar{s}$ state [25]. These contradictory results suggest that the $f_0(1500)$ may possess a high concentration of glue [1]. This interpretation is supported by the non-observation of the $f_0(1500)$ in $\gamma\gamma$ collisions, since glueball states do not couple directly to photons and therefore their production should be suppressed in this channel [59, 25]. The presence of the $f_0(1500)$ in radiative J/ψ decays is debatable [18] due to limited statistics.

2.2.5 The $f_0(1710)$

First discovered as an $\eta\eta$ resonance in radiative J/ψ decays [60], the angular momentum of the $f_0(1710)$ was controversial. An analysis with data from WA102 in central collisions finally set the quantum numbers to be 0^{++} [58]. The lack of a signal for the $f_0(1710)$ in analyses of $p\bar{p}$ annihilation data suggest that it is primarily an $s\bar{s}$ state [61]. This is due to the fact that the OZI rule forbids $p\bar{p}$ annihilation production of states made purely of $s\bar{s}$, even though scalar mesons are strongly produced by this mechanism [23]. The data from ALEPH are consistent with this interpretation since the $f_0(1710)$ is not observed in $\gamma\gamma$ collisions to $\pi^+\pi^-$, but may be observed in $K_s^0K_s^0$ [59, 25]. This is also in accord with recent results from the Belle Collaboration on $\gamma\gamma$ collisions to $K_s^0K_s^0$ [62].

Studies of the $f_0(1710)$ have yielded masses from $1710 \pm 12 \pm 11$ MeV in centrally produced pp production [4], which is very close to the PDG value of 1720 $\pm$ 6 MeV [1], to as much as 1765 $\pm$ 4 $\pm$ 13 in radiative J/ψ decays [18]. Indeed, there is some suggestion that the state produced in this latter mechanism should be attributed to a different scalar state [20].

2.2.6 Higher mass scalar states

Several scalar states have been observed above 2 GeV/c^2. These include the $f_0(2100)$, which was observed in J/ψ decays [63] as well as $p\bar{p}$ annihilation [64]. The latter study also saw evidence of an $f_0(2200)$ and an $f_0(2330)$, which are also listed in the PDG [1]. Also listed are two additional states including the $f_0(2020)$, which has been seen in central pp interactions [4], and and $f_0(2100)$.

2.2.7 Tensor states

The description of spin 2 states in the low mass region is much less complicated than the scalar spectrum. The $f_2(1270)$ is the dominant feature in the $\pi\pi$ system [18] while the $f_2'(1525)$ decays primarily to $K\bar{K}$ [65]. The general interpretation of this system is a nearly ideally mixed system in which the $f_2(1270)$ is primarily $u\bar{u}$ and $d\bar{d}$ and the $f_2'(1525)$ is primarily $s\bar{s}$. These two states are joined by a relatively large number of less well established states. For a review of the tensor meson spectrum, see for example Ref. [66].

2.2.8 Spin 4 states

Two spin 4 states are listed in the PDG [1]. These states exist above 2 GeV/c^2 and include the relatively wide $f_4(2050)$ [67, 68] and the $f_4(2300)$ [69].

2.3 Production Mechanism

As discussed above, various production mechanisms have been utilized for meson spectroscopy in the low mass scalar region. One of the most promising is that used in this analysis, radiative decays of the J/ψ meson. The J/ψ is a charmonium meson, which consists of a charm anti-charm quark pair, but exists below the open charm threshold. That is, the energy of the J/ψ is not great enough to allow it to decay into charmed mesons. Charmed mesons contain a charm quark and a light quark and are the favored channel for charmonium decays when kinematically accessible. This means that decays in which the quarks annihilate into gluons now dominate. These decays are otherwise suppressed (called OZI suppression). This "glue-rich" environment provides an excellent laboratory in which to search for glueballs.

Recall that mesons carry no color (they are color singlet states). This means that the annihilation process in J/ψ decays must proceed through at least two gluons. Since the J/ψ is a spin triplet state, C-parity restrictions require an odd number of gluons, so the favored decay is mediated by three gluons. Radiative J/ψ decays on the other hand, proceed through two gluons. The extra factor of the fine structure constant results in a suppression of the radiative decay relative to that of the three gluon decay. This suppression factor, though, is only about a factor of ten, which leaves the rate of radiative J/ψ decays at about 8% of all J/ψ decays. For a more thorough review of J/ψ decays, see for example Ref. [30].

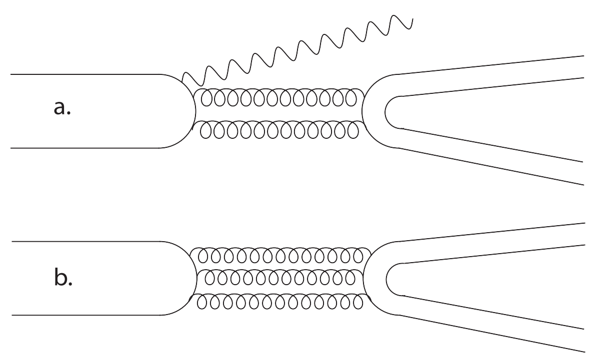

Figure 2.2: A graphical representation of the (a) radiative decay and the (b) three gluon decays of the J/ψ meson.

Chapter 3

Experimental Apparatus

Amidst the aftermath of the violent collision between high energy particles lie clues to the nature of fundamental forces. Some of the most interesting and illuminating information may only be accessed from particle interactions at very high energies. These energies are attainable only in collisions such as those which occurred immediately following the big bang. Physicists are able to recreate these high energy collisions in the laboratory of particle accelerators. The result is the creation of unstable particles that will decay almost instantly into lower energy particles. These may then decay again, according to a particular decay channel. Surrounding the point at which the collisions occur are particle detectors that are designed to collect information on the final state particles from a decay. From this information, it becomes possible to determine the properties of the original, or parent, particle.

Recording all of the information that is released in the collision and subsequent annihilation of high energy particles requires sensitive and finely tuned equipment. A great deal of time and effort is required in the construction and maintenance of each component of a particle detector that in the heart of a particle accelerator. Once a set of data is collected, analysis of the information requires sophisticated computational tools and techniques. Through the collaboration of detector hardware and software, and often the creativity of the researcher, it is possible to reconstruct and interpret the details of the collision and the underlying physics of the particle interactions.

3.1 The BEPCII Accelerator

The Beijing Electron Positron Collider II (BEPCII) is a major upgrade of the accelerator based at the Institute for High Energy Physics (IHEP) in Beijing, China. The original BEPC accelerator was operated from 1989 to 2004. The upgraded collider was completed in July of 2008 and began running for data collection in March of 2009. With a design luminosity of $1 \times 10^{33}\text{cm}^{-2}\text{s}^{-1}$ at a center of mass energy of 3.78 GeV, BEPCII operates at energies between 2 and 4.6 GeV. This energy range is of interest because it spans a region wherein both short-distance and long-distance effects are relevant.

BEPCII is a double ring e^+e^- collider with a circumference of 237.5 m (Fig. 3.1). A 202 meter long linear accelerator (LINAC) uses a Radio Frequency (RF) system to accelerate electrons and positrons to an energy of approximately 1.89 GeV. The positron beam is a derivative of the electron beam and is created by impinging electrons, which are accelerated to an energy of about 250 MeV, on a tungsten target. The positrons created by this collision are collected using focusing magnetic field. The electron and positron beams are then injected into two storage rings, one for the electron beam and another for the positron beam. In each beam, a superconducting RF cavity is used to change or maintain the beam energy.

The storage rings contain a series of dipole and quadrupole magnets, which are useful for bending and focusing the beams respectively. Sextupole correcting magnets are also used to shape the beam. The electron and positron beams consist of bunches of particles spaced about 8 ns apart and have a relative energy spread of about 0.5 MeV. The beams rotate in opposite directions and are steered to an interaction point

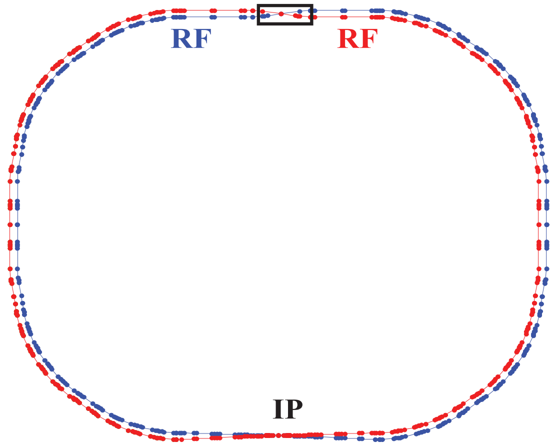

Figure 3.1: A schematic representation of the BEPCII storage ring is shown here. The bending and focusing magnets are depicted by red and blue markers along the beam lines. The beams bypass each other at the northern crossing (top), while at the interaction point (bottom) the beams collide at an angle of about 11 mrad.

(IP) that lies at the center of the BESIII detector. The collision takes place at a horizontal crossing angle of about 11 mrad. This means that any particles created by the interaction of the beam bunches will not be produced exactly at rest, but will have some non-zero momentum. Decay products from the collision move outward through the BESIII detector components.

3.2 Introduction to the BESIII Detector

The Beijing Spectrometer (BESIII) is a general-purpose, hermetic detector located at BEPCII in Beijing, China. BESIII and BEPCII represent major upgrades to the BESII detector and BEPC accelerator. The physics goals of the BESIII experiment cover a broad research program including charmonium physics, D-physics, light hadron spectroscopy and τ physics, as well as searches for physics beyond the standard model. The detector is described in full detail elsewhere [70]. Brief descriptions of the detector components follow.

The BESIII detector consists of five primary components working in conjunction to facilitate the reconstruction of collision events. A schematic of the detector is displayed in Fig. 3.2. Charged particle tracking is performed with a helium-gas based multilayer drift chamber (MDC). The momentum resolution of the MDC is expected to be better than 0.5% at 1 GeV/c^2, while the expected dE/dx resolution is 6%. With a timing resolution of 90 ps (120 ps) in the barrel (endcap), a plastic scintillator Time-Of-Flight (TOF) detector is used to assist in particle identification. The energies of electromagnetic showers are determined using information from the electromagnetic calorimeter (EMC). The EMC consists of 6240 CsI(Tl) crystals arranged in a barrel and two endcap sections. The EMC provides an angular coverage of about 93% of 4π and an energy resolution of 2.5% (5%) at 1.0 GeV. The position resolution of the EMC is 6 mm (9 mm) in the barrel (endcap). Particles that escape these detectors travel through a muon chamber system (MUC), which provides additional information on the identity of particles. The MUC provides 2 cm position resolution for muons and covers 0.89 of 4π. Muons with momenta over 0.5 GeV/c^2 are detected with an efficiency greater than 90%. The efficiency of pions reaching the MUC is about 10% at this energy. Finally, a superconducting solenoid magnet provides a uniform 1 T field within the detector.

3.3 Charged Particle Tracking

Much of the information on final state particles moving through the detector comes from the charged particle tracking systems. By combining the information from each of these detector components, it is possible to calculate the momentum of high energy particles coming from the beam interaction. For particles with momentum within a certain range, it is also possible to use information from these components to determine the identity (mass) of the particles.

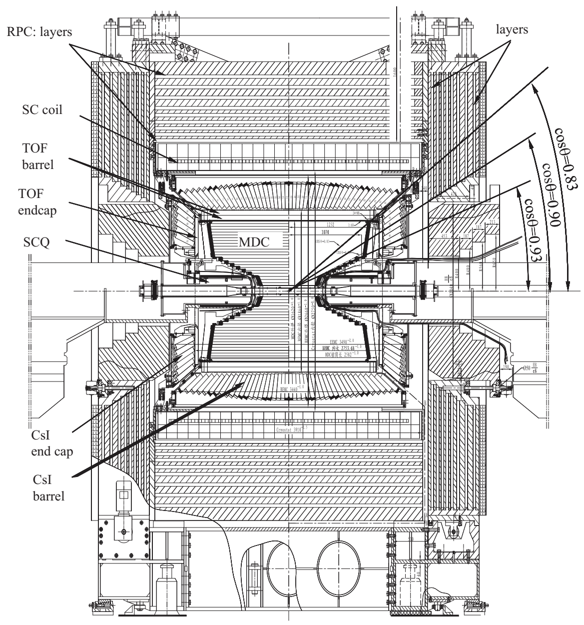

Figure 3.2: A schematic representation of the BESIII detector is shown here. The beam line runs horizontally with the interaction point at the center of the diagram. The detector is cylindrically symmetric about the beam line.

3.3.1 The Solenoid Magnet

The superconducting solenoid magnet, located outside of the EMC, encloses the inner detector components. It is designed to provide a uniform axial magnetic field with a magnitude of 1 T. The solenoid has a mean radius of 1.482 m and a length of 3.52 m. This gives a good idea of the overall size of the BESIII detector. The magnetic field created by the solenoid enables accurate measurements of the momentum of charged particles, which are deflected due to the Lorentz force. Any charged particle moving through the field will follow a helical trajectory, which depends on the sign of the electric charge. This allows reconstruction algorithms to determine the charge of the particle.

3.3.2 The Main Drift Chamber

The bunches of electrons or positrons that make up the beams interact within a beryllium beam pipe at the center of the detector. The MDC immediately surrounds the beam pipe and is responsible for collecting much of the information that is useful for calculating the momenta of charged particles coming from the interaction point. With an inner radius of 59 mm (2 mm from the beam pipe) and an outer radius of 810 mm, the BESIII MDC covers a polar angle of $|\cos(\theta)| \leq 0.83$ for the innermost layers and $|\cos(\theta)| \leq 0.93$ for the outermost layers (Fig. 3.3). The overall design of the MDC is similar in design to the drift chamber used in the CLEO-III detector [71]. Drift chambers of this type depend on the ionization of gas molecules caused by collisions with high energy charged particles. Some fraction of the energy of the particles is lost when it collides with the gas molecules. The electrons created by such collisions drift toward wires that collect information such as the total charge of particles created by the ionization.

The MDC consists of many drift cells, each of which contain a sense wire surrounded by eight field wires. The 110 μm gold plated aluminum field wires are held at ground while the 25 μm gold plated tungsten sense wires are held at positive high voltage. The field accelerates the ionized electrons toward the sense wires, inducing additional ionization by the electrons as they near the wires. The resulting electron avalanche is detected by the sense wires, which are amplified and read out by fast electronics. In total, the MDC contains 28,640 wires.

By measuring the arrival time of the electrons at the sense wire, and with knowledge about the drift velocity of electrons within a certain gas, it is possible to determine where within the cell the initial ionization occurred and therefore the position in the transverse plane through which the high energy particle passed. The drift velocity of electrons depends strongly on the nature of the gas. A helium based gas mixture with a ratio of He to C_3H_8 of 60:40 is used for the BESIII MDC. To precisely determine the three-dimensional trajectory of the charged particles, several layers of sense wires within the MDC are given a stereo angle. Of the 43 sense wire layers, 24 are oriented with a small angle with respect to the axial direction. This gives a resolution in the z direction (along the beam line) of 3 to 4 mm [70]. The resolution from a single cell is less than 130 μm in the transverse plane.

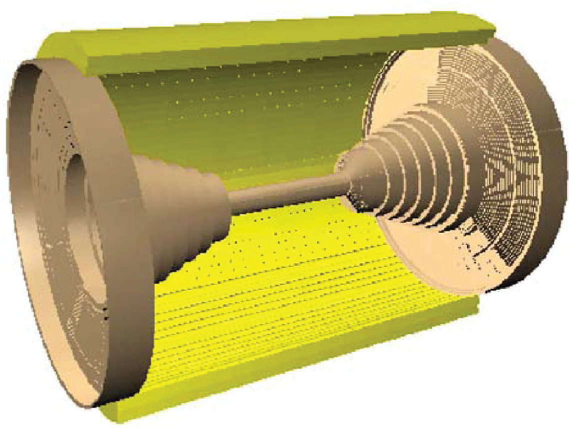

Figure 3.3: A schematic representation of the MDC is shown here. In total the MDC contains 28,640 wires.

The curvature of the track traced out by a charged particle in the MDC is related to the strength of the magnetic field and the momentum of the charged particle according to the Lorentz Force. Therefore, using knowledge on the strength of the magnetic field created by the solenoid magnet and a measurement of the curvature of the track in the MDC, it is possible to determine the momentum of charged particles. The momentum resolution of the MDC is expected to be less than 0.5% at 1 GeV/c^2.

In the BOSS framework, a tracking algorithm uses the hit patterns in the MDC to calculate track segments. These segments are then used to extrapolate circular patterns. These circular tracks are combined with the stereo hit information to generate helical particle trajectories. Finally, a fitting mechanism attempts to include additional hits that may come from the particle under investigation.

In addition to measuring the arrival time of the electron avalanche, the drift chamber facilitates a measurement of the specific ionization energy loss (dE/dx) of a high energy particle. The total amount of ions collected by the wire is proportional to the initial amount of ionization in the drift cell of interest. This information, gathered across different cells, gives a measure of the ionization energy loss. To a good approximation, the rate of energy deposition for charged particles depends only on the particle's velocity. Together with the measurement of the momentum from the tracking and magnetic field information, knowledge of the particle's velocity provides a means of identifying a particle by determining its mass. The expected dE/dx resolution is 6%.

3.4 Particle Identification

As discussed above, information on the dE/dx and momentum of a particle are useful for particle identification (PID). That is, a pion will exhibit a different dE/dx than a kaon or an electron. Thus, with information from the MDC, it is possible to determine the mass of a particle and therefore its identity. It is also possible to determine the identity of a particle by comparing the momentum measurement from the MDC with the velocity of the particle. The BOSS framework uses all of this information to produce a probability for each track to be produced by a certain charged particle. That is, each track will have a probability to come from an electron, pion, kaon, etc. This information may be useful in reducing backgrounds.

3.4.1 The Time of Flight System

A plastic scintillator time-of-flight system (TOF) directly encloses the MDC and provides the primary means of particle identification for the BESIII detector (Fig. 3.4). The barrel of the TOF consists of two layers of 88 trapezoidal shaped scintillating bars, each of which are 5 cm thick and 2.3 m long. Two photomultiplier tubes (PMTs) are attached to the end of the bars to read out the signal. The endcaps contain only a single layer each of 48 fan shaped counters with a width of 5 cm and length of 48 cm and is read out by another PMT.

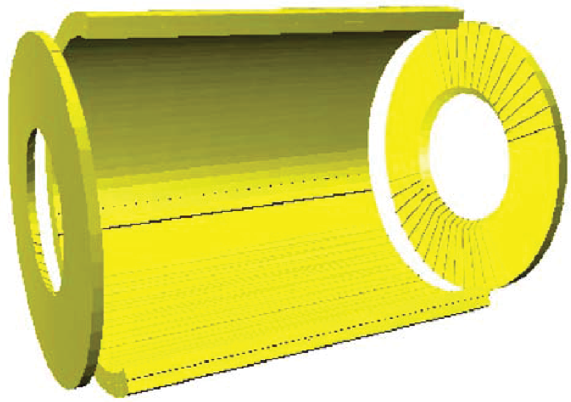

Figure 3.4: A schematic representation of the TOF is shown here. The barrel of the TOF consists of two layers of 88 trapezoidal shaped scintillating bars, while the endcaps contain only a single layer each of 48 fan shaped counters.

The TOF detector depends on the principle that charged particles passing through matter will excite the molecules they encounter. When this occurs in the plastic scintillator of the TOF, which is made of an organic scintillation material called Bicron BC-408, these excited molecules then release a small fraction of that energy as light. This light then bounces along the length of the scintillator bar until it reaches a PMT. A PMT is a light sensitive device, in which incoming photons knock electrons off of a series of metal plates. These electrons are then accelerated by an electric field, eventually colliding with additional sets of plates and knocking off more and more electrons. The resulting shower of electrons produces a measurable signal. This allows for a precision measurement of the time at which the charged particle hit the TOF. The timing resolution for the barrel (endcap) of the TOF is approximately 90 ps (120 ps).

By combining the timing measurements from the TOF and the time of the e^+e^-

collision at the interaction point, it is possible to determine the velocity of a charged particle moving through the detector. When coupled with the momentum measurement from the MDC, this provides a means to determine the identity of charged tracks.

3.4.2 The Muon System

A muon identifier (MUC) composed of resistive plate capacitors (RPCs) is useful for supplemental particle identification. This detector system is composed of nine (eight) layers of RPCs in the barrel (endcap) of the detector. The RPCs are placed between layers steel plates in the magnetic flux return of the solenoid magnet. High energy electrons will deposit most of their energy in the calorimetry system of the detector, but the much more massive muons are able to penetrate matter far more deeply than electrons (and other charge particles). Tracks reconstructed within the MUC are matched with an extrapolation of the tracks identified in the MDC. Thus, charged particles that are able to reach the MUC may be identified as muons.

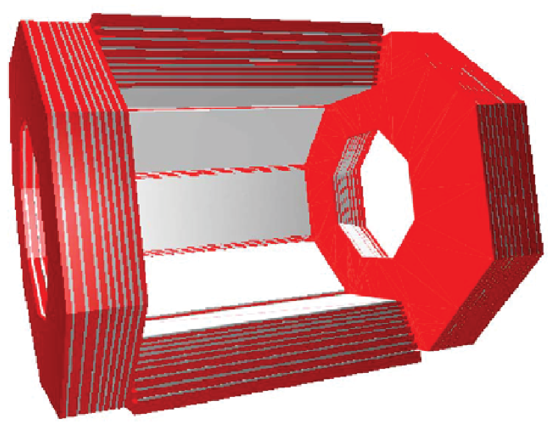

Figure 3.5: A schematic representation of the MUC is shown here. The MUC is composed of resistive plate capacitors and is useful for particle identification.

The total thickness of the steel plates in the MUC is 41 cm, with the innermost layers being an intentionally thin 4 cm. This allows for the detection of lower momentum muons, while still providing a dense material in which to absorb other charged particles. In this way, the minimum momentum of muons which can be effectively detected by the MUC is about 0.4 GeV/c^2. The MUC provides 2 cm position resolution for muons and covers 0.89 of 4π. Muons with momenta over 0.5 GeV/c^2 are detected with an efficiency greater than 90%. The efficiency of pions reaching the MUC is about 10% at this energy.

3.5 Calorimetry

The detection and measurement of neutral particles is very important in particle detectors, because many particles undergo a decay to final state photons. Neutral particles pass straight through the other detector components (barring any interaction with the detector material). The process of measuring the energies of photons takes place in devices called calorimeters.

3.5.1 The Electromagnetic Calorimeter

Between the TOF and the solenoid magnet is the Electromagnetic Calorimeter (EMC), which is used primarily to measure the energy and position of photons in the detector (Fig. 3.6). The EMC consists of 6240 CsI(Tl) crystals arranged in a barrel and two endcap sections. A gap of 5 cm separates the barrel and endcap of the EMC in order to allow for mechanical support and service lines of the inner detectors.

Cesium-iodide is a type of inorganic scintillator with a high light yield. Inorganic scintillators like these are useful for cases in which it is necessary to convert much of the energy of incident photons into a measurable signal. In the case of high energy particles, the dominant means by which these particles deposit energy in the calorimeter are bremsstrahlung radiation by charged particles and pair production of electrons and positrons by photons [1].

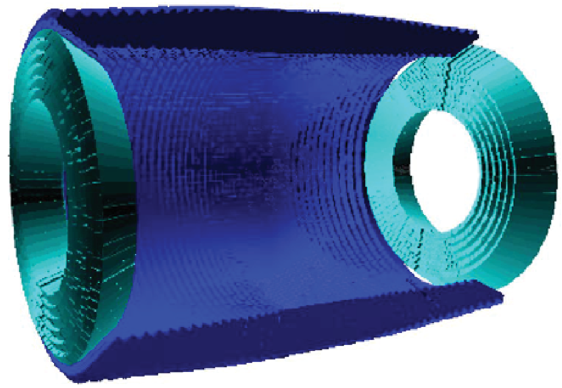

Figure 3.6: A schematic representation of the EMC is shown here. The EMC consists of 6240 CsI(Tl) crystals arranged in a barrel and two endcap sections.

When a high energy photon is incident upon the EMC, it will produce an electron-positron pair according to a probability distribution given by

$$\frac{dw}{dx} = \frac{1}{\lambda} e^{-x/\lambda}, \tag{3.1}$$

where λ is the average distance necessary for pair production. It is related to the radiation length, which is a characteristic of the material traversed by high energy photons and electrons, by $\lambda = \frac{9}{7} X_0$. The electrons and positrons produced in this manner will then emit bremsstrahlung radiation according to

$$-\left(\frac{dE}{dx}\right) = \frac{E}{X_0}. \tag{3.2}$$

In this context, the radiation length is a measure of the average distance over which an electron loses all but $\frac{1}{e}$ of its energy by bremsstrahlung. The photons which are produced in this event will then travel a certain distance in the crystal before pair-producing and the process is repeated. The resulting cascade of shower particles, including electrons, positrons and photons, creates a measurable signal in light sensitive devices. In the case of the BESIII EMC, this is achieved with Hamamatsu

S2744-08 photodiodes.

The signal detected in each EMC crystal is used to determine the energy deposited in that crystal. A clustering algorithm uses the energy information for each crystal to identify clusters of energy deposition in the EMC. Presumably, these are areas in which a photon has entered the calorimeter (though the cluster may be due to incident charged particles or electronic noise). Another algorithm identifies crystals with relative energy maxima and uses them to determine the number and characteristics of reconstructed showers. This includes the position and energy of the incident photons.

The CsI(Tl) crystals used in the EMC have a radiation length of about 1.85 cm. In order to absorb the maximum amount of energy from showers, the length of the crystals must be at least 10 to 15 times the radiation length. The BESIII EMC crystals are 28 cm in length, or 15 times the radiation length, with a gradually increasing cross section measuring 5.2 cm by 5.2 cm in the front and 6.4 cm by 6.4 cm in the rear. The barrel section of the EMC consists of 5,280 CsI(Tl) crystals, arranged into 44 rings of 120 crystals, while the remaining 960 crystals are contained in the endcaps, which are segmented into six rings of varying numbers of crystals. The crystals which make up the endcaps are irregularly shaped in order to avoid gaps in the detector apart from the segmentation between the barrel and endcap. With an angular coverage of about 93% of 4π, the EMC provides an energy resolution of 2.5% (5%) at 1.0 GeV and a position resolution of 6 mm (9 mm) in the barrel (endcap).

3.6 Data Summary

Over a total running time of a little more than 3 months in 2009 and 2012, the BESIII collaboration has collected the world's largest sample of J/ψ decays. This data sample was collected by running at a center of mass energy equal to the J/ψ mass (3.0969 GeV/c^2). The total luminosity of the sample is approximately 430 pb^{-1}, while the total number of J/ψ decays is determined to be $(1.3106 \pm 0.0072) \times 10^9$, where the error is statistical only. The analysis presented here utilizes the full J/ψ data sample as well as a sample of events collected below the J/ψ peak (3.080 GeV/c^2) in order to study continuum backgrounds.

Chapter 4

Experimental Methods

Much of the effort necessary to complete a physics analysis goes into isolating the events of interest, called the signal, while eliminating those events that resemble the signal but actually originate from some other process. In other words, the number of signal events must be maximized, while the number of background events must be minimized. This process is accomplished primarily by studying simulated events, called Monte Carlo (MC) events, whose features are predetermined. By comparing the distributions of measurable variables in the MC samples with what is visible in the data, it is possible to estimate the background that is present in the data. MC samples can come in several types. Inclusive MC samples contain all known processes and possibly some approximation of any remaining unknown decays. Exclusive MC (sometimes called signal MC) samples contain only one or more specific decay channels and are useful for studies of particular signal or background types.

Typically, the data sample is purified by applying selection criteria or "cuts" to different variables. For example, backgrounds like detector noise or out of time events may produce showers in the EMC. In other words, some showers do not correspond to a particle coming from the true event. By restricting the energy of photons, it may be possible to reduce or even eliminate these backgrounds while not severely reducing the number of true events. After all selection criteria are applied, it is possible to use a MC sample to calculate the reconstruction efficiency of the sample. That is, how many events remain from the original MC sample after reconstruction and selection criteria have been applied.

With the exception of backgrounds due to J/ψ decays to $\gamma\eta(')$, which are specifically addressed in the fitting procedure, the amplitude analysis presented here is performed with the assumption that all background events have been eliminated. Each event left in the sample is treated as a true signal event. Therefore, it is important to reduce the backgrounds in the sample as much as possible. Any remaining backgrounds may produce a systematic uncertainty in the results. Uncertainties of this type are studied by varying the selection criteria or fitting method.

4.1 The Reconstruction Software

Information coming from the BESIII detector subsystems is processed by the BESIII Offline Software System (BOSS) [72]. BOSS is an object-oriented framework that utilizes the C++ programming language. The interfaces and utilities which are useful for simulation, reconstruction and analysis are provided by the Gaudi package [73], and management of the software is performed with CMT [74].

This analysis is performed with data reconstructed with BOSS version 6.6.4. The data consist of $(1.3106 \pm 0.0072) \times 10^9$ J/ψ events, which were collected by BESIII at BEPCII in the two separate runs, one in 2009 and the other in 2012.

4.2 Detector Simulation

Selection criteria and background estimation are studied using a GEANT4-based MC simulation. The BESIII Object Oriented Simulation Tool (BOOST) [75] provides a description of the geometry, material composition, and detector response of the

BESIII detector. The MC generator KKMC [76], is used for the production of J/ψ mesons by e^+e^- annihilation, while BESEVTGEN [77] is used to generate the known decays of the J/ψ according to the world average values from the PDG [1]. Additionally, the unknown portion of the J/ψ decay spectrum is generated with the Lundcharm model [78].

An inclusive MC sample of 1.225×10^9 J/ψ decays, also reconstructed in BOSS version 6.6.4, is used for background analysis and signal isolation. Additional exclusive MC samples were generated in the same BOSS version for further investigation of particular backgrounds and for efficiency calculations. A phase space exclusive MC sample was generated using the AmpTools package and reconstructed in the BOSS framework for calculation of normalization integrals in the mass independent analysis.

4.3 Extracting the Reconstructed Data

A software package called FSFilter is implemented to extract the reconstruction information for each event in the data and MC samples. This package was designed by Ryan Mitchell to aid in the reconstruction of BESIII events that correspond to a particular reaction. FSFilter looks for events with the appropriate topology, like the number of tracks or photons in an event, and applies some loose restrictions, such as the typical photon angle and energy restrictions. The algorithm obtains this information by extracting the reconstruction objects from the BOSS environment. It can also perform any pertinent analysis procedures such as kinematic fitting. After all such procedures, FSFilter produces a ROOT file that contains all of the information that will be necessary for the analysis. This includes the four-momenta of the final state particles before and after the kinematic fit as well as other information like the χ^2 from a kinematic fit.

For the analysis presented here, FSFilter is asked to look for events that have a final state consisting of a photon and two π^0s. This requires a final state with at least five photons, each of which must satisfy a set of restrictions. Any photon that lands in the barrel of the detector must have an energy of at least 25 MeV, while any photon that lands in the endcap must have an energy of at least 50 MeV. The typical BESIII timing restriction on photons is relaxed due to the absence of charged tracks, which are used to determine the interaction time. The typical restriction only accepts showers that have a time within 700 ns of the time of interaction. Since the interaction time cannot be accurately measured for the reaction under study, each shower time must instead be within 500 ns of the time of the most energetic shower.

In addition to individual photons, the BOSS reconstruction framework generates objects that represent particles like the π^0, which decays to two photons. For every unique pair of photons in the event, BOSS gives a π^0 reconstruction object. This type of object contains information like the identity of the daughter photons and the χ^2 from any kinematic fit that is performed on the daughter particles. FSFilter looks for each π^0 object and applies the same photon restrictions described above to each of the two daughter photons. For this analysis, the invariant mass of the photon pair is required to fall within 28 MeV/c^2 of the π^0 rest mass. Additionally, the χ^2 from a 1C kinematic fit of the two photons to have an invariant mass equal to that of the π^0 is restricted to be less than 2500 (a very loose criterion).

FSFilter applied a 6C kinematic fit on any events that have the topology described above. This includes a 4C kinematic fit of the total four-momenta of the final state particles to come from a J/ψ meson. FSFilter also accounts for the small crossing angle of the beams in the detector which generates a non-zero momentum for the J/ψ. In addition to the 4C kinematic fit, each pair of photons coming from the π^0 reconstruction objects is constrained to have an invariant mass equal to that of a π^0. The resulting kinematic fit has $4 + 1 + 1 = 6$ constraints. Only events with a χ^2 from the 6C kinematic fit less than 600 are accepted for further analysis.

If more than 5 photons that satisfy the above criteria are found for a single event, all possible combinations of $\gamma\pi^0\pi^0$ are reconstructed. FSFilter analyzes each combination as though it came from a separate event. Theoretically speaking, only one such event represents the true event, while the other combinations will become a background to the signal. To account for this background, only the combination that has the smallest χ^2 from the 6C kinematic fit is retained for each event. This restriction is applied after all event selection criteria (discussed below) are applied.

4.4 Event Selection Criteria

In order to perform a mass independent amplitude analysis, it is necessary to extract a signal that is very clean. That is, it is necessary to reduce the size of any backgrounds to be as close to zero as possible. Any significant background contamination that remains must be addressed either in the fitting procedure itself or by introducing systematics uncertainties.

In the context of variables that are useful for signal isolation, some of the signal events will necessarily be eliminated when selection criteria are applied. In many cases it is possible to define a figure of merit, with which one is able determine the optimal selection criteria. For the case of the amplitude analysis presented here, the need to reduce the background to nearly zero implies that a figure of merit may not give the optimal outcome. Rather, the selection criteria must tend more strongly toward background reduction than to the retention of signal events.

4.4.1 Optimization

The $\pi^0\pi^0$ invariant mass spectrum for all events from the data and inclusive MC samples that pass the minimal selection criteria applied by the FSFilter algorithm are shown in Fig. 4.1. This sample has a background contamination on the order of 27% according to the inclusive MC sample. Significant backgrounds include J/ψ decays to $\gamma\eta$ ($\eta \to \pi^0\pi^0\pi^0$) and $\gamma\eta'$ ($\eta \to \eta\pi^0\pi^0; \eta \to \gamma\gamma$) as well as to $\omega\pi^0$ ($\omega \to \gamma\pi^0$). In order to further reduce the remaining backgrounds, a series of additional selection criteria are applied.

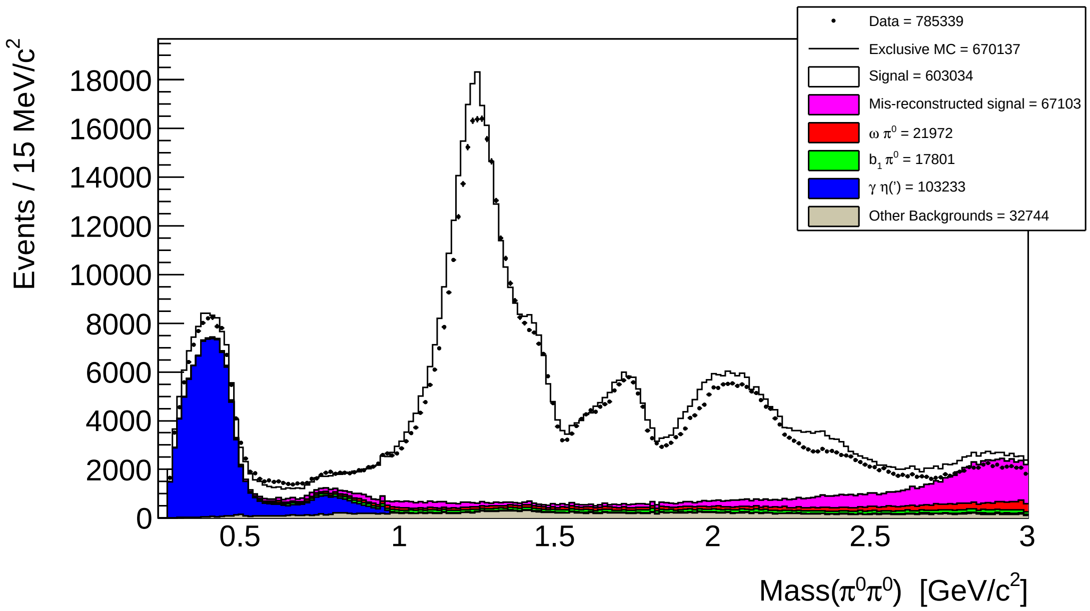

Figure 4.1: The $\pi^0\pi^0$ invariant mass spectrum is plotted here after only minimal event selection criteria are applied. The markers show the J/ψ data and the histograms indicate the backgrounds according to the inclusive and exclusive MC samples. The MC samples have been scaled to the size of the data sample after all selection criteria have been applied. Significant backgrounds from J/ψ decays to $\gamma\eta(')$ are visible, particularly below 0.6 GeV/c^2.

The most problematic backgrounds for this analysis are those from J/ψ decays to $\gamma\eta$ and $\gamma\eta'$. Each of these backgrounds consists only of final state photons (each of the π^0s and ηs decay into two photons). The reconstruction algorithm takes all combinations of five photons which have a reasonable probability to come from a final state of $\gamma\pi^0\pi^0$. Some combination of five of the seven photons coming from each of these final states may meet this criterion. In particular, if two of the photons from the π^0 or η decays are lost in the detector, the final state appears to have the event topology of interest. Statistically speaking, it is likely that such a background is significant. This will create a background contamination that peaks in the $\pi^0\pi^0$ invariant mass, the kinematic variable of greatest interest for this analysis.

While it is possible to reconstruct a seven photon final state as a five photon final state, the χ^2 of a kinematic fit to such a final state should be greater than that of a $\gamma\pi^0\pi^0$ event. In this way, it is possible to reduce the backgrounds containing decays to $\gamma\eta(')$ by restricting the χ^2_{6C} from the 6C kinematic fit. This criterion is tailored to address primarily the $\gamma\eta(')$ backgrounds and so is applied selectively to the invariant mass spectrum. Events with a $\pi^0\pi^0$ invariant mass below 0.99 GeV/c^2 (the region in which these backgrounds are significant) must have a χ^2_{6C} less than 20. Events above 0.99 GeV/c^2 need only have a χ^2_{6C} less than 60. The selection criterion in the high mass region is determined such that the backgrounds remaining after all selection requirements is on the order of 1%. The χ^2_{6C} distributions for these two regions are shown in Fig. 4.2. For clarity, these same distributions are plotted on a log scale in Fig. 4.3.

The result of the selection criteria on the χ^2_{6C} is to reduce the signal size by about 32%. While some portion of the $\gamma\eta(')$ backgrounds remains even after this restriction, the amount is now only about 0.3% of the signal size.

Several of the backgrounds to $\gamma\pi^0\pi^0$ actually have the same final state as the signal itself. These channels decay through a final state of Xπ^0 where the X decays to $\gamma\pi^0$. The most significant of these backgrounds comes from J/ψ decays to $\omega\pi^0$ ($\omega \rightarrow \gamma\pi^0$). The $\omega\pi^0$ background is apparent in the Dalitz-like plot shown in Fig. 4.4. Since the ω is very narrow, it is possible to greatly reduce this background by requiring that the invariant mass of each $\gamma\pi^0$ pair be at least 50 MeV/c^2 away from the ω mass (782.7 MeV/c^2) (Fig. 4.5).

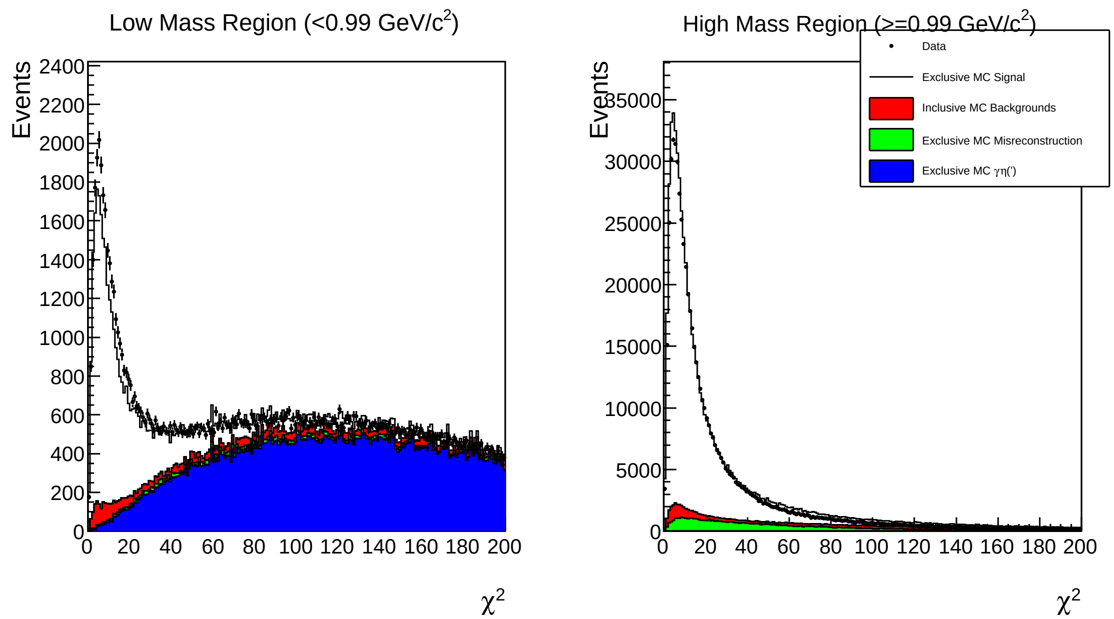

Figure 4.2: The χ^2 distribution from the 6C kinematic fit is plotted here after minimal event selection criteria are applied. The left (right) plot shows the χ^2 distribution for events with a $\pi^0\pi^0$ invariant mass below (above) 0.99 GeV/c^2. The markers are the J/ψ data and the histograms come from the inclusive and exclusive MC samples. Placing a restriction on the 6C χ^2 to be less than 20 in the low mass region is an effective means of reducing the background from J/ψ decays to $\gamma\eta(')$. In the high mass region, this requirement is relaxed to be less than 60.

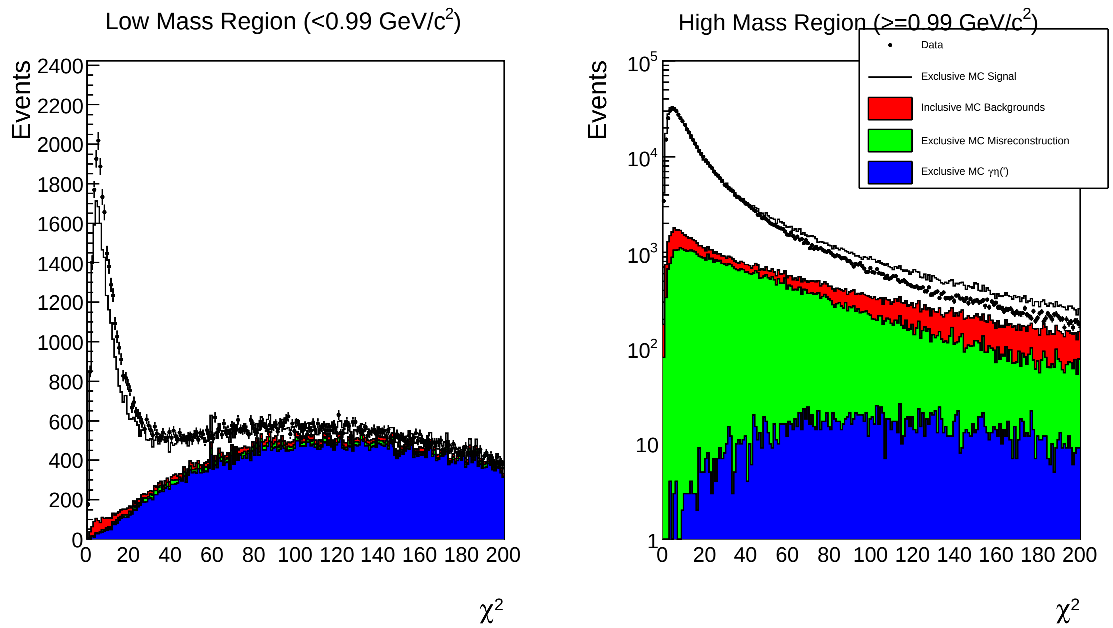

Figure 4.3: The χ^2 distribution from the 6C kinematic fit is plotted here before any event selection criteria are applied. The left (right) plot shows the χ^2 distribution for events with a $\pi^0\pi^0$ invariant mass below (above) 0.99 GeV/c^2. The markers are the J/ψ data and the histograms come from the inclusive and exclusive MC samples. Placing a restriction on the 6C χ^2 to be less than 20 in the low mass region is an effective means of reducing the background from J/ψ decays to $\gamma\eta(')$. In the high mass region, this requirement is relaxed to be less than 60.

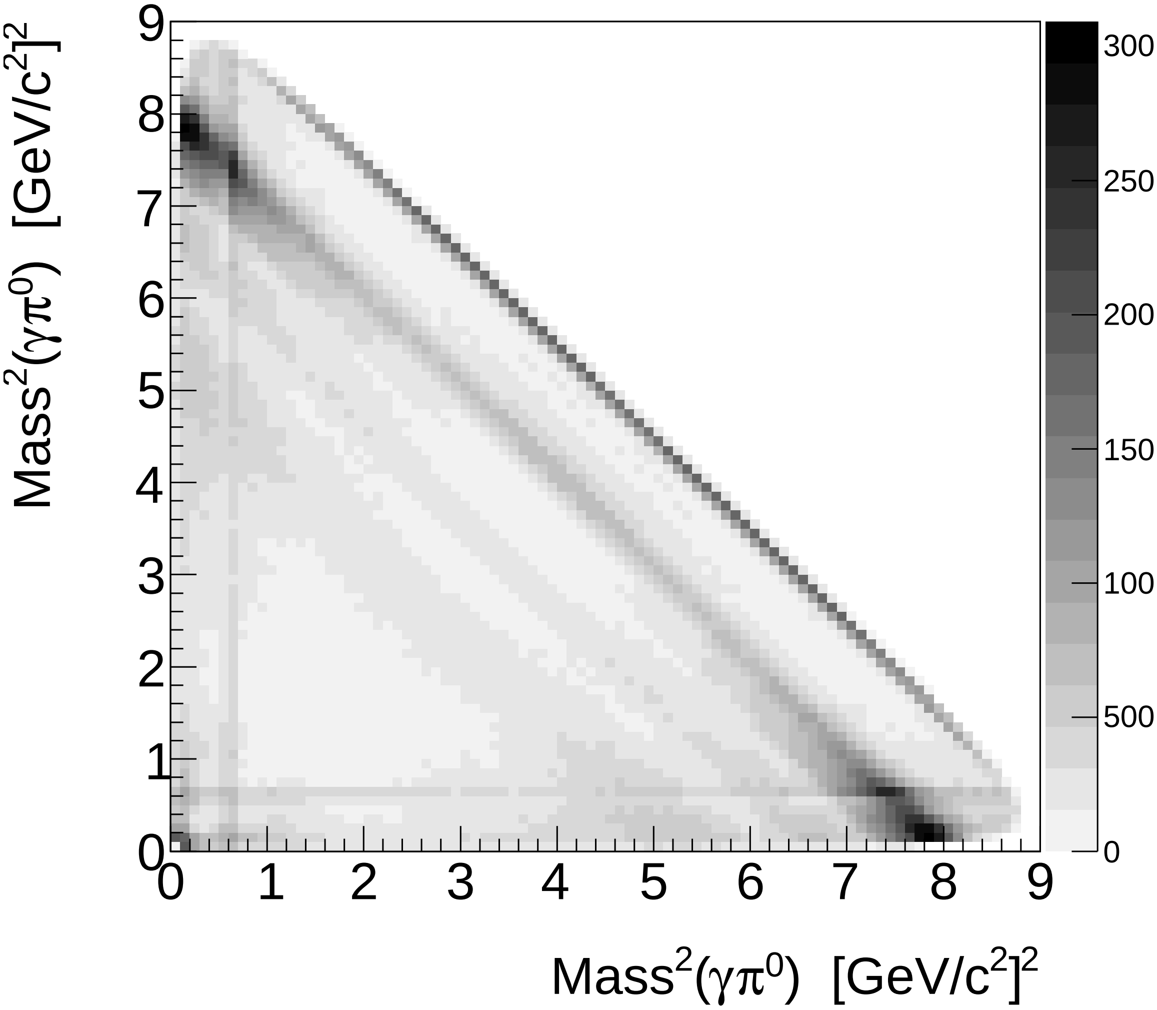

Figure 4.4: The Dalitz-like plot of the $\gamma\pi^0$ invariant mass is shown here after the selection criteria on the χ^2_{6C}.

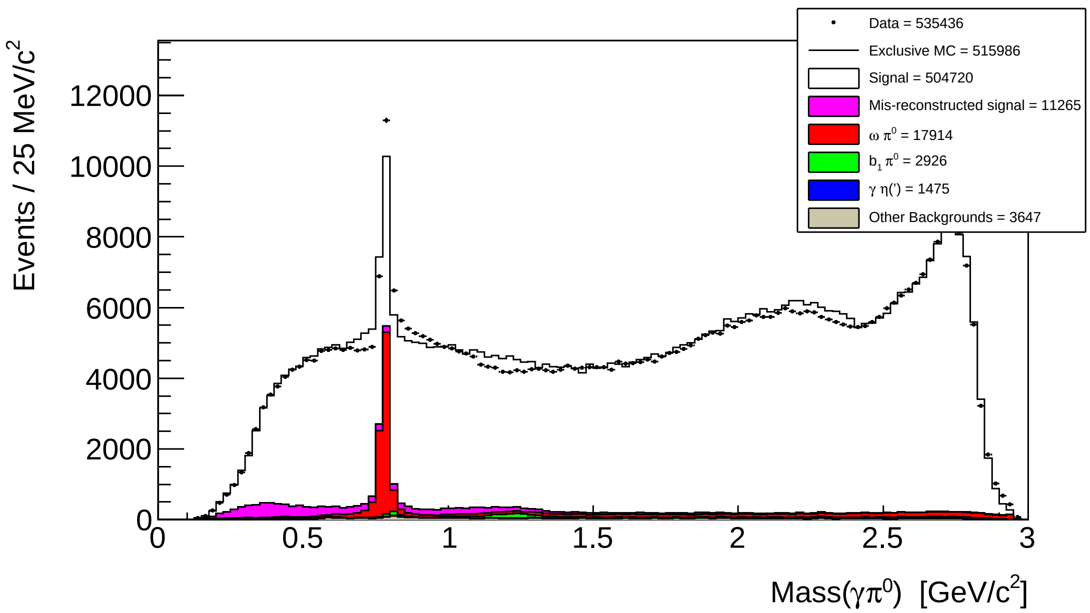

Figure 4.5: Backgrounds from J/ψ decays to $\omega\pi^0$ where the ω decays to $\gamma\pi^0$ are removed by restricting the invariant mass of each $\gamma\pi^0$ pair in an event to be at least 50 MeV/c^2 from the mass of the ω.

Some of the reconstructed events take as the radiative photon one of the photons from the π^0 decays. This is essentially a misreconstructed event that presents as a background to the signal. In order to reduce this background, the invariant mass of the radiative photon paired with any π^0 daughter photon is required to be greater than 0.15 GeV/c^2 4.6. Thus, it is very unlikely that the radiated photon actually came from a π^0 decay. This restriction reduces the size of the data sample by about 9%. The remaining misreconstructed background is approximately 0.14% of the size of the data sample.

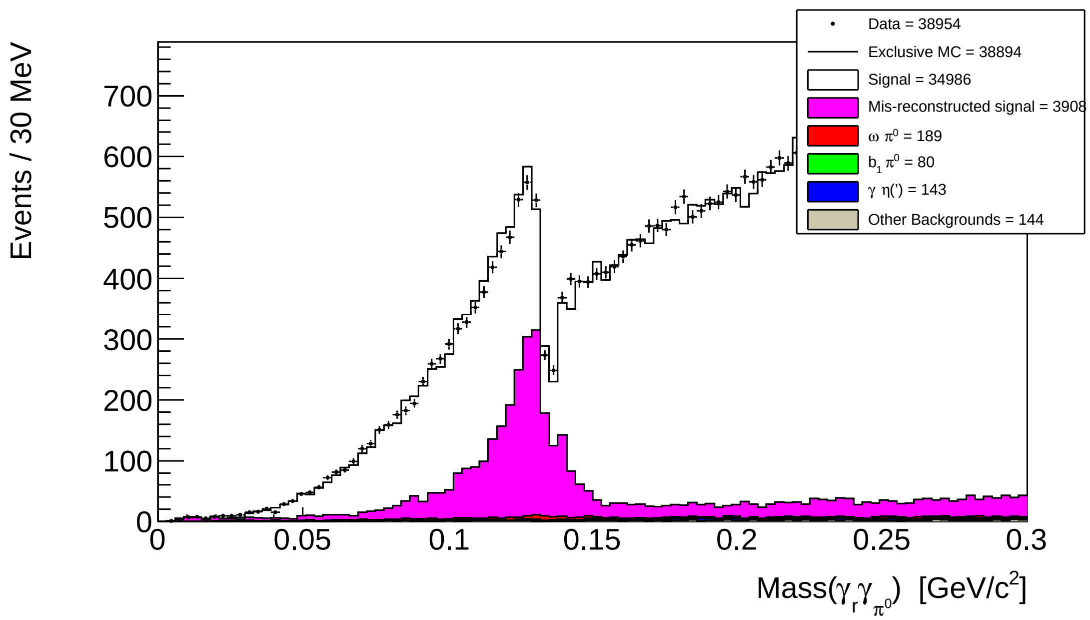

Figure 4.6: Misreconstructed events are reduced by requiring the invariant mass of the radiative photon paired with any π^0 daughter photon to be greater than 0.15 GeV/c^2. Each combination of the radiative photon, γ_r, and a π^0 daughter photon, γ_{π^0}, is plotted.

The left plot of Fig. 4.7 shows the generated invariant mass of the $\pi^0\pi^0$ pair as a function of its reconstructed invariant mass. The events that fall off of the diagonal represent the misreconstructed background. The events remaining after the restriction on the radiative photon are plotted on the right. Most of the misreconstructed background is removed by this restriction (Fig. 4.8 gives the efficiency for the signal and this background as a function of $\pi^0\pi^0$ invariant mass).

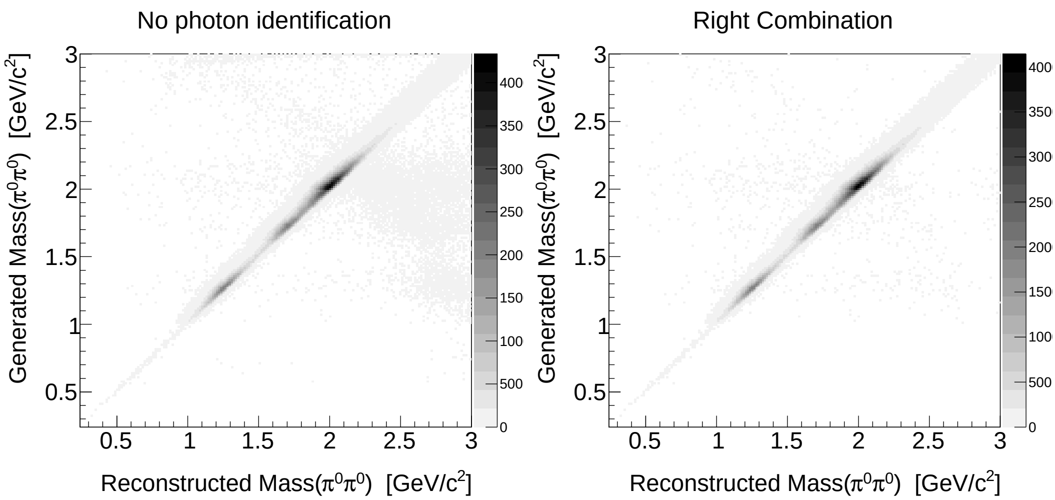

Figure 4.7: These two dimensional plots show the generated mass versus the reconstructed mass of the π^0 pair from the inclusive MC sample. A significant number of events are misreconstructed by swapping the radiative photon with one of the photons from a π^0. The plot on the left (right) shows the distribution before (after) the radiative photon selection criteria are applied. By restricting the likelihood that the radiative photon comes from a π^0, this background is greatly reduced.

After all event selection criteria are applied, the total number of background events is reduced to about 1.8% of the size of the signal according to the inclusive MC sample (Fig. 4.9). The number of events remaining in the data is 442,562. To measure the efficiency of these selection criteria, a set of phase space MC was reconstructed according to the same procedure described above. According to this sample, the efficiency across the full spectrum is 37.9%. The efficiency is plotted as a function of $\pi^0\pi^0$ invariant mass in Fig. 4.10. One additional source of backgrounds come from continuum events, in which the interaction does not resonate through a J/ψ. Continuum backgrounds are investigated with a data sample collected at a center of mass energy of 3.08 GeV. Only 247 events, which represents approximately

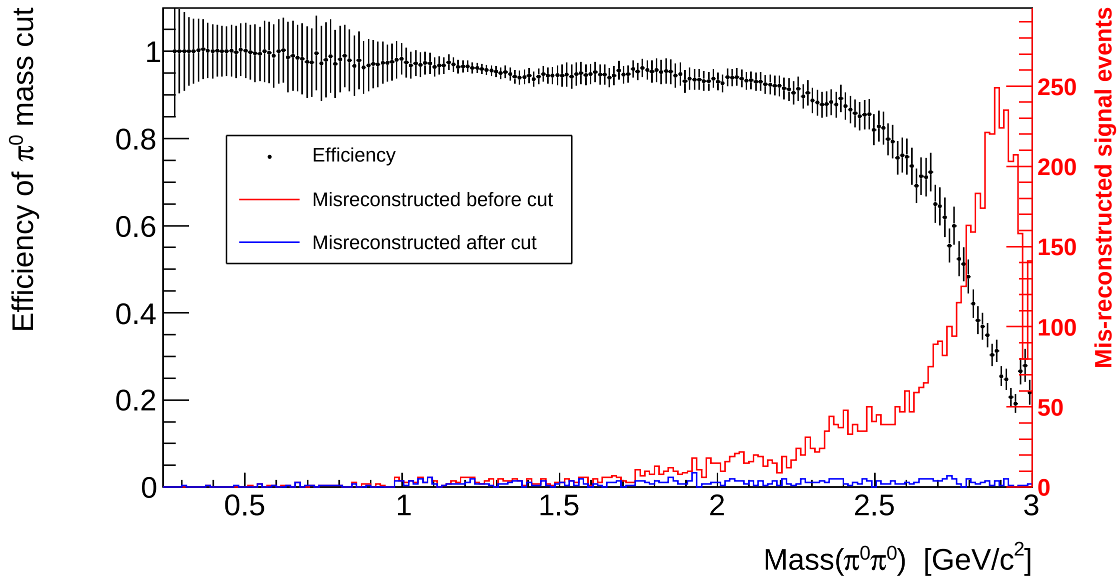

Figure 4.8: The signal efficiency of the selection criteria on the radiative photon according to an exclusive MC sample is shown here by the black markers. The number of misreconstructed events before the selection criteria on the radiative photon is given by the red histogram, while the number after the criteria are applied is shown by the blue histogram. The selection criteria on the radiative photon are very efficient in reducing this misreconstructed background.

0.8% of the signal when scaled by luminosity, survive after all signal isolation cuts.

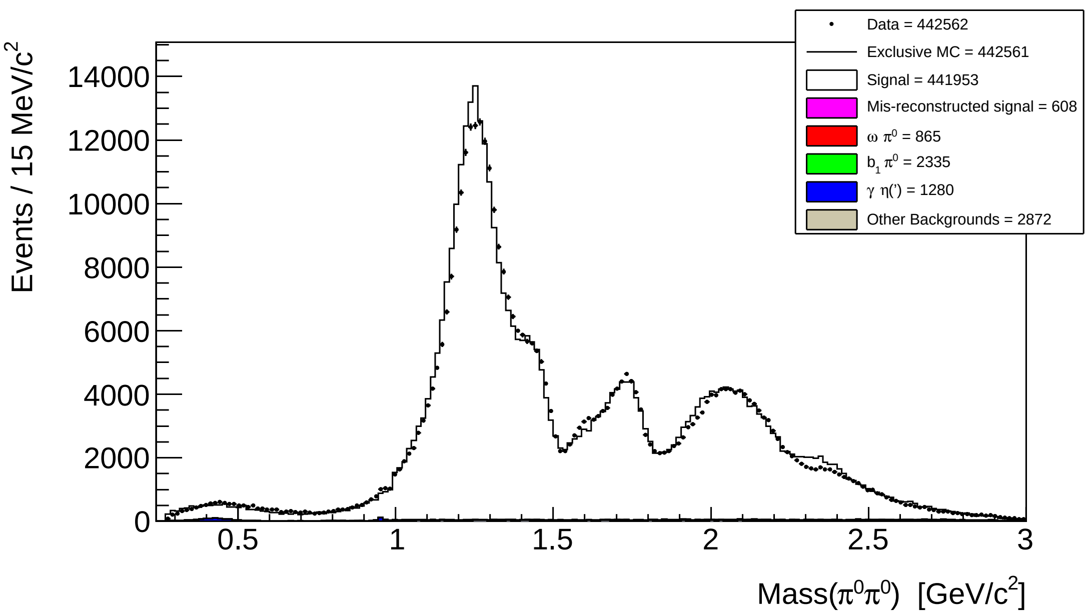

Figure 4.9: The $\pi^0\pi^0$ invariant mass spectrum is plotted here after all event selection criteria have been applied. The markers show the J/ψ data and the histograms come from the inclusive MC sample. The backgrounds have been reduced to the order of 1.2% of the signal (according to the inclusive MC sample).

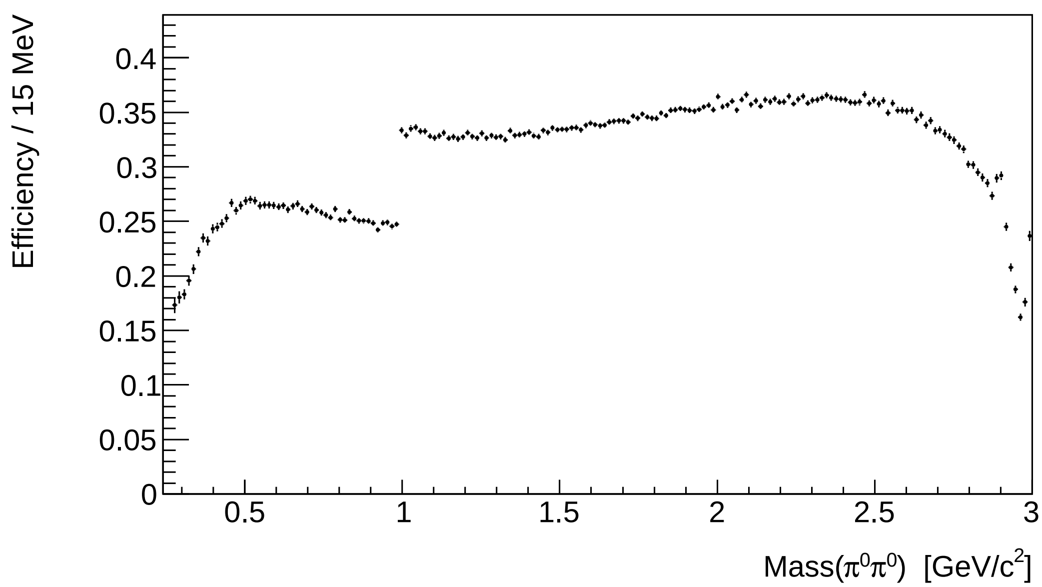

Figure 4.10: The efficiency is plotted here as a function of $\pi^0\pi^0$ invariant mass. The integrated efficiency across all mass bins is 37.9%.

4.4.2 Background Analysis

The primary remaining backgrounds after all selection criteria have been applied are the signal mimicking decays of the J/ψ to Xπ^0, where the X then decays to $\gamma\pi^0$. The types and amounts of the backgrounds which remain in the inclusive MC sample are listed in Table 4.1. The first two rows give the number of events in the data sample and in a continuum sample taken at 3.08 GeV respectively. The next three rows give the backgrounds for signal mimicking decays. Additional backgrounds include the decays of a J/ψ to $\gamma\eta(')$, which will be further discussed below, and a background due to misreconstruction of signal events.

Decay channel	Number of events
$J/\psi \to \gamma\pi^0\pi^0$ (data)	442,562
$J/\psi \to \gamma\pi^0\pi^0$ (continuum)	247
$J/\psi \to \omega\pi^0; \omega \to \gamma\pi^0$	865
$J/\psi \to \rho\pi^0; \rho \to \gamma\pi^0$	832
$J/\psi \to b_1\pi^0; b_1 \to \gamma\pi^0$	618
$J/\psi \to \gamma\eta; \eta \to 3\pi^0$	903
$J/\psi \to \gamma\eta'; \eta' \to \eta\pi^0\pi^0; \eta \to \gamma\gamma$	377
Misreconstructed signal events	608
$J/\psi \to b_1\pi^0; b_1 \to \omega\pi^0; \omega \to \gamma\pi^0$	1,717
$J/\psi \to \omega\pi^0\pi^0; \omega \to \gamma\pi^0$	829
$J/\psi \to \omega\eta; \omega \to \gamma\pi^0$	437
Other backgrounds	774
Total Background (MC)	7,960

Table 4.1: The number of events remaining after all selection criteria for each of a number of background channels is shown in the right column.

The decays of the J/ψ to $\gamma\eta(')$ introduce a challenge to the amplitude analysis. They both peak in the low mass region near interesting structures. The $\gamma\eta$ final state lies in the region of the $f_0(500)$, which is of particular interest to many theorists for its importance to Chiral Perturbation Theory (ChPT) [1, 79]. The $\gamma\eta'$ background peaks near the $f_0(980)$, which is also of particular interest due to its strong coupling to KK and its implications for a scalar meson nonet [23]. These backgrounds are therefore addressed by performing two independent analyses. One analysis treats these backgrounds as negligible while the other utilizes an exclusive MC sample to remove the background events from the fit. The presentation of both results makes it possible to study the uncertainties introduced by backgrounds of this type.

An exclusive MC sample consisting of J/ψ decays to $\gamma\eta(')$ is generated according to the branching fractions of these reactions given by the PDG [1]. This angular distributions of events in this sample are generated according to a model within BESEVTGEN called the JPE model. Each of the selection criteria discussed above is applied to the MC sample. The events that remain are plotted in Fig. 4.11. These events may be included in the amplitude analysis with a negative weight. In this way, when the exclusive MC sample is included in the fit, it has the effect of canceling out the remaining $\gamma\eta(')$ backgrounds in the data sample.

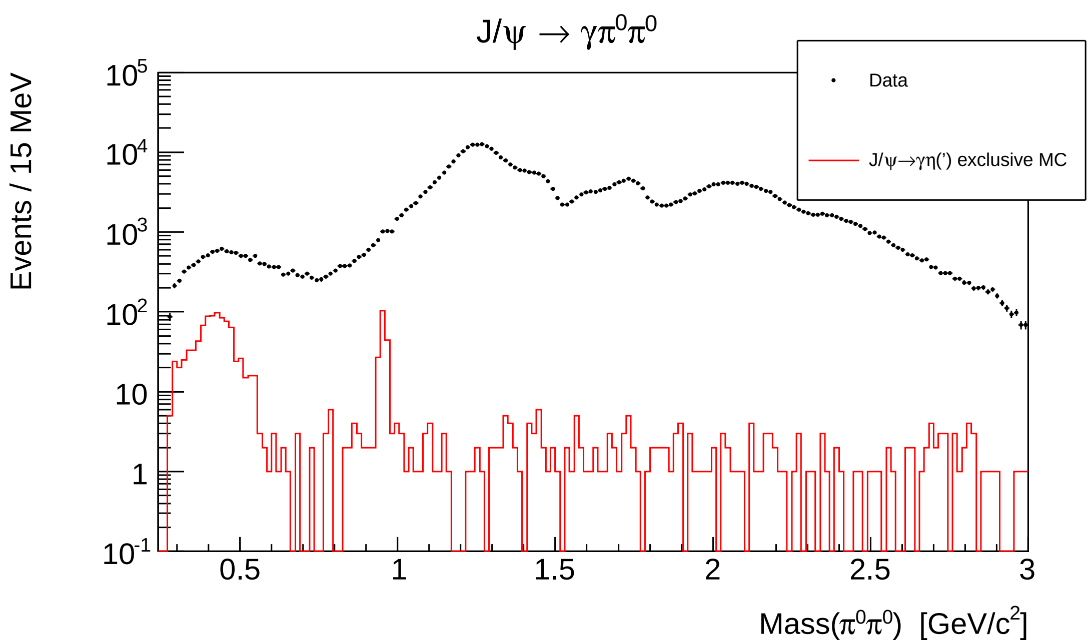

Figure 4.11: The combined data set is plotted here as the black markers. The $\gamma\eta(')$ backgrounds generated according to the PDG branching ratios (and the JPE model) are plotted as the blue histogram.

Continuum backgrounds are investigated with a data sample collected at a center of mass energy of 3.08 GeV, just below the J/ψ peak. Only 247 events (Fig. 4.12) survive after all signal isolation criteria. The continuum sample contains 29.14 pb^{-1}, while the data sample contains 430.84 pb^{-1}. After scaling by luminosity, the continuum background represents approximately 0.8% of the data sample. This suggests that backgrounds of this type are negligible for the amplitude analysis. A systematic uncertainty due to the background contamination is included in the branching ratio measurement.

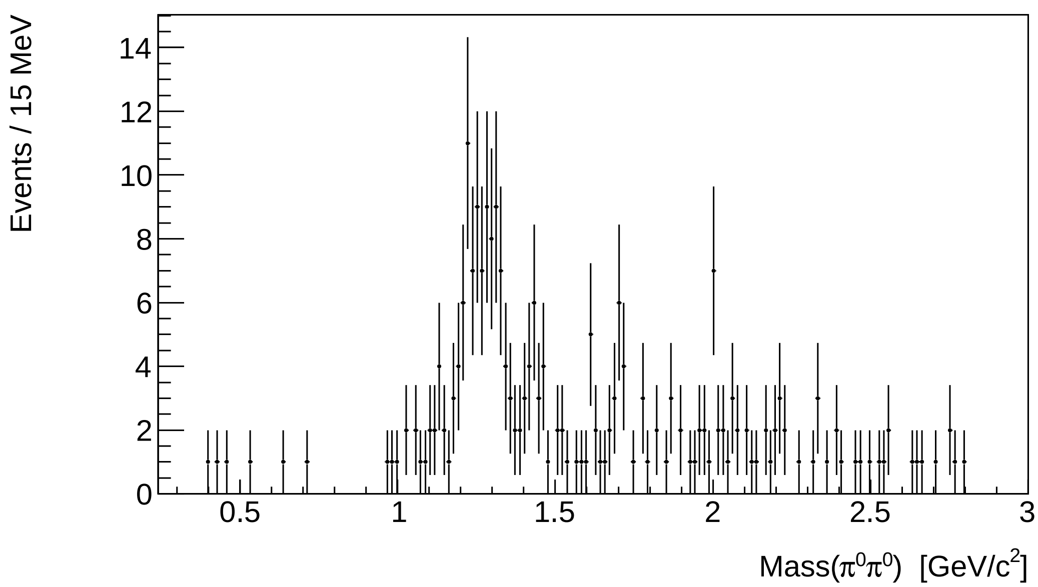

Figure 4.12: The distribution of continuum events that pass the selection criteria described above is shown here. Only 247 events remain, which correspond to less than 0.8% of the data sample, suggesting that this background is negligible.

Due to the fact that this analysis implements a 6C kinematic fit, it is not possible to study the π^0 sidebands. The ability to study sidebands is important, because it may be possible to take a photon from each true π^0 in the event and improperly combine them to form a false π^0. This would result in a background for the analysis. As an alternative means to investigate this possible background, the two photon invariant mass spectrum is studied under different conditions. The invariant mass spectrum for the wrong combination of photons (one from each π^0 object) is shown for the data before the χ^2 selection criteria in Fig. 4.13. Two bands are apparent in each distribution. For reference, the reconstructed two photon invariant mass spectrum for each π^0 object is shown in the left plot of Fig. 4.13. The two photon invariant mass distributions are shown in Fig. 4.14 after applying the restriction on the χ^2_{6C} from the kinematic fit. The vertical and horizontal bands are no longer apparent.

To further study this background, an exclusive MC sample was also utilized. This sample contains structures similar to those visible in the data and was generated using a Breit-Wigner parameterization, with the masses and widths taken from a mass dependent fit to the data (see Section 6.3). Each photon is compared with the truth information. To isolate the miscombination effect, the only events that are analyzed are those in which the four photons coming from the π^0 objects can be unambiguously matched by energies and angles to the four true π^0 daughter photons in the event. The energy tolerance is 0.05 GeV, while the angular tolerance on $\cos\theta$ is 0.03 (Fig. 4.15). The goal is then to determine how many of these events use the wrong combination of photons to make a π^0. This is accomplished by determining the number of events for which one reconstructed photon matches a photon from one generated π^0 while the partner of the reconstructed photon matches a photon from the other generated π^0.

Of the 438,635 events from the exclusive MC sample, 130,658 have photons that can be unambiguously matched to a generated photon. This means that only one reconstructed photon has values of energy and $\cos\theta$ near that of the truth information (energy tolerance = 0.05, $\cos\theta$ tolerance = 0.03 - see Fig. 4.15). Most of the other events (255,983) contain more than one reconstructed photon that can be matched to a single generated photon. Of the unambiguously matched events, only 752 events are misreconstructed (a background of about 0.6%). After the χ^2 cut, these numbers are reduced to 15 miscombined events out of 123,504 (a background of about 0.01%). Modification of the tolerances results in background sizes consistent with this value. This suggests that the background of this type is negligible.

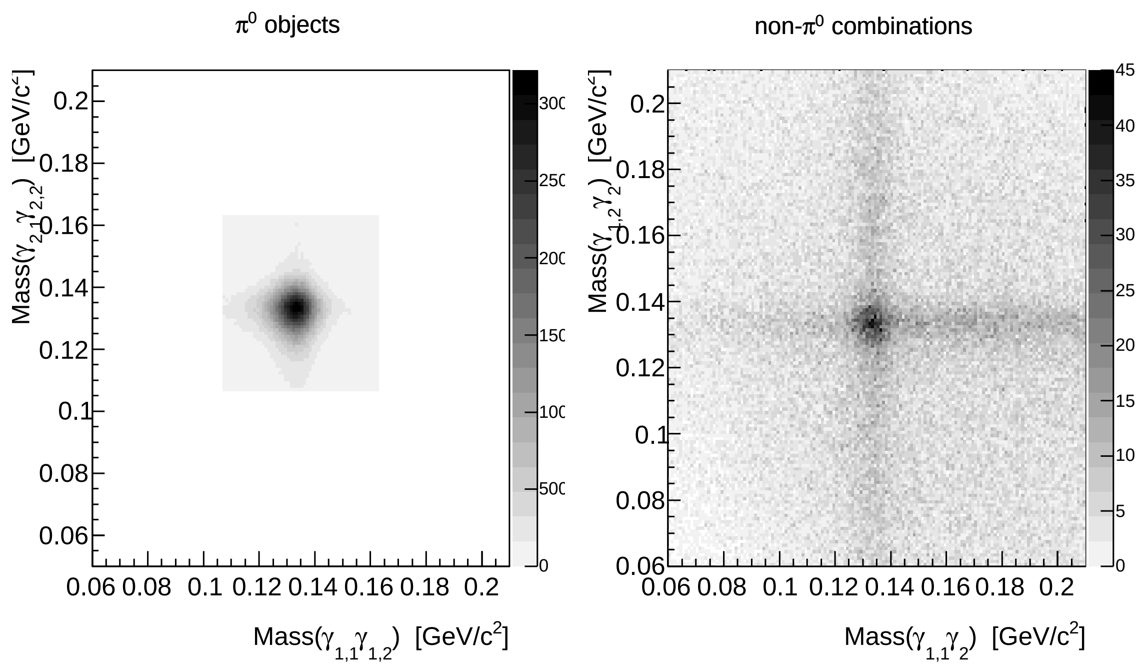

Figure 4.13: These plots show the invariant mass of two photon combinations before the 6C kinematic fit is applied. The first subscript gives the parent π^0 of the photon, while the second identifies the daughter. The left plot shows the two photon invariant mass distributions for photons that come from the same reconstructed π^0. The selection criteria for π^0s require the unconstrained π^0 mass to be between 0.107 and 0.163 GeV/c^2. The plot on the right shows all combinations of two photons coming from opposite π^0 objects. The normal reconstruction criteria (at least one photon of the appropriate energy, at least two π0s with appropriate unconstrained mass, etc.) are applied, but no additional selection criteria have been applied.

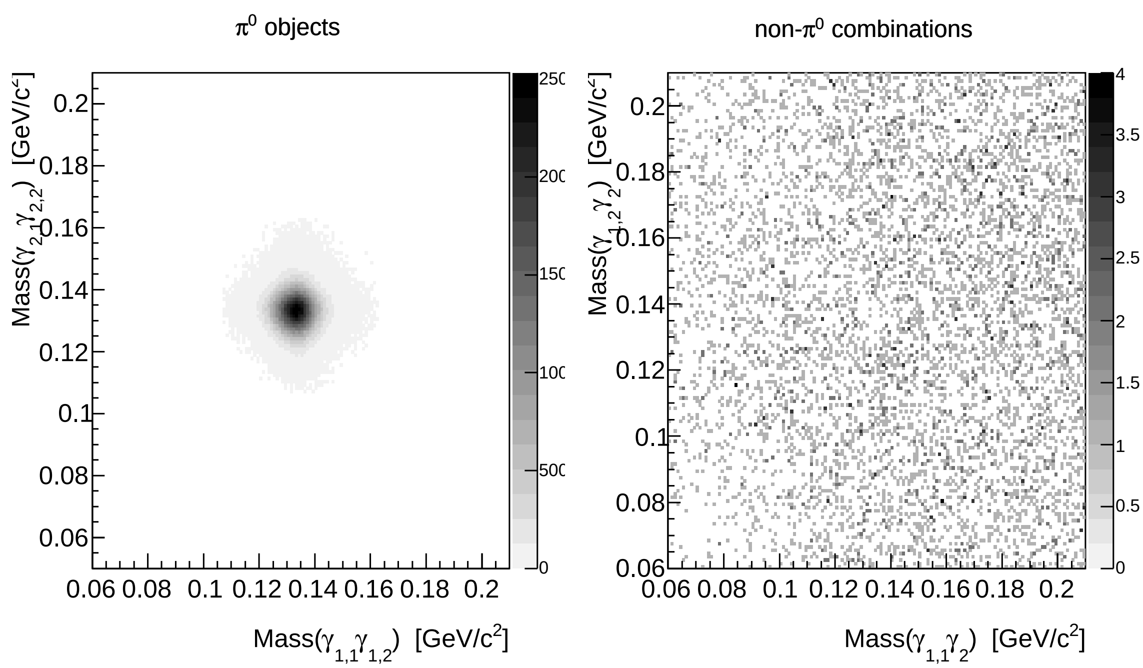

Figure 4.14: These plots are the same as those above, except that the signal isolation criteria has been placed on the kinematic fit χ^2_{6C}.

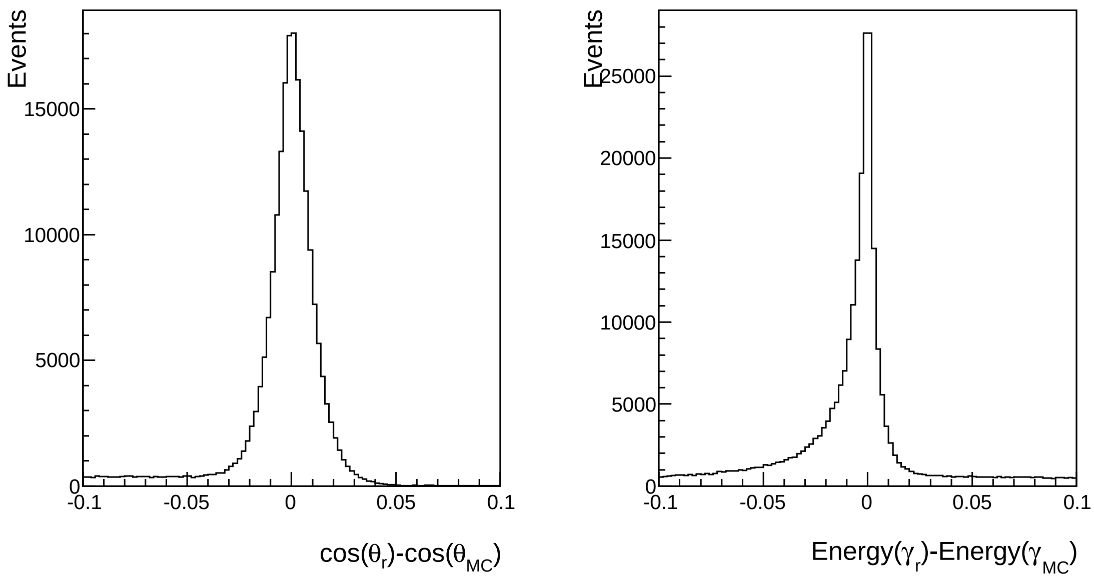

Figure 4.15: These plots show a comparison between a reconstructed photon and a generated photon. The absolute difference in $\cos\theta$ (left) for a matching pair of photons is required to be less than 0.03, while that for the energy (right) is required to be less than 0.05.

Chapter 5

Amplitude Analysis

One of the biggest challenges to meson spectroscopy in the low mass region is the presence of broad, overlapping states. Whereas the classical principle of superposition may be used to interpret a composite wave as a simple sum of the intensities of two or more waves, superposition in the quantum mechanical sense brings a new level of complexity to the problem. The intermediate states in a decay process are not independent of one another. Rather, the reaction is a quantum mechanical mixture of many different intermediate processes. In addition to measuring the intensity for each intermediate process, it is also necessary to consider the interference between them. Such an analysis is called an amplitude analysis because it investigates the reaction on the level of quantum mechanical amplitudes.

5.1 Introduction to Amplitude Analyses

An unbinned extended maximum likelihood fit is an analytical tool with which to measure one or more parameters that describe a physical process. This method requires a model that contains free parameters and predicts the probability of having an event with a particular topology. The true values for the parameters are approximated by maximizing the probability that the model matches the data.

Practically, an amplitude analysis is performed by fitting several quantum mechanical amplitudes to the observed distribution of events in a data sample. The amplitudes contain the production mechanism, dynamics of the interaction, and possibly also the decay of intermediate states. For radiative J/ψ decays to $\pi^0\pi^0$, the amplitudes may be factorized into a piece that contains the radiative transition of the J/ψ to an intermediate state X_{12} and a piece that contains the $\pi^0\pi^0$ interaction

$$U = \sum_{X=\pi\pi,KK,...} < J/\psi|H_{EM}|\gamma_{J_\gamma} X_{12} > \times < X_{12}|H_{QCD}|\pi^0\pi^0 >, \tag{5.1}$$

where the sum includes any pseudoscalar-pseudoscalar final state. The part of the amplitude that describes the $\pi^0\pi^0$ interaction is the piece that is of greatest interest for this study.

The amplitude in Eq. 5.1 may be parameterized in various ways depending on the desired information. For example, if the goal of an analysis is to measure characteristics like the masses and widths of intermediate resonances, it may be useful to parameterize the part of the amplitude that describes the $\pi^0\pi^0$ interaction with a sum of Breit-Wigner functions. A mass dependent approach such as this introduces model dependencies, which are necessary to explain the final state interactions. The free parameters in the fit then contain the couplings of radiative J/ψ decays to each $\pi^0\pi^0$ resonance. Unfortunately, these couplings are only useful in the context of the model being used.

Another possible method to perform the amplitude analysis is to bin the data sample as a function of $\pi^0\pi^0$ invariant mass and to absorb the part of the amplitude that describes the interaction of final state particles into the free parameters. In this mass independent method, the free parameters contain the dynamical function that describes the $\pi^0\pi^0$ interactions, which is assumed to be constant across some small range of $\pi^0\pi^0$ invariant mass (the bin size). By performing a fit in each bin, the dynamical function is replaced by a table of complex numbers. While it is not possible to extract quantities like branching fractions from the results of a mass independent analysis, this method is useful because any arbitrary model may be fit to the results for each amplitude. This is not possible with only the results of a mass dependent analysis.

For the mass independent method, the amplitude for an event at some position in phase space $\vec{x}$ is given by

$$U(\vec{x}) = V(\vec{x})A(\vec{x}), \tag{5.2}$$

where $V(\vec{x})$ contains the product of the coupling of the amplitude to the radiative J/ψ decay and the piece of the amplitude that describes the $\pi^0\pi^0$ interaction. Then $A(\vec{x})$ contains the piece of the amplitude that describes the decay and is determined by the kinematics of an event. In each fit, the production coefficients, $V\vec{x}$, are replaced by free parameters, V. The intensity function $I(\vec{x})$, which represents the density of events at some position in phase space $\vec{x}$, is given by

$$I(\vec{x}) = \sum_{\beta} \left| \sum_{\alpha} V_{\alpha,\beta} A_{\alpha,\beta}(\vec{x}) \right|^2 . \tag{5.3}$$

The coherent sum over α includes the different accessible amplitudes and the incoherent sum over β includes the observables of the reaction. For the reaction under study, the observables are the polarization of the J/ψ, M= ± 1, and the helicity of the radiative photon, $\lambda_\gamma = \pm 1$. The free parameters are constrained to be the same for each of the four incoherent sums.

To extract the couplings, $V_{\alpha.\beta}$, an unbinned extended maximum likelihood fit is performed in each bin of $\pi^0\pi^0$ invariant mass. The probability to make N independent observations of a quantity X (X_1, ..., X_N) is given by a joint probability density function (pdf)

$$P(X|\theta) = P(X_1, ..., X_N|\theta) = \prod_{i=1}^{N} f(X_i|\theta), \tag{5.4}$$

where $f(X|\theta)$ is the probability density function (pdf) to observe a quantity X with a set of parameters θ. When the variable quantity X is replaced by experiment observations $\vec{x}$, this quantity no longer represents a probability. Instead, it is called a likelihood

$$L(\vec{x}, \theta) = \prod_{i=1}^{N} f(\vec{x}_i|\theta). \tag{5.5}$$

The true value for the parameters θ may be estimated by determining the values θ^0 for which the likelihood function is maximized [80].

If a data sample is entirely free of backgrounds, the likelihood function is constructed as

$$L(\vec{x}, \theta) = \prod_{i=1}^{N_{sig}} f(\vec{x}_i|\theta). \tag{5.6}$$

The number of events in the pure sample is given by N_{sig}. Now, the likelihood may be written

$$L(\vec{x}, \theta) = \prod_{i=1}^{N_{sig}} f(\vec{x}_i|\theta) \prod_{j=1}^{N_{bkg}} f(\vec{x}_j|\theta) \prod_{k=1}^{N_{bkg}} f(\vec{x}_k|\theta)^{-1}, \tag{5.7}$$

where an additional joint pdf, which describes the reaction for background events, has been multiplied and divided. Consider now a more realistic data sample that consists not only of signal events, N_{sig}, but also some number of background events, N_{bkg}. Then the first two factors of Eq. 5.7 are simply the joint pdf for the entire (contaminated) data sample, but the likelihood represents only that of the pure signal since the background joint pdf has also been divided. Now, for a given data set, any backgrounds remaining after selection criteria have been applied are difficult to distinguish from the true signal. Rather than using the true background to determine the background joint pdf, it is therefore necessary to approximate it using an exclusive

MC sample. That is,

$$\prod_{i=1}^{N_{MC}} f(\vec{x}_i|\theta)^{-w_i} \approx \prod_{i=1}^{N_{bkg}} f(\vec{x}_i|\theta)^{-1}, \tag{5.8}$$

where the weight, w_i, is necessary for scaling purposes. For example, if the MC sample is twice the size of the expected background, a weight factor of 0.5 is necessary. Finally, the likelihood function may be written

$$L(\vec{x},\theta) = \prod_{i=1}^{N_{data}} f(\vec{x}_i|\theta) \prod_{k=1}^{N_{MC}} f(\vec{x}_k|\theta)^{-w_k}. \tag{5.9}$$

For the analysis presented here, each data event is unweighted (has a weight of 1).

The probability to find an event in the detector at some location in phase space, $\vec{x}$, is given by

$$f(\vec{x}|\theta) = \frac{\eta(\vec{x})I(\vec{x}|\theta)}{\int \eta(\vec{x})I(\vec{x}|\theta)dx}, \tag{5.10}$$

where $\eta(\vec{x})$ is the efficiency of the detector to find an event at $\vec{x}$ (1 if the event is detected, 0 if not) after all selection criteria have been applied. For a physics model that predicts a number of events μ, the likelihood is given by the probability of observing N events multiplied by a Poisson distribution of N events with a mean of μ,

$$L(\vec{x},\theta) = \frac{(e^{-\mu}\mu^N)}{N!} \prod_{i=1}^{N} \frac{\eta(\vec{x_i})I(\vec{x_i}|\theta)}{\int \eta(\vec{x})I(\vec{x}|\theta)d\vec{x}}. \tag{5.11}$$

Here the set of variables θ to be approximated are the production amplitudes, $V_{\alpha,\beta}$. The integral

$$\int \eta(\vec{x})I(\vec{x}|\theta)d\vec{x} \tag{5.12}$$

is simply the expected number of events μ.

Rather than maximizing the likelihood, it is computationally preferable to minimize -2 $\ln L$. Note here that maximizing $\ln L$ (or minimizing -2 $\ln L$) also maximizes L. Also, by expanding the log likelihood function it is possible to drop terms that are constant in $V_{\alpha,\beta}$ since they merely result in the addition of a constant value to the likelihood and do not affect the minimization. The log likelihood, with like terms canceled, is given by

$$\ln L = \sum_{i=1}^{N} \ln I(\vec{x_i}|\theta) - \int \eta(\vec{x})I(\vec{x}|\theta)d\vec{x}, \tag{5.13}$$

where the constant factors,

$$\sum_{i=1}^{N} \ln \eta(\vec{x_i}) - \ln N!, \tag{5.14}$$

are dropped. The second term in Eq. 5.13 may be separated into a piece containing the free parameters and a piece that may be pre-computed using a large phase space MC sample,

$$\int \eta(\vec{x})I(\vec{x}|\theta)d\vec{x} = \int \eta(\vec{x}) \sum_{\alpha,\alpha'} V_\alpha A_\alpha(\vec{x})V^*_{\alpha'}A^*_{\alpha'}(\vec{x})d\vec{x} = \sum_{\alpha,\alpha'} V_\alpha V^*_{\alpha'}\phi_{\alpha,\alpha'}, \tag{5.15}$$

where $\phi_{\alpha,\alpha'}$ represents the normalization integral. Since $\eta(\vec{x})$ is equal to one for accepted events and zero otherwise, the normalization integral may be approximated using a flat distribution of MC events, N_{acc} of which are accepted from a sample of N_{gen} events. Then,

$$\phi_{\alpha,\alpha'} = \frac{U}{N_{gen}} \sum_{i=1}^{N_{acc}} A_\alpha(\vec{x_i})A^*_{\alpha'}(\vec{x_i}), \tag{5.16}$$

where U is the volume of phase space and may be absorbed into the production amplitudes V_α,

$$V'_{\alpha,\beta} = V_{\alpha,\beta}\sqrt{U}. \tag{5.17}$$

This transformation results in an overall shift in the log likelihood and does not affect the intensity distribution.

For the case of background subtraction in the likelihood as in Eq. 5.9, the likelihood is given by

$$L(\vec{x}|\theta) = \frac{(e^{-\mu}\mu^N)}{N!}\prod_{i=1}^{N}\frac{\eta(\vec{x_i})I(\vec{x_i}|\theta)}{\int\eta(\vec{x})I(\vec{x}|\theta)d\vec{x}} \times \frac{(e^{-\mu'}\mu'^{N_{MC}})}{N_{MC}!}\prod_{k=1}^{N_{MC}}\left[\frac{\eta(\vec{x_k})I(\vec{x_k}|\theta)}{\int\eta(\vec{x})I(\vec{x}|\theta)d\vec{x}}\right]^{-w_k}, \tag{5.18}$$

where μ' is the expected number of background events and N_{MC} is the number of background events in the MC sample. Note that μ' is independent of $V_{\alpha,\beta}$. Here again, by taking the natural log of the likelihood equation and dropping terms constant in $V_{\alpha,\beta}$,

$$\ln L = \sum_{i=1}^{N}\ln I(\vec{x_i}) - \sum_{k=1}^{N_{MC}} w_k \ln I(\vec{x_k}) - \int \eta(\vec{x})I(\vec{x})d\vec{x}, \tag{5.19}$$

where the weights w_k of the background events are all equal to -1.

5.2 The Mass Independent Amplitude Analysis

The primary goal of the mass independent analysis is to extract the function that describes the interaction of the two pseudoscalars ($\pi^0\pi^0$). For a "model independent" approach of this type, the decay is parameterized such that the couplings contain the $\pi^0\pi^0$ interaction. As described above, these will become the (complex) fit parameters, which are extracted from a fit to the data. The decay amplitudes, $A_{\alpha,\beta}(\vec{x_i})$, contain the angular distributions of the final state particles. These decay amplitudes are determined solely from event kinematics and are described more fully below.

Once again, the mass independent analysis is directed toward providing a set of results that have as few model dependencies as possible. Results like these can be utilized in a more complete analysis of the scalar spectrum. For example, results of this type are expected to be useful in a K-matrix analysis, as they provide a complementary source of hadronic production to that of pion beam and $p\bar{p}$ experiments [37]. While it is possible to perform a K-matrix analysis on the $\pi^0\pi^0$ spectrum from radiative J/ψ decays, the results can be better constrained with data from radiative

J/ψ decays to other channels like K_sK_s and $\eta\eta$. A more complete K-matrix analysis will therefore be delayed until results on these other channels are prepared.

While the mass independent analysis is intended to be as model independent as possible, some assumptions must be made. These assumptions include requiring that the intensity function for each amplitude and that of the phase difference be continuous across the $\pi^0\pi^0$ invariant mass spectrum. Additionally, each set of amplitudes with the same J^{PC} are constrained to have the same phase below the KK threshold. This latter constraint comes from the assumption that the vertex factors associated with the production process are purely real numbers unless additional channels are available. Above the KK threshold, though, rescattering effects may become significant. This has the potential to generated phase differences between the amplitudes of the same J^{PC}.

A difficulty arises when the constraint on the phases is relaxed. When this happens, the intensity is no longer uniquely determined. That is, ambiguities appear in the fit beyond the non-trivial ambiguities associated with the construction of the fit function. Each of these types of ambiguities are discussed more fully below. In an effort to provide as much detail as possible, the mass independent analysis is repeated with and without the phase constraint applied above the KK threshold. In this way, any study that is performed using the results of this analysis may either enforce the constraint on the phases of the 2^{++} amplitudes or not. For example, if a model which predicts minimal rescattering, the mass independent results with the phase constraint enforced provide greater accuracy. This constraint may even be applied selectively to specific regions of invariant mass.

The amplitude analysis is performed with the assumption that all backgrounds have been eliminated. While this seems like a plausible assumption for most of the $\pi^0\pi^0$ invariant mass spectrum, significant backgrounds from J/ψ decays to $\gamma\eta$ and $\gamma\eta'$ exist below 1 GeV. Rather than inflate the errors of these results according to the uncertainty introduced by these backgrounds, which would not take into account the bin-to-bin correlations, the mass independent analysis is repeated with and without the $\gamma\eta(')$ background subtraction. The background subtraction is accomplished according to the procedure discussing in section 4.4.2. Recall that the ratio of events from the reaction $J/\psi \to \gamma\eta(')$ that survive the event selection criteria for the $\gamma\pi^0\pi^0$ final state is very small. Minor changes to the modeling of the former decay may have a large effect on the backgrounds to the latter. Therefore, the systematic difference between the two sets of results, which treat the backgrounds differently, is taken as the systematic uncertainty due to backgrounds of this type. This is important for any studies that take the results of this analysis as inputs.

For each data set, the mass independent analysis is carried out by performing an extended maximum likelihood fit in each bin. The MIGRAD algorithm is used in the MINUIT framework to minimize -2 $\ln L$. A covariance matrix is estimated at each step of the algorithm, but is generally not sufficiently accurate. To obtain a more accurate estimate of the covariance matrix, the HESSE method is applied after minimization. This algorithm determines the covariance matrix by calculating the matrix of second derivatives at the minimum. The results are culled by applying constraints on certain MINUIT flags. The fit must converge, have an accurate error matrix, and an estimated distance to the minimum (an estimate of the goodness of the fit) of less than 10^{-5}.

In each bin, the solution with the minimum value of -2 $\ln L$ is retained as the "best" solution. Any other solutions that have values of -2 $\ln L$ within 1 unit of the minimum and parameter values that are distinct from the best solution (and any other results that are retained) are also kept. The issue of ambiguities in the fit is discussed below and in Appendix A. The choice of nominal solutions is discussed in the results section.

5.2.1 Mass Binning

In order to study the interaction between two pseudoscalars as a function of the $\pi^0\pi^0$ invariant mass, it is necessary to bin the data as finely as possible without losing information. If the binning is too fine, the statistics in each bin may be reduced to such a degree that the errors from the fit would make the results useless. Also, it is important that the resolution of the measured quantity (in this case the invariant mass of the π^0 pair) does not exceed the bin size.

The large size of the J/ψ data set collected at BESIII allows for very fine binning. The bin size for the mass independent analysis is set to 15 MeV/c^2, which is somewhat larger than the $\pi^0\pi^0$ mass resolution. To determine the mass resolution, an exclusive MC sample was generated according to phase space for the radiative J/ψ decay to $\pi^0\pi^0$. For each, event, the difference between the generated and reconstructed $\pi^0\pi^0$ invariant mass is fitted with a double Crystal Ball shape (Fig. 5.1). The double Crystal Ball shape is essentially the superposition of two Crystal Ball shapes, each of which must have the same mass, width, and number of events [81]. This shape was used in order to account for the tails of the distribution that are visible on either side of the peak. The width of the Gaussian core, measured to be about 9 MeV/c^2, was taken as the mass resolution.

To probe the effect of the energy of the radiative photon on the mass resolution of the $\pi^0\pi^0$ pair, the phase space MC sample is divided into bins of photon energy. In each bin, the resolution is measured as described above. A slight shift is noted for mid-range photon energies, but the resolution is no greater than about 11 MeV/c^2 (Fig. 5.2). A bin size of 15 MeV/c^2 is therefore a reasonable choice.

5.2.2 The Radiative Multipole Basis

The amplitude for radiative J/ψ decays to $\pi^0\pi^0$ can be determined in different bases depending on the information of interest. For example, in the helicity basis, the amplitude depends on the angular momentum and helicity of the $\pi^0\pi^0$ resonance as well as the angular momentum and polarization of the J/ψ. It is also possible to redefine the basis such that the dependence of the amplitudes is shifted to the angular momentum and helicity of the radiative photon. In this way it is possible to relate the amplitudes to radiative multipole transitions. Such a basis is useful because it allows for physical arguments about the amplitudes. For example, a model may suggest that the E1 radiative transition should dominate over the M2 transition.

In the radiative multipole basis, the amplitude for $J/\psi \to \gamma\pi^0\pi^0$ is given by

$$U(\vec{x}) = \sum_{J_\gamma, j_{12}, \mu_{12}} N_{J_\gamma} N_{j_{12}} D^{J}_{M,\mu_{12}-\lambda_\gamma}(\pi + \phi_\gamma, \pi - \theta_\gamma, \phi_1) d^{j_{12}}_{\mu_{12},0}(\theta_1) \frac{1 + P_{12}(-1)^{j_{12}}}{2} \frac{1 + (-1)^{j_{12}}}{2}$$
$$\langle J_\gamma - \lambda_\gamma; j_{12}\mu_{12} | J\mu_{12} - \lambda_\gamma \rangle \frac{1}{\sqrt{2}} [\delta_{\lambda_\gamma,1} + \delta_{\lambda_\gamma,-1} P_{12} (-1)^{J_\gamma - 1}] T_{J_\gamma j_{12}}(s_{12}) \tag{5.20}$$

where $\vec{x}$ describes the kinematics of the event. The parity, total angular momentum, and helicity of the pair of pseudoscalars are given by P_{ij}, j_{ij}, and μ_{ij}, respectively. The angular momentum of the photon, J_γ, is related to the nuclear radiative decays. The possible values of J_γ are limited by the conservation of angular momentum. The helicity of the radiative photon is given by λ_γ. The total angular momentum and polarization of the J/ψ are given by J and M, respectively. Finally, $N_j = \sqrt{\frac{2j+1}{4\pi}}$ is a normalization factor.

The angles (ϕ_γ, θ_γ, 0) are the azimuthal and polar angles of the photon in the rest frame of the J/ψ. The angles (ϕ_1, θ_1, 0) are the azimuthal and polar angles of one π^0 in the rest frame of the $\pi^0\pi^0$ pair, with the -z axis along the direction of the photon momentum. The π^0 momenta in this frame are given by $\mathbf{q}_1 + \mathbf{q}_2 = 0$.

Parity is a conserved quantity for strong and electromagnetic interactions. Hence, for J/ψ radiative decays, $P_{12} = (-1)^{j_{12}}$ must be positive. This means that the only intermediate states avaiable have $j_{12}^{P_{12}} = 0^+, 2^+, 4^+$, etc. Additionally, isospin symmetry in strong interactions requires $I_{12}^{G_{12}}$ for the intermediate state to be 0^+ (isoscalar). The dynamical amplitude $T_{J_\gamma j_{12}}(s_{12})$ describes the $\pi^0\pi^0$ interaction as a function of center of mass energy, s_{12}, and may be parametrized in different ways. In order to minimize the model dependence of the mass independent analysis, the dynamical amplitude is replaced by a (complex) free parameter in the unbinned maximum likelihood fit. Thus, the amplitude is given by

$$U(\vec{x}) = V(\vec{x})A(\vec{x}), \tag{5.21}$$

where

$$\begin{aligned} A_{\alpha,\beta}(\vec{x}) =& N_{J_\gamma} N_{j_{12}} D^{J}_{M,\mu_{12}-\lambda_\gamma}(\pi+\phi_\gamma, \pi-\theta_\gamma, \phi_1) \\ & d^{j_{12}}_{\mu_{12},0}(\theta_1) \frac{1+P_{12}(-1)^{j_{12}}}{2} \frac{1+(-1)^{j_{12}}}{2} \\ & \langle J_\gamma - \lambda_\gamma; j_{12}\mu_{12} | J\mu_{12}-\lambda_\gamma \rangle \\ & \frac{1}{\sqrt{2}}[\delta_{\lambda_\gamma,1} + \delta_{\lambda_\gamma,-1} P_{12}(-1)^{J_\gamma - 1}], \end{aligned} \tag{5.22}$$

and α represents the unique amplitudes accesible for the given set of observables, β. In this case, α includes the anguar momentum of the photon, J_γ, the angular momentum of the intermediate state, j_{12}, and its helicity, μ_{12}. The index β includes the polarization of the J/ψ, M, and the helicity of the raditive photon, λ_γ.

Any amplitude with total angular momentum greater than zero will have three components (the 0^{++} amplitude has only an E1 component). Thus, the 2^{++} amplitude has components relating to E1, M2, and E3 radiative transitions. While any amplitude with even total angular momentum and positive parity and charge conjugation are accessible for this decay, preliminary fits suggest that the 4^{++} amplitude is not significant in this region. For this reason, only the 0^{++} and 2^{++} amplitudes are included in the fits.

5.3 Ambiguities in the Amplitude Analysis

Since the intensity distribution, to which the amplitudes are fit, is constructed from the squares of the coherent sums of amplitudes, it is possible to identify multiple sets of amplitudes that give identical values for the intensity. In this way, multiple solutions may give comparable values of -2 $\ln L$ for a particular fit. For the $\gamma\pi^0\pi^0$ final state, two types of ambiguities are present. Trivial ambiguities may be partially addressed by applying a phase convention to the results of the fits. Non-trivial ambiguities represent a more challenging problem to the analysis and cannot be eliminated without introducing model dependencies.

5.3.1 Trivial Ambiguities

While it is not possible in principle to measure the absolute phase of the amplitudes (the fit function contains an absolute square), it is possible to study the relative phases between amplitudes. For the fits in each bin, one of the amplitudes is constrained to be real. The phase difference between this and the other amplitudes can then be determined for each mass bin.

A set of trivial ambiguities arises due to the possibility of applying a complex conjugation to each amplitude without changing the intensity distribution, Eq. 5.13. This has the effect of multiplying only the imaginary pieces of each amplitude by -1, and therefore changing the sign of the phase difference with respect to the reference amplitude. This issue is partially resolved by establishing a phase convention. In this case, the amplitude that is constrained to be real is required to be positive.

The remaining ambiguity is due to the inability to determine the absolute phase. That is, the total phase of the amplitudes may be either positive or negative (the intensity is unchanged when each amplitude is multiplied by a factor of -1). This ambiguity introduces the added complication that when a phase difference approaches zero, it is impossible to determine if the phase difference changes sign. For clarity, only positive phase differences are plotted. Any analyses taking these results as input should also include the various permutations of the phase differences. The intensity distributions are redundant for each permutation of phase differences.

5.3.2 Non-trivial Ambiguities

In an amplitude analysis, the angular dependence of the intensity function is the driving mechanism to determine the fractional intensity of each amplitude. That is, each of the amplitudes has a particular angular distribution, which is used to discriminate between it and the other amplitudes. By writing out the angular dependence of the intensity function, it is possible to show that the freedom for the relative phases to float for components of a given amplitude (2^{++} E1, M2, and E3, for example) generates an ambiguity in the intensity distribution. The very construction of the intensity allows for the existence of multiple sets of amplitudes that give the exact same intensity distribution. The ambiguities that appear in this analysis are described more fully in Appendix A below. Only two such ambiguous solutions are present. Rather than make an argument as to which solution is the physical solution, both sets of results from the mass independent analysis are presented.

5.4 The Mass Dependent Amplitude Analysis

Many amplitude analyses performed to date have utilized a set of interfering Breit-Wigner line shapes to describe the structures present in the data. This method has obvious flaws for wide, overlapping states (such as violating unitarity). Nevertheless, a Breit-Wigner parameterization of the $\gamma\pi^0\pi^0$ spectrum may provide a useful means of comparing the results of this analysis with previous studies. The results of such an analysis may also be useful in a comparison with the results of the mass independent analysis. That is, it may be useful to show whether the mass independent solution gives a fair representation of the data in comparison to the results using a mass dependent parameterization. With that goal in mind, a mass dependent amplitude analysis using interfering Breit-Wigner functions is performed in addition to the mass independent analysis.

A few words on the K-matrix approach are appropriate here. While this method also has some flaws, a K-matrix parameterization is generally considered to be a more appropriate method than a Breit-Wigner parameterization to extract information on wide and overlapping states. The K-matrix formalism accounts for unitarity constraints and can accommodate multiple overlapping resonances from the same amplitude. Additionally, the formalism allows for a couple channel analysis to difference final states. For a review of the K-matrix formalism, see for example Ref. [82].

One of the ultimate goals of the analysis of the pseudoscalar-pseudoscalar spectrum in radiative J/ψ decays is to perform just such a parameterization. A K-matrix analysis, though, is likely to change significantly with the addition of more channels like $\gamma K_S K_S$. Therefore, rather than perform a K-matrix analysis on the $\pi^0\pi^0$ system, a full analysis of this type is delayed until data on additional channels is ready.

The results of the mass dependent analysis are products of (complex) vertex factors, which are related to the coupling strength of each resonance in an amplitude. By extracting these values, it is possible to determine the fractional intensity for each resonance. Measurements of the mass and width of significant resonances are also possible with this method. Of course, these results should be considered only for comparative reasons.

The mass dependent analysis is performed with the same assumptions as the mass independent analysis (aside from the parameterization of the $\pi^0\pi^0$ interaction). That is, the three components of the 2^{++} amplitude are not constrained to have the same phase. In fact, the 2^{++} amplitude is relatively well understood experimentally.

Contributions to this amplitude come primarily from the $f_2(1270)$ and the $f_2'(1525)$, with a few other less well defined resonances above 1.5 GeV/c^2. Rather, the region of greatest interest is the 0^{++} amplitude.

To first order, a parameterization of this type would proceed according to the isobar model. In the simplest approximation, this relates to simple s-channel production. This is somewhat reasonable given that the photon does not interact in the final state. This means that the amplitude is a product of two vertex factors and a Breit-Wigner propagator,

$$A_X = f_{X;J/\psi,\gamma} BW(X) f^*_{X;\pi^0\pi^0}. \tag{5.23}$$

Now, in order to preserve time reversal invariance, this amplitude should be equal to the reverse process,

$$A_X = f^*_{X;J/\psi,\gamma} BW(X) f_{X;\pi^0\pi^0}, \tag{5.24}$$

which implies that the product of vertex factors must be real. For a parameterization of this type, then, one would expect the production amplitudes (the fit parameters) to be real. A failure of the fit to describe the data under these assumptions would imply that other effects are causing the couplings to become complex. This is a fairly common assumption [1]. Under these considerations, interference effects near the threshold of the $f_2'(1525)$, which has a strong coupling to the KK final state, lead to the expectation that the 2^{++} amplitudes to be complex. Therefore, the coupling for each amplitude in the mass dependent analysis is allowed to be complex.

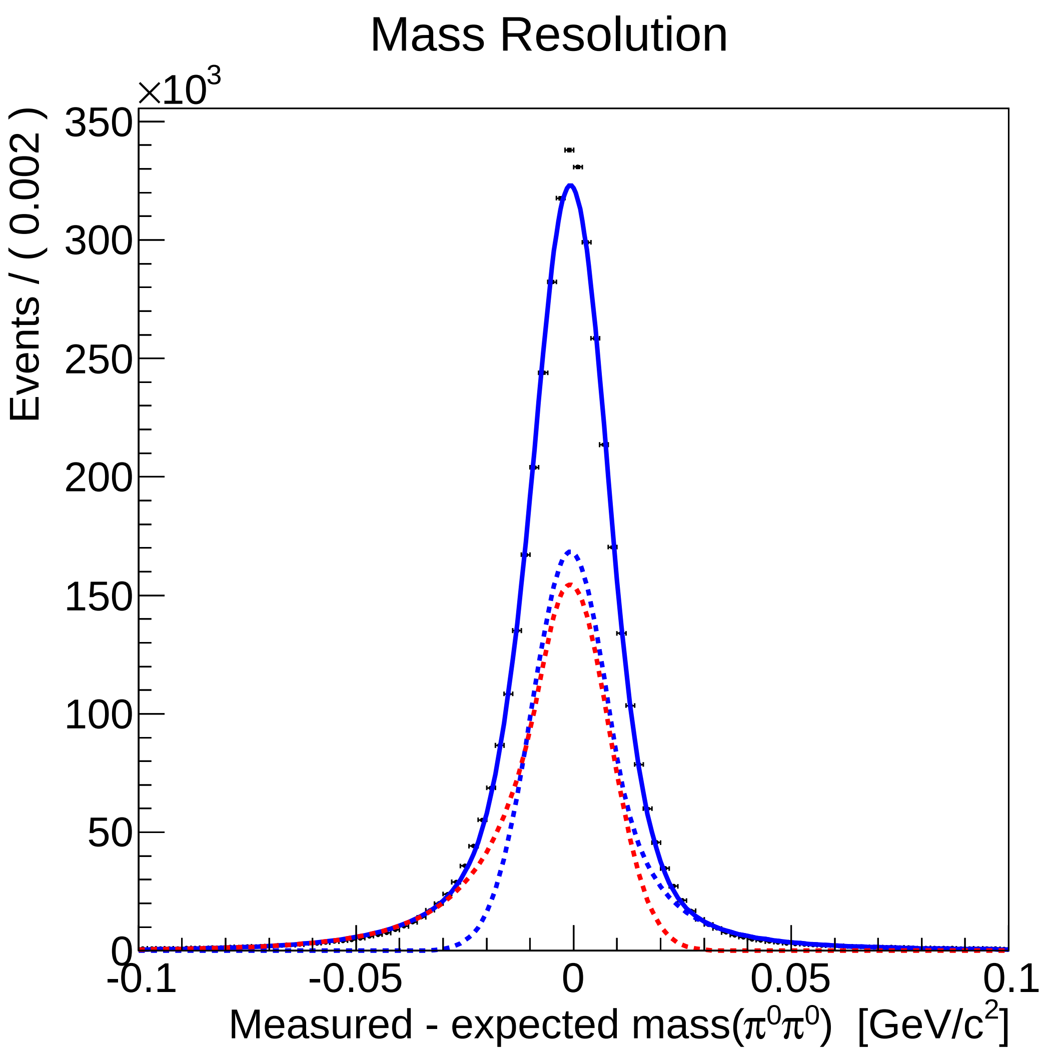

Figure 5.1: The $\pi^0\pi^0$ mass resolution is determined by fitting a double Crystal Ball function to the invariant mass of each π^0 pair in a phase space exclusive MC sample.

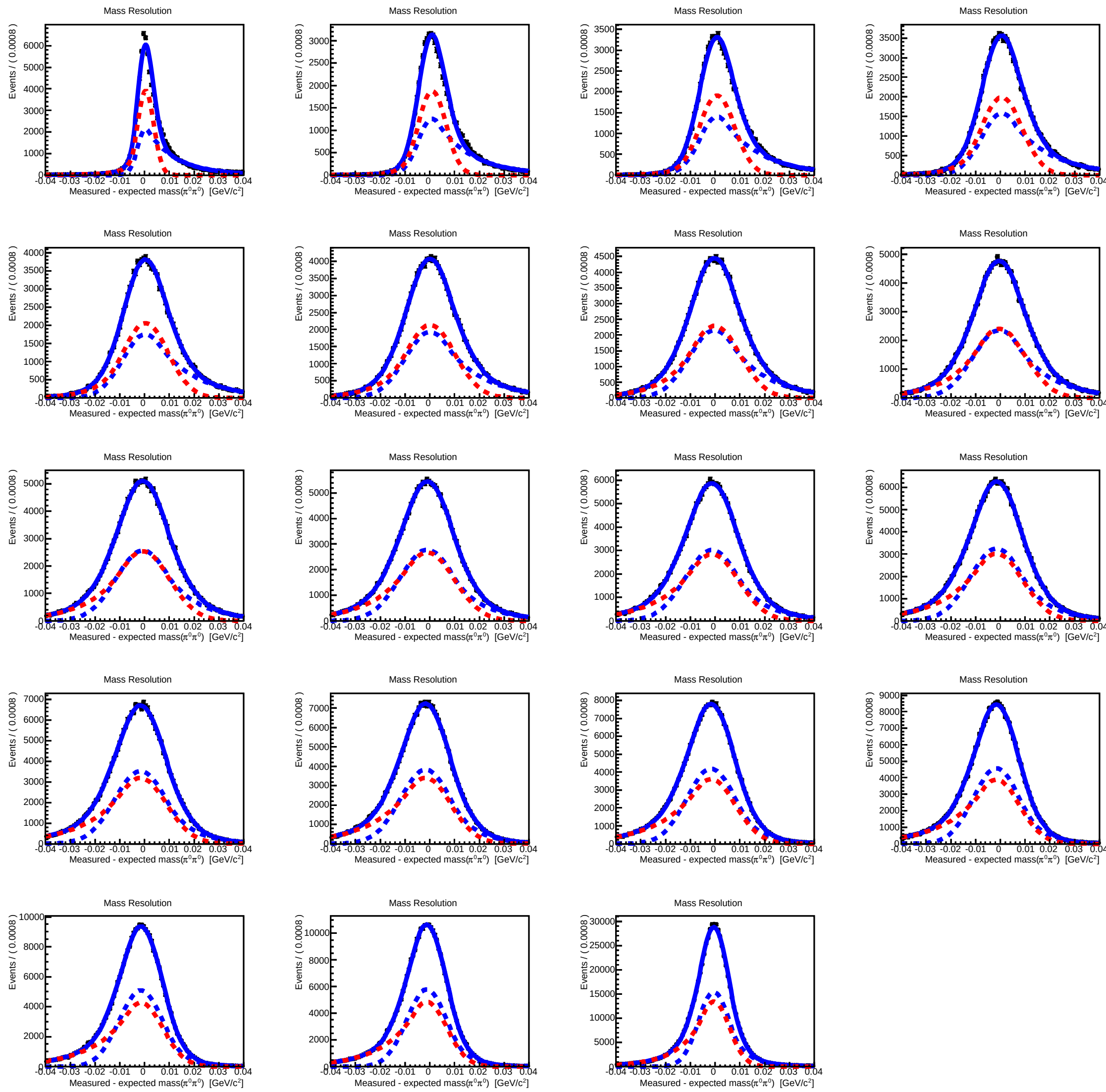

Figure 5.2: The dependence of the $\pi^0\pi^0$ mass resolution on the energy of the radiative photon is probed by fitting a Crystal Ball shape to the invariant mass of each π^0 pair in bins of photon energy. The resolution is less than 15 MeV/c^2, the size of each bin in the mass independent analysis, in each bin.

Chapter 6

Results

The results of this analysis may be separated into three distinct pieces. First, the branching ratio of radiative J/ψ decays to $\pi^0\pi^0$ is presented along with a discussion of the systematic uncertainties for this measurement. Second, the results of the mass independent amplitude analysis are presented. The mass independent approach allows for the extraction of model independent information about the scattering amplitude. These results enable one to fit the amplitude using any arbitrary model, allowing for a systematic study of model dependencies. Finally, the mass dependent analysis is presented. Measured quantities include masses, widths, and fractional intensities for each resonance included in the fit. Alternative fits using a sigma pole parameterization are also included as well as systematic checks for other significant resonances.

6.1 Branching Ratio

The results of the amplitude analysis are useful in the determination of the branching ratio of radiative J/ψ decays to $\pi^0\pi^0$, which is determined according to:

$$\mathcal{B}(J/\psi \to \gamma\pi^0\pi^0) = \frac{\epsilon_\gamma N_{\gamma\pi^0\pi^0} - N_{bkg}}{N_{J/\psi}}. \tag{6.1}$$

Here $N_{\gamma\pi^0\pi^0}$ is the number of acceptance corrected signal events determined from the amplitude analysis, N_{bkg} is the remaining background contamination according to the inclusive and exclusive MC samples, ϵ_γ is an efficiency correction, and $N_{J/\psi}$ is the number of J/ψ decays in the data. The efficiency correction is necessary to extrapolate the $\pi^0\pi^0$ spectrum down to a radiative photon energy of zero. This is accomplished by determining the fraction of phase space that is removed by applying the typical selection requirements on the energy of the radiative photon. This extrapolation increases the total number of events by 0.06%. Therefore, ϵ_γ is taken to be 1.0006. The global value for the number of radiative J/ψ decays to $\pi^0\pi^0$, $N_{\gamma\pi^0\pi^0}$, is 1,543,050 events.

The remaining backgrounds are of four types. Decays of the J/ψ to $\gamma\eta(')$ are studied with an exclusive MC sample generated according to the PDG branching ratio. The remaining misreconstructed backgrounds are determined from an exclusive MC sample that resembles the data. The other remaining backgrounds are determined from the inclusive MC sample. Finally, any events remaining in the continuum data sample taken at 3.08 GeV are also taken as a background. Each of these background is scaled appropriately. The continuum backgrounds are scaled by luminosity and a correction factor for the difference in cross section as a function of center of mass energy. In total, the acceptance corrected number of background events, N_{bkg}, is determined to be 40,412. This gives a branching ratio of $(1.147 \pm 0.002) \times 10^{-3}$, where the error is statistical only.

6.1.1 Branching Ratio Systematic Uncertainties

Sources of systematic uncertainties on the calculation of the branching ratio include contamination of the data sample by background events, the photon detection efficiency systematic uncertainty, and the uncertainty in the number of J/ψ decays. Additionally, sources of systematic uncertainty on the number of acceptance corrected signal events include how the $\omega\pi^0$ background is addressed in the fit, possible mismodeling in the kinematic fit, differences with the yield of analysis with a model of the dynamical function that describes the $\pi\pi$ interaction, and the effect of the remaining miscombined backgrounds. The uncertainty on the branching ratio of π^0 to $\gamma\gamma$ according to the PDG is 0.03%, which is negligible in relation to the other sources of error [1]. The systematic uncertainties are described below and summarized in Table 6.1.

Photon Detection Efficiency

The primary source of systematic uncertainty comes from the reconstruction of photons. To account for this uncertainty, the photon detection efficiency of the BESIII detector is studied using a sample of $J/\psi \to \pi^+\pi^-\pi^0$ events, where the π^0 decays into two photons. One of these final state photons is reconstructed, along with the two charged tracks, while the other photon is left as a missing particle in the event. This information can then be used to determine the region in the detector where the missing photon is expected. The photon detection efficiency is calculated by taking the ratio of the number of missing photons that are detected in this region to the number that are expected. The numbers of detected and expected photons are determined with fits to the two photon invariant mass distributions.

The systematic error due to photon reconstruction is determined by investigating the differences between the photon detection efficiencies of the inclusive MC sample and that of the data sample. This difference is measured to be less than 0.5%. For the five photon final state the overall uncertainty due to this effect is 2.5%.

Background Size

According to the inclusive MC sample, the total amount of background events that contaminate the signal is about 1.7%. These do not include the misreconstructed backgrounds, which are addressed in a separate systematic uncertainty. Additionally, continuum MC studies yield a contamination of approximately 0.8%. A conservative systematic error of 2.5% is added to the branching ratio measurement due to background contamination.

Number of J/ψ

The number of J/ψ decays is determined from an analysis of inclusive hadronic events

$$N_{J/\psi} = \frac{N_{sel} - N_{bg}}{\epsilon_{trig} \times \epsilon_{data}^{\psi(2S)} \times f_{cor}}, \tag{6.2}$$

where N_{sel} represents the number of inclusive events remaining after selection criteria have been applied and N_{bg} is the number of background events estimated with a data sample collected at 3.08 GeV. The efficiencies for the trigger is given by ϵ_{trig}, while $\epsilon_{data}^{\psi(2S)}$ is the efficiency for $\psi(2S)$ decays to $\pi^+\pi^- J/\psi$. Finally, f_{cor} represents a correction factor to translate $\epsilon_{data}^{\psi(2S)}$ to the efficiency for J/ψ events. To obtain N_{sel}, at least two charged tracks are required for each event. Additionally, the momenta of these tracks and the visible energy of each event are restricted in order to eliminate bhabha and di-muon events as well as beam gas interactions and virtual photon-photon collisions. The total number of J/ψ decays in the data sample according to Eq. 6.2 is determined to be (1.3106 ± 7.2) $\times 10^9$ events. The uncertainty on this number is 0.5% [83].

Uncertainty in the acceptance corrected signal yield

The nominal results restrict the backgrounds due to J/ψ decays to $\omega\pi^0$ ($\omega \to \gamma\pi^0$) by cutting on the invariant mass of each $\gamma\pi^0$ combination. An alternate method to account for this background is to include an amplitude for this decay in the analysis. The difference between the branching ratio using the signal yield for the alternate method compared to the nominal method is about 0.8%.

Differences in the results of a kinematic fit between the data and MC sample may cause a systematic difference in the acceptance corrected signal yield. This effect was investigated by varying the selection criterion requiring each event with a $\pi^0\pi^0$ invariant mass above 0.99 GeV/c^2 to have a χ^2 from the 6C kinematic fit to be less than 60. This restriction was instead relaxed to be less than 125. The difference in the branching ratio for the results of the analysis with the loosened χ^2 cut relative to that of the nominal results is about 0.2%.

Another source of systematic uncertainty in the branching ratio is the difference between applying a model that describes the $\pi\pi$ interaction or now. To test this effect, a model dependent fit using interfering Breit-Wigner line shapes was performed. The difference in the branching ratio using the acceptance corrected yield of this analysis compared to the nominal results is about 0.5%.

The effect of the remaining misreconstructed backgrounds on the results is studied by performing the mass independent amplitude analysis on an exclusive MC sample. This MC sample was generated according to the results of a model dependent analysis of the data and includes the proper angular distributions. After applying the same selection criteria that are applied to the data, the MC sample is passed through the mass independent analysis. This process is repeated after removing the remaining misreconstructed backgrounds from the sample. The difference in the branching ratio between these two methods is 0.01%. The effect of these backgrounds is therefore taken to be negligible.

6.1.2 Branching Ratio Results

Using the world's largest data sample of its type, the branching ratio of radiative J/ψ decays to $\pi^0\pi^0$ is measured to be $(1.147 \pm 0.002 \pm 0.042) \times 10^{-3}$, where the first error is statistical and the second is systematic. This is the first measurement of the

Source	$J/\psi \to \gamma\pi^0\pi^0$ (%)
Photon detection efficiency	2.5
Number of J/ψ	0.5
Background size	2.5
$\omega\pi^0$ background	0.8
Kinematic fit χ^2_{6C}	0.2
Model dependence	0.5
Total	3.7

Table 6.1: This table summarizes the systematic uncertainties (in %) for the branching ratio of $J/\psi \to \gamma\pi^0\pi^0$.

exclusive branching fraction.

6.2 Mass Independent Analysis Results

With the goal of presenting the greatest amount of information possible, the results of the mass independent amplitude analysis are presented in two ways. First, plots of the intensities of each amplitude and their relative phase differences are presented here as a function of $\pi^0\pi^0$ invariant mass. Second, a series of data sets will be made available that contain the intensities and phase differences of all amplitudes in the fit for each bin of $\pi^0\pi^0$ invariant mass. These data sets may be used to fit the amplitude using any arbitrary model. This allows for a systematic study of model dependencies such as whether or not the phases of component amplitudes of a similar type should be constrained. True to this spirit, rather than treating differences due to unavoidable assumptions as systematic errors, the results of the analysis under each assumption are presented independently. An estimate of the uncertainty due to these assumptions may be determined by fitting a model to each set of results. Differences between the results of such applications give an estimate of systematic uncertainties.

The nominal results of the mass independent analysis are obtained by allowing the relative phases of the 2^{++} amplitudes allowed to float above the KK threshold. The primary difficulty with this method is the presence of ambiguous solutions to the fits in most bins. The most significant difference between the ambiguous solutions is in the E1 component amplitudes (the 0^{++} and 2^{++} swap some amount of the intensity). This is especially apparent by looking at the fit projections in a bin with a significant difference in the fractional intensities between the two sets of solutions (Fig. 6.2 and Fig. 6.1).

For each bin in the nominal results, the predicted ambiguous solutions may be calculated using the prescription described in the Appendix A. These predicted ambiguous solutions agree well with the experimentally determined solutions. For some bins, the ambiguous solution is identical to the solution from which it was calculated. That is, several bins do not exhibit ambiguities. Below the KK threshold, the nominal results utilize the background subtracted data set, in which the $\gamma\eta(')$ backgrounds have been removed from these results as discussed in section 4.4.2.

Two sets of alternate results are presented in addition to the nominal results. Alternate results 1 contain the results of fits in which the phases of the three components of the 2^{++} amplitude are constrained to be the same even above the KK threshold. The region below the KK threshold utilizes the background subtracted data and is therefore equivalent to the nominal results in that region. In contrast, alternate results 2 have the phase constraint relaxed above KK threshold as in the nominal results, but do not have the $\gamma\eta(')$ backgrounds subtracted. Thus, the results above the KK threshold are equivalent to the nominal results, but the results below the threshold are independent results with a different assumption about the backgrounds.

Several bins in the mass independent analysis contain more than one set of solutions that are not ambiguous partners. In other words, some bins have extra solutions (beyond the ambiguous pair) which have similar values of -2 $\ln L$. These are interpreted as local minima in the likelihood function. Any extra solutions can be eliminated by applying simple assumptions like the continuity of the intensities and phase differences as a function of $\pi^0\pi^0$ invariant mass.

The continuity of the intensities and phase differences is determined quantitatively by calculating a χ^2 value as follows. For each bin, the function values (intensities or phase differences) in the neighboring two bins are averaged to give $\bar{x} = (x_{i+1} - x_{i-1})/2$ (for each function x). The difference between the function value in the bin of interest and this average value is used to give the χ^2 for this particular solution,

$$\chi^2 = \left(\frac{\bar{x} - x_i}{\sigma_i}\right)^2, \tag{6.3}$$

where σ_i is the error on the function value in the bin of interest. If a neighboring bin contains multiple solutions, this process is repeated for each of the three function values. The solution in each bin with the minimum χ^2 value is taken as the nominal result. This process is carried out by starting from bins that do not have multiple solutions and iterating through the entire mass spectrum.

6.2.1 Mass Independent Fit Projections

It is useful to plot the angular projections of the fit results in each bin. The angles of interest for this channel are the polar and azimuthal angles for the radiative photon in the J/ψ rest frame and those for one of the π^0s in the $\pi^0\pi^0$ center of mass frame. In each bin, the predicted distributions for each of the amplitudes may be plotted according to the results of the fit in that bin.

The lab frame is defined with the z-axis in the direction of the positron beam. There is a small crossing angle between the electron and positron beams. The cross product between the beams defines the y-axis in the lab frame. The photon angular distributions are calculated in the J/ψ rest frame, which is created by a boost from the lab frame to that in which the J/ψ is at rest.

The π^0 angular distributions are calculated in the rest frame of the $\pi^0\pi^0$ pair. The z-axis is given by the direction opposite the direction of propagation of the radiative photon. This means that the z-axis is the direction of flight of the $\pi^0\pi^0$ pair (the direction along which the boost to this rest frame has been performed) in the J/ψ rest frame. The y-axis is defined by the cross product of the z-axis with the positron beam direction.

The fit projections are useful for studying the differences between the ambiguous solutions. That is, the angular distributions for a given bin calculated from the sum of all amplitudes are the same for each of the ambiguous solutions, but individual amplitudes may have different distributions. By studying the fit projections in a bin that contains multiple solutions, it is evident that the E1 component amplitudes of the 0^{++} and 2^{++} waves tend to have the most significant change (Figure 6.1,6.2).

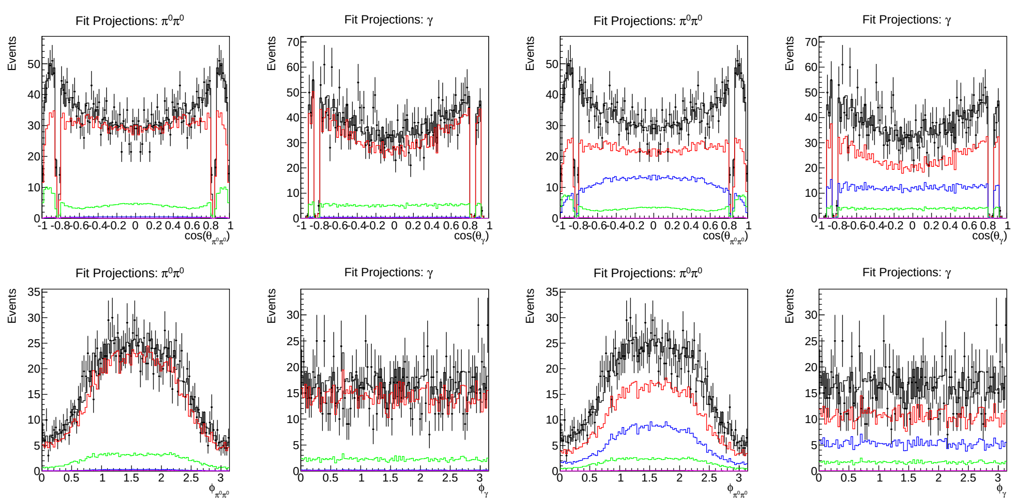

Figure 6.1: The angular distributions for the two ambiguous solutions in the $\pi^0\pi^0$ mass bin around 2.0 GeV are plotted here. The left four plots show the angular distributions for one of the ambiguous solutions and the right four show the same distributions for its partner. These plots include detector acceptance effects.

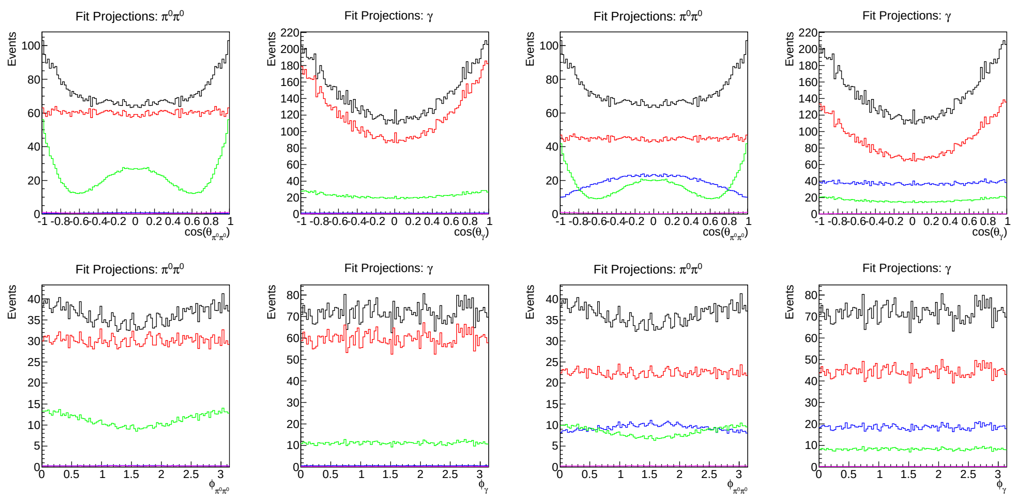

Figure 6.2: The angular distributions for the two ambiguous solutions in the $\pi^0\pi^0$ mass bin around 2.0 GeV are plotted here. The left four plots show the angular distributions for one of the ambiguous solutions and the right four show the same distributions for its partner. Here the acceptance effects have been removed.

6.2.2 Nominal Results

Again, the nominal results of the mass independent analysis are obtained by allowing the relative phases of the 2^{++} amplitudes allowed to float above the KK threshold. The nominal intensity for each amplitude as a function of $\pi^0\pi^0$ invariant mass is plotted in Figure 6.3. Each of the phase differences between two amplitudes is plotted in Fig. 6.4. Above the KK threshold, two distinct sets of solutions are apparent. The bins below about 0.6 GeV contain multiple non-ambiguous solutions, only one set of which preserves continuity as defined above. Several other bins, both above and below the KK threshold, exhibit similar behavior.

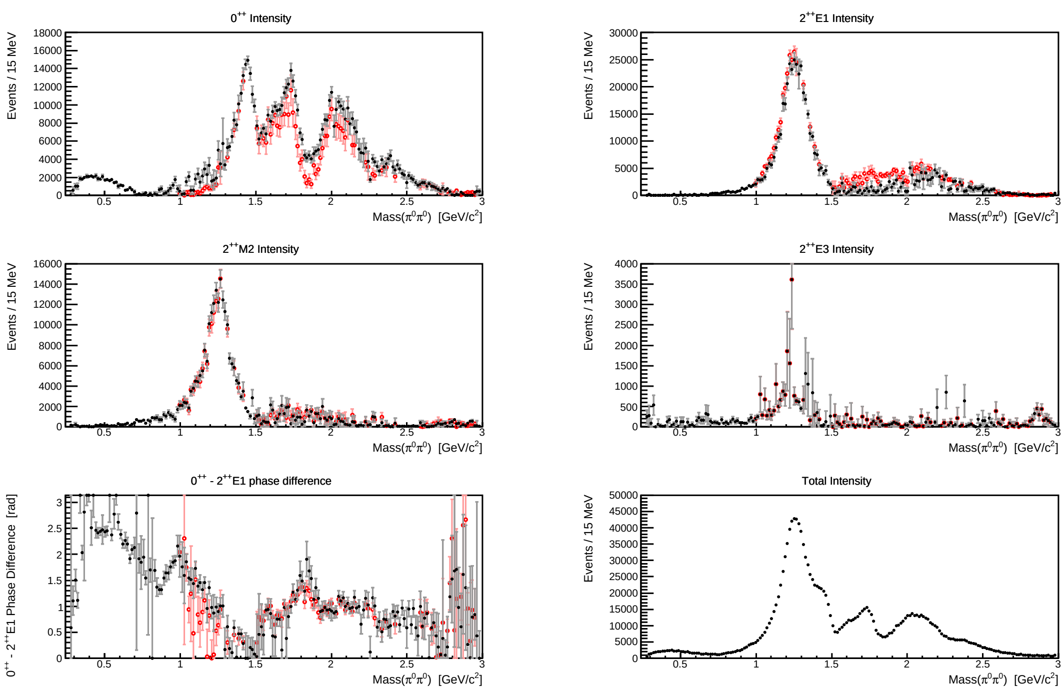

Figure 6.3: The intensity for each amplitude is plotted here as a function of $\pi^0\pi^0$ invariant mass for the nominal results. The solid black markers show the intensity calculated from one set of solutions, while the open red markers represent its ambiguous partner.

As discussed in Appendix A, the mathematical ambiguities may be predicted from the experimental results. Figures 6.5 and 6.6 show the experimentally determined

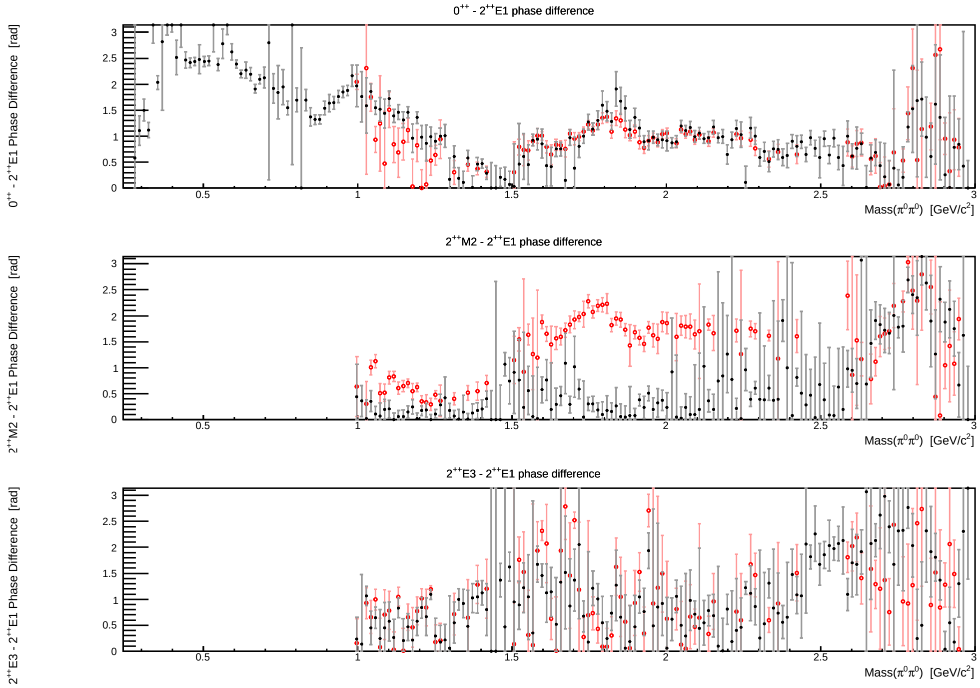

Figure 6.4: The phase differences are plotted here as a function of $\pi^0\pi^0$ invariant mass for the nominal results. The solid black markers show the phase differences calculated from one set of solutions, while the open red markers represent its ambiguous partner.

and mathematically predicted solutions. It is apparent that the predictions match the intensities calculated from the fitting procedure.

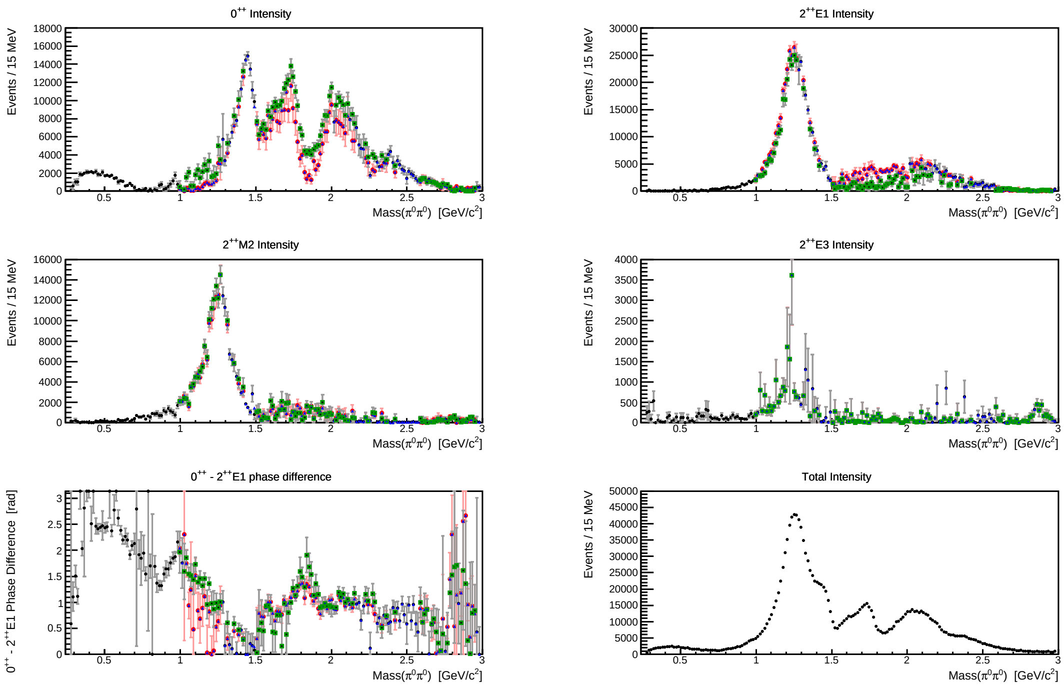

Figure 6.5: The intensity for each amplitude is plotted here as a function of $\pi^0\pi^0$ invariant mass. The solid black markers show the intensity calculated from one set of solutions, while the open red markers represent its ambiguous partner. The solid blue triangles show the predicted intensity for the ambiguous partner to the solutions represented by the solid black markers. The open green squares similarly predict the ambiguous partner to the open red circle solutions.

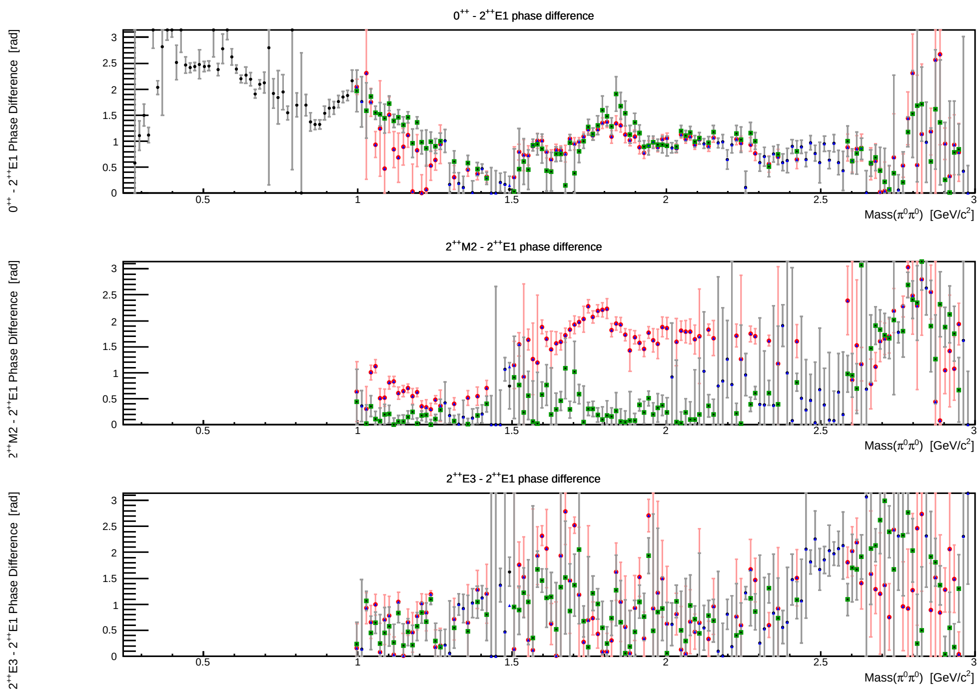

Figure 6.6: The phase differences are plotted here as a function of $\pi^0\pi^0$ invariant mass. The solid black markers show the intensity calculated from one set of solutions, while the open red markers represent its ambiguous partner. The solid blue triangles show the predicted intensity for the ambiguous partner to the solutions represented by the solid black markers. The open green squares similarly predict the ambiguous partner to the open red circle solutions.

6.2.3 Permutations

For the nominal results, it is apparent that the ambiguous sets of solutions are distinct in some regions, while they approach and possibly cross at other points. The most powerful discriminator of this effect is the phase difference between the E1 and M2 components of the 2^{++} amplitude (the middle plot of Fig. 6.4). In particular, one set of solutions appears to be consistent with no phase difference between the components of the 2^{++} amplitudes for most of the invariant mass spectrum (the black markers), while the other is significantly different for the regions between about 1.0 GeV and 1.3 GeV as well as between about 1.5 GeV and 2.4 GeV. In the regions just below 1.5 GeV and above 2.4 GeV, the two solutions are consistent with each other. Due to this possible crossing of solutions, each distinct permutation of the possible sets of solutions is presented. Three crossing regions are defined near 0.99 GeV (the KK threshold), 1.3 GeV, and above 2.4 GeV. This leads to four distinct permutations of the nominal results. They are shown in Figs 6.7-6.10.

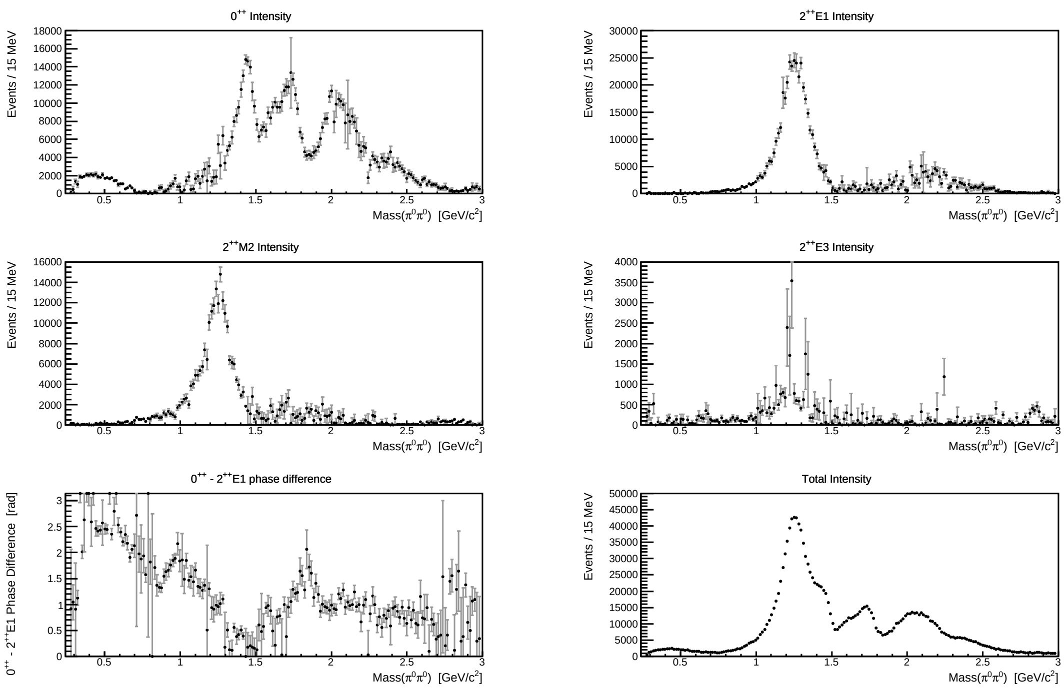

Figure 6.7: The intensity for each amplitude in the first permutation of the nominal results is plotted here. These results are extracted from the background subtracted data sample.

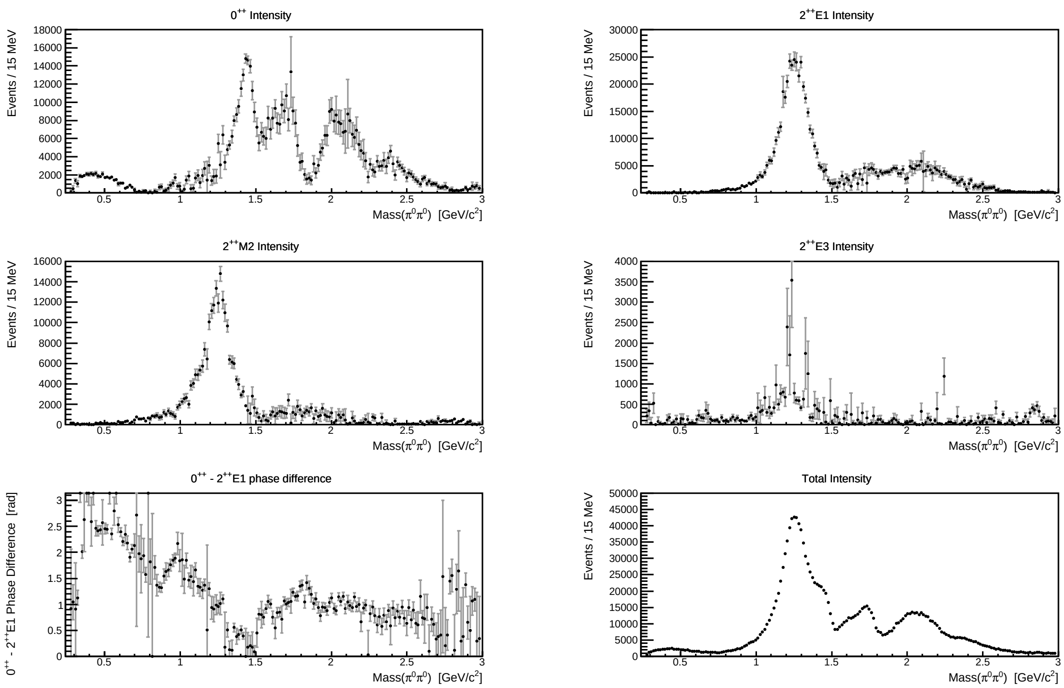

Figure 6.8: The intensity for each amplitude in the second permutation of the nominal results is plotted here. These results are extracted from the background subtracted data sample.

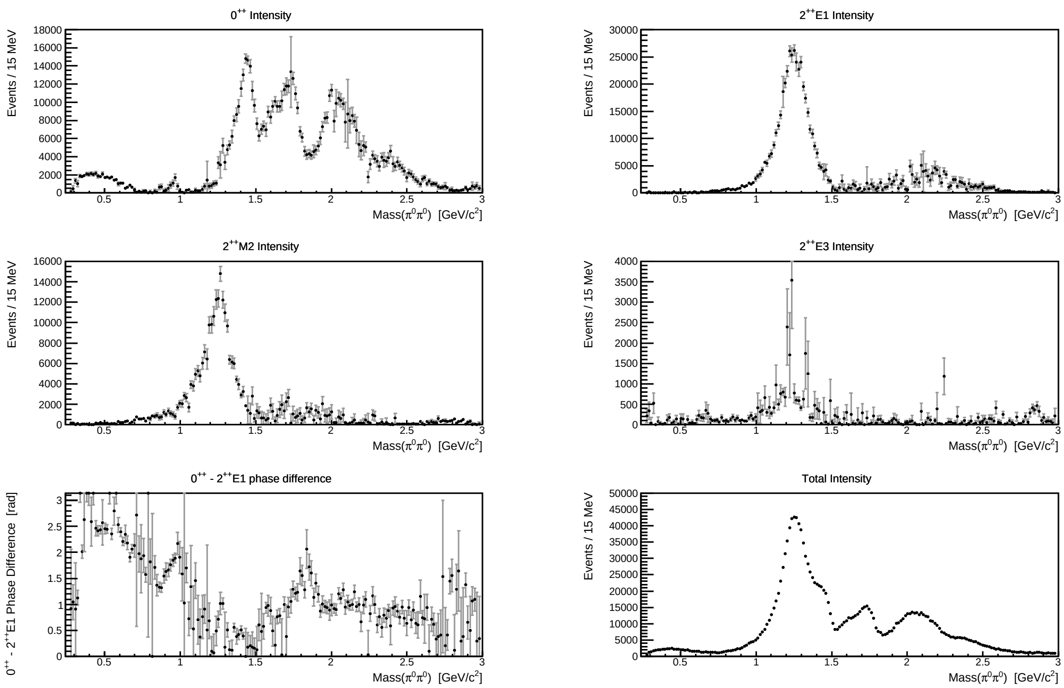

Figure 6.9: The intensity for each amplitude in the third permutation of the nominal results is plotted here. These results are extracted from the background subtracted data sample.

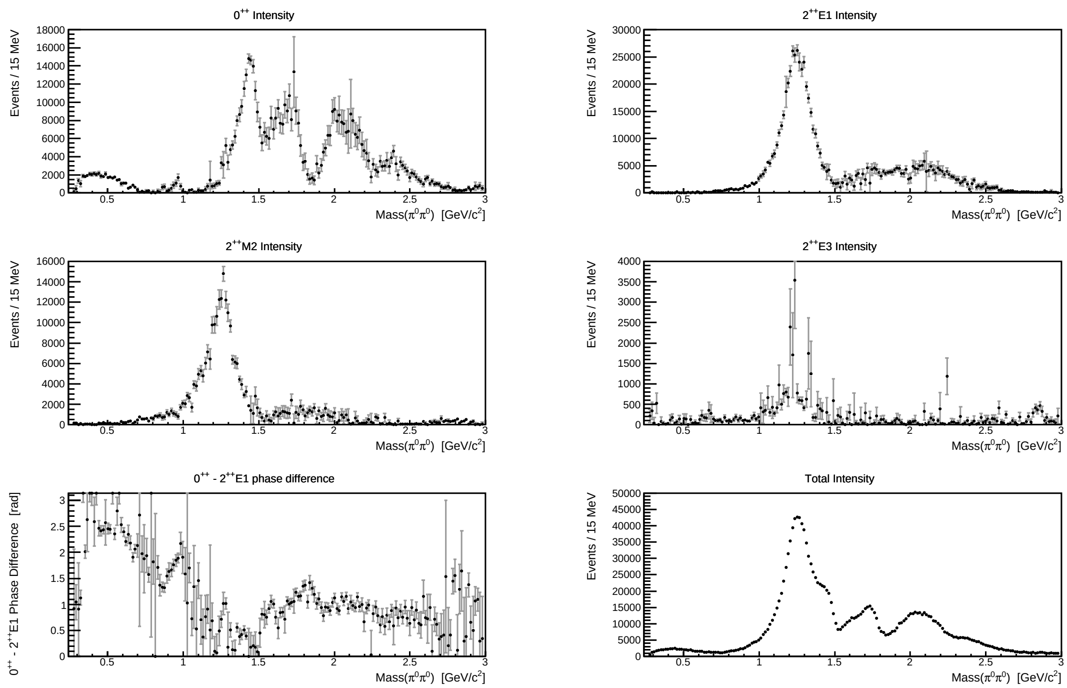

Figure 6.10: The intensity for each amplitude in the fourth permutation of the nominal results is plotted here. These results are extracted from the background subtracted data sample.

6.2.4 Alternate Results 1

The mass independent analysis is also repeated after constraining the components of the 2^{++} amplitude to have the same phase above the KK threshold. These results are presented in Fig. 6.11. The region below the KK threshold is redundant with the nominal results above, containing data with the $\gamma\eta(')$ background subtraction.

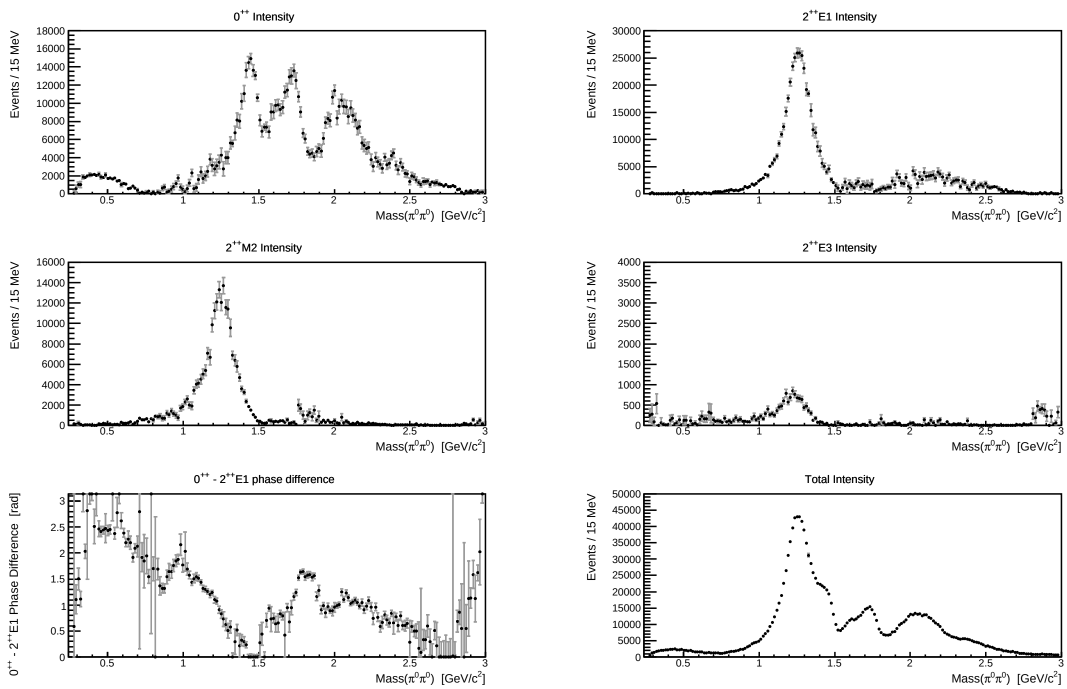

Figure 6.11: The intensity for each amplitude in alternate results 1 is plotted here as a function of $\pi^0\pi^0$ invariant mass. The ambiguous solutions are no longer present due to the constraint that the phases of each component of the 2^{++} amplitude must be equal.

The 0^{++} and 2^{++} spectra in alternate results 1 appear very similar to one set of solutions for the nominal results. This is a predicable outcome given that one set of solutions in the nominal results has phase differences between each pair of 2^{++} amplitudes that are consistent with zero. Alternate results 1 are determined by applying the constraint that these phase differences are exactly zero. For comparison, the two sets of results are overlaid in Fig. 6.12. The pull distributions, calculated by dividing the difference between the nominal and alternate results by the error on the nominal results, is shown in Fig. 6.13.

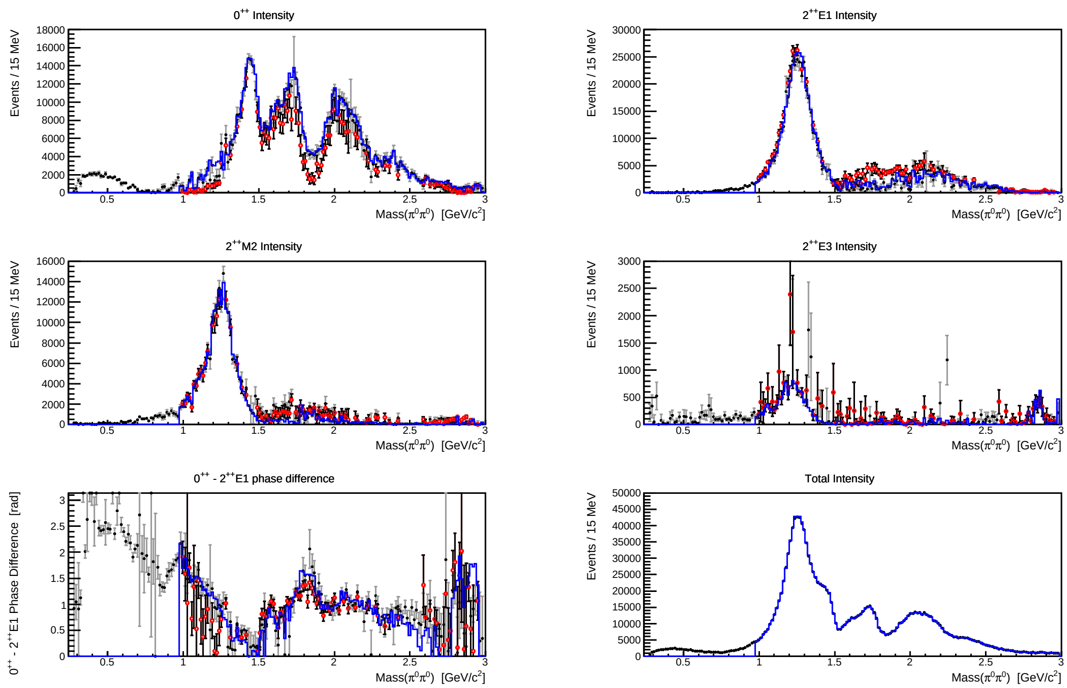

Figure 6.12: For comparison, a blue histogram representing alternate results 1 is overlaid on the nominal results. The alternate results appear consistent with one set of solutions for the nominal results (that with phase differences between the 2^{++} waves consistent with zero). The two sets of results are redundant in the low mass region.

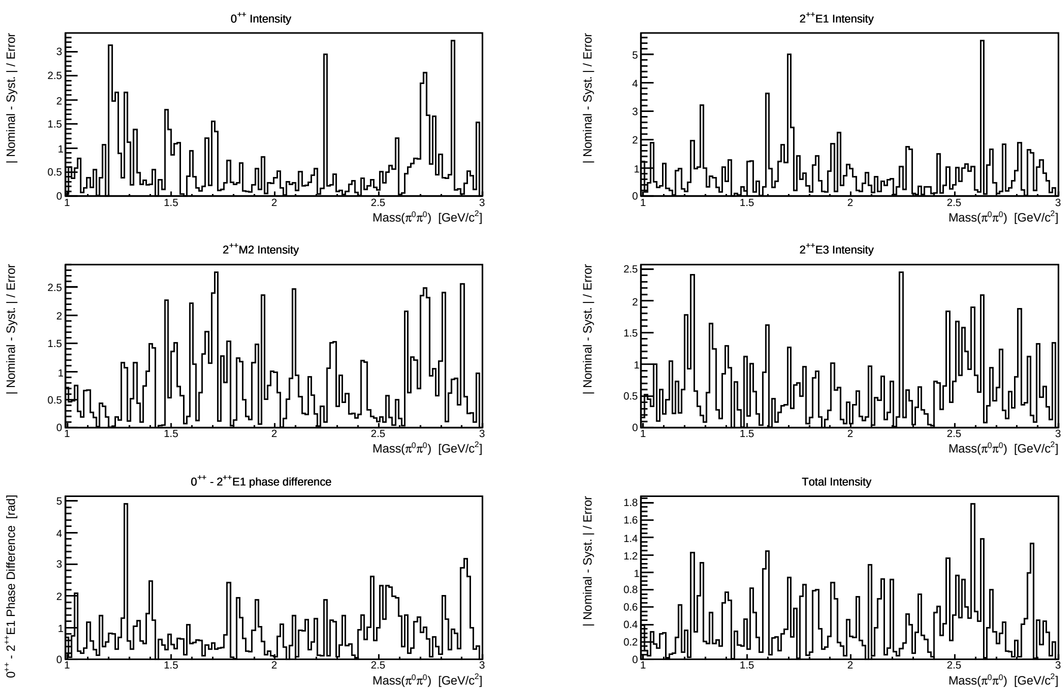

Figure 6.13: The pull distribution (defined in the text) of one set of solutions from the nominal results versus alternate results 1.

6.2.5 Alternate Results 2

Finally, the mass independent analysis is also repeated with the pure data, which does not contain the $\gamma\eta(')$ background subtraction (Fig. 6.14). For clarity, this process is briefly repeated here. An exclusive MC sample of J/ψ decays to $\gamma\eta(')$ are generated according to the branching fractions given by the PDG [1] and with angular distributions according to a model within BESEVTGEN called the JPE model. This sample must then pass all of the selection criteria discussed in section 4.4. The events that remain are added to the maximum likelihood fit with a negative weight (-1). In this way, when the exclusive MC sample is included in the analysis, it has the effect of canceling out the effect of the remaining $\gamma\eta(')$ backgrounds in the data sample.

Since the backgrounds of this type are only significant below the KK threshold, the results above 0.99 GeV are redundant with the nominal results above. Both the 0^{++} and 2^{++} spectra are equivalent to those of the nominal results for much of the invariant mass spectrum. The primary difference is a slight enhancement in the 0^{++} intensity in the region below about 0.6 GeV and near the η' peak (Fig. 6.15). This is interpreted as being due to the contribution of events decaying through $\gamma\eta(')$ that are being treated as signal events.

6.2.6 Discussion

The results of the mass independent analysis exhibit significant in the 0^{++} amplitude just below 1.5 GeV/c^2 and near 1.7 GeV/c^2. If these structures are interpreted as the $f_0(1500)$ and $f_0(1710)$ respectively, the presence of these states in radiative J/ψ decays is quite conclusive. This would also lend credence to a prediction for each of these states to have a significant glueball component. The apparent strength of the $f_0(1710)$ coupling to $\pi\pi$ over the KK final state seems to contradict the corresponding ratio to these final states in J/ψ decays to $\omega\pi\pi$ and ωKK [20]. Interestingly, there is no visual evidence for a structure around 1.3 GeV/c^2, which would correspond to

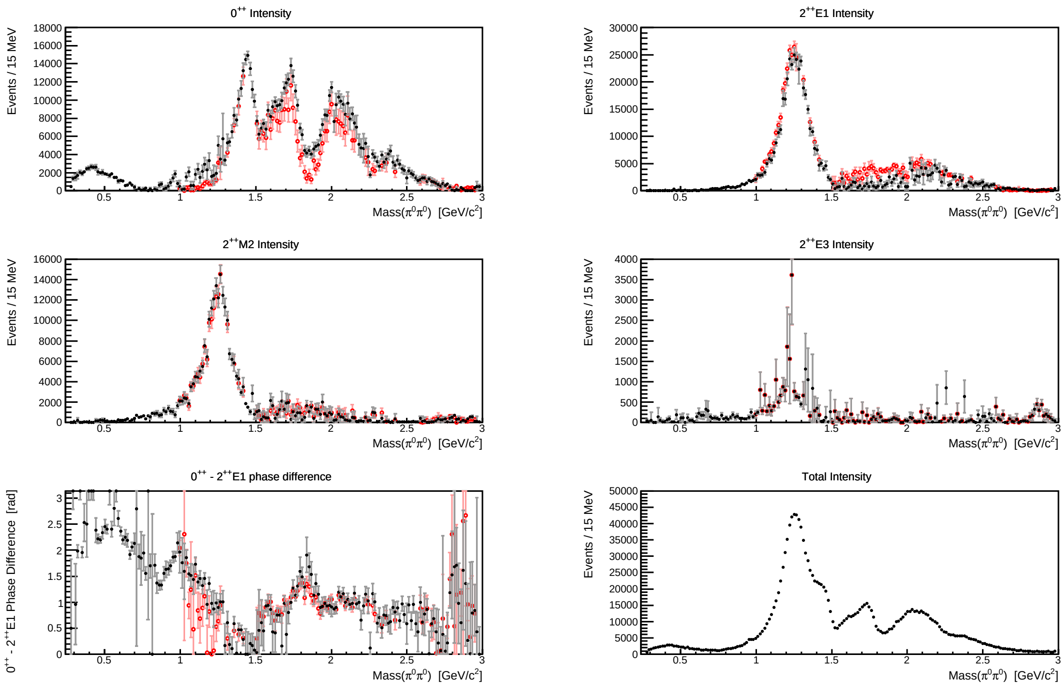

Figure 6.14: The intensity for each amplitude in alternate results 2 is plotted here as a function of $\pi^0\pi^0$ invariant mass. In these results, the $\gamma\eta(')$ backgrounds have not been subtracted from the data.

the $f_0(1370)$. A definitive statement on the necessity of the $f_0(1370)$ to describe the data will require a coupled channel analysis to determine the number and placement of pole positions.

Additional structures are present below 0.6 GeV/c^2 and near 2.0 GeV/c^2. It seems reasonable to interpret the former as the σ ($f_0(500)$), while the latter may be attributed to the $f_0(2020)$. The presence of the four states below 2.1 GeV/c^2 would be consistent with the previous study of radiative J/ψ decays to $\pi\pi$ by BESII [18]. Due to the fact that this study constrained the phases of the 2^{++} amplitudes to have the same phase, a comparison with alternate results 1 rather than the nominal results is most appropriate. The results of this analysis also suggest that 0^{++} spectrum may also exhibit a structure just below 1 GeV/c^2, which was not observed in Ref. [18], but the enhancement in this region is quite small. Finally, there also appears to be

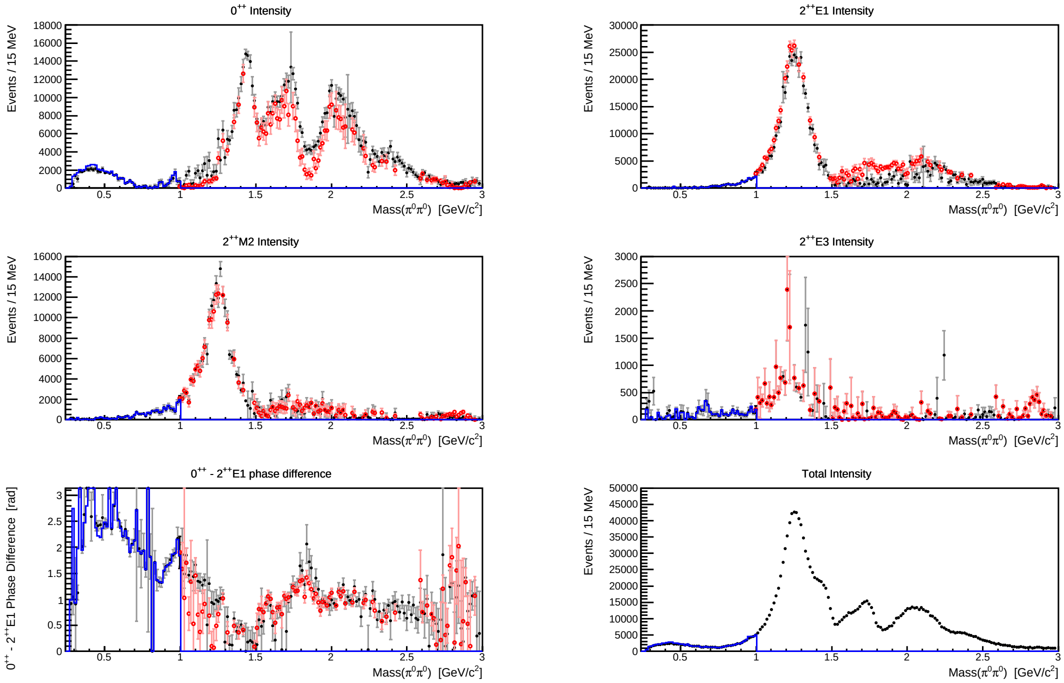

Figure 6.15: For comparison, alternate results 2 are overlaid in blue on the nominal results. The two results differ only in the low mass region.

some structure around 2.4 GeV/c^2 in the 0^{++} spectrum.

In the 2^{++} amplitude, the results of this analysis indicate a strong contribution from what appears to be the $f_2(1270)$ consistent with previous results [18]. However, the remaining structure in the 2^{++} amplitude appears significantly different than the BESII results. In particular, Ref. [18] describes the region between 1.5 and 2.0 GeV/c^2 with a relatively narrow $f_2(1810)$. One permutation of the nominal results in this region indicates that the structures in this region are much wider, while the other permutation suggests that there is very little contribution from states in this region.

For both permutations of the nominal results, there appears to be a broad structure above 2 GeV/c^2. The previous results on this reaction include an $f_2(2150)$ and an $f_4(2050)$ in this region [18]. The tensor spectrum near 2 GeV/c^2 is of interest in the search for a tensor glueball. Lattice calculations suggest that a tensor glueball in

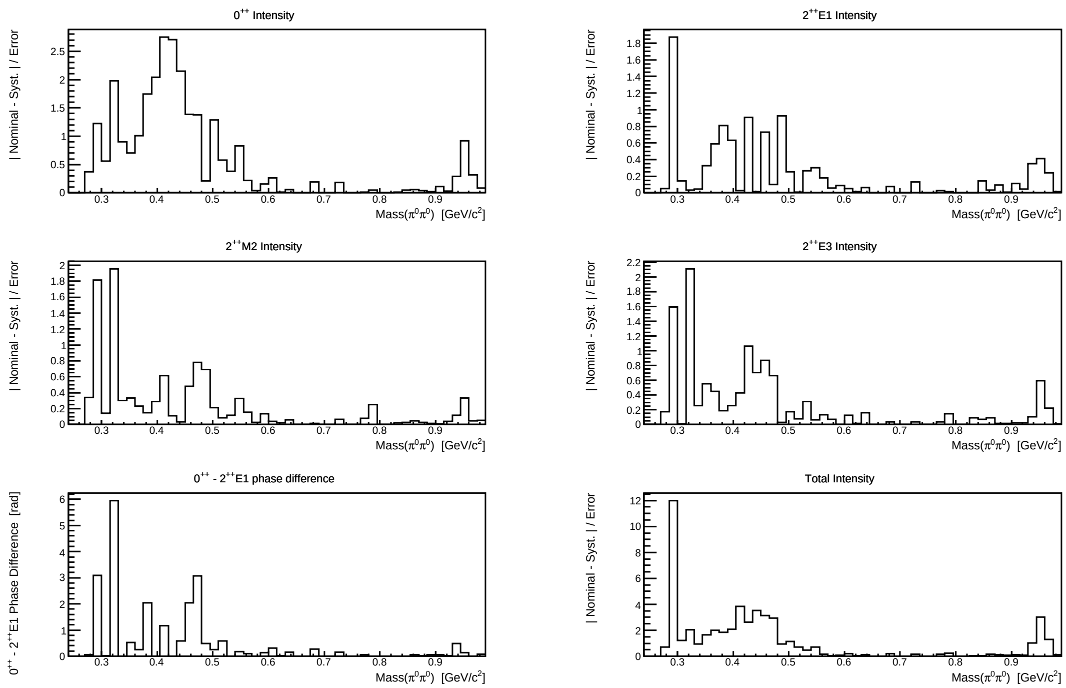

Figure 6.16: The pull distribution (defined in the text) of one set of solutions from the nominal results versus alternate results 2. The results differ only in the low mass region.

this region should have a mass of about 2.40 ± 0.15 GeV/c^2 [16]. However, studies of the $\phi\phi\eta$ final state in $\pi^- p$ production and the $\pi^+\pi^-$ system in $p\bar{p}$ annihilation indicate that all tensor states may be associated with conventional quark states except for a broad structure near 2.01 GeV/c^2 [84, 85]. This latter state may be interpreted as a tensor glueball state [86]. The structure above 2 GeV/c^2 in the nominal results of this analysis appear consistent with such a state.

6.2.7 Error analysis

A common issue for analyses of this type is the consistency of error bars. Some bins that are near each other in invariant mass may have results with wildly different error bars. This may be due in part to some of the assumptions that go into the determination of the errors. Minimization is accomplished by using the MIGRAD algorithm of MINUIT, while the HESSE method is used to calculate the error matrix. HESSE calculates the second derivative matrix after minimization and inverts it to get there error matrix. In this way, the error matrix accounts for parameter correlations, but not non-linearities. That is, it only measures the second derivative matrix at a single point and does not measure the likelihood contour elsewhere. HESSE also relies on the assumption of Gaussian errors, which may not be correct, in the determination of the error matrix. The MINOS processor calculates the parameter errors taking into account any non-linearities by actually determining the likelihood function away from the minimum, but at the cost of losing the error matrix, which is needed to account for parameter correlations.

Investigations into the error bars in the mass independent analysis have not provided any conclusive evidence that there is a problem with how the error bars are calculated. First of all, some bins do not exhibit multiple solutions. This is likely due to the inability of MINUIT to discern two minima in the likelihood contour. These errors may understandably be larger than their neighbors. For bins that do exhibit multiple solutions, contour plots of the likelihood function as a function of the 0^{++} parameters may be compared. The contours in bins with small and large error bars are plotted in Fig. 6.17 and Fig. 6.18 respectively. Of course, these plots are something of a simplification due to the fact that the true contour exists in seven dimensional space. Due to the presence of multiple solutions in a bin, discontinuities are produced in these plots if other parameters are allowed to float. It is not apparent that the error bars are inconsistent with the likelihood contours.

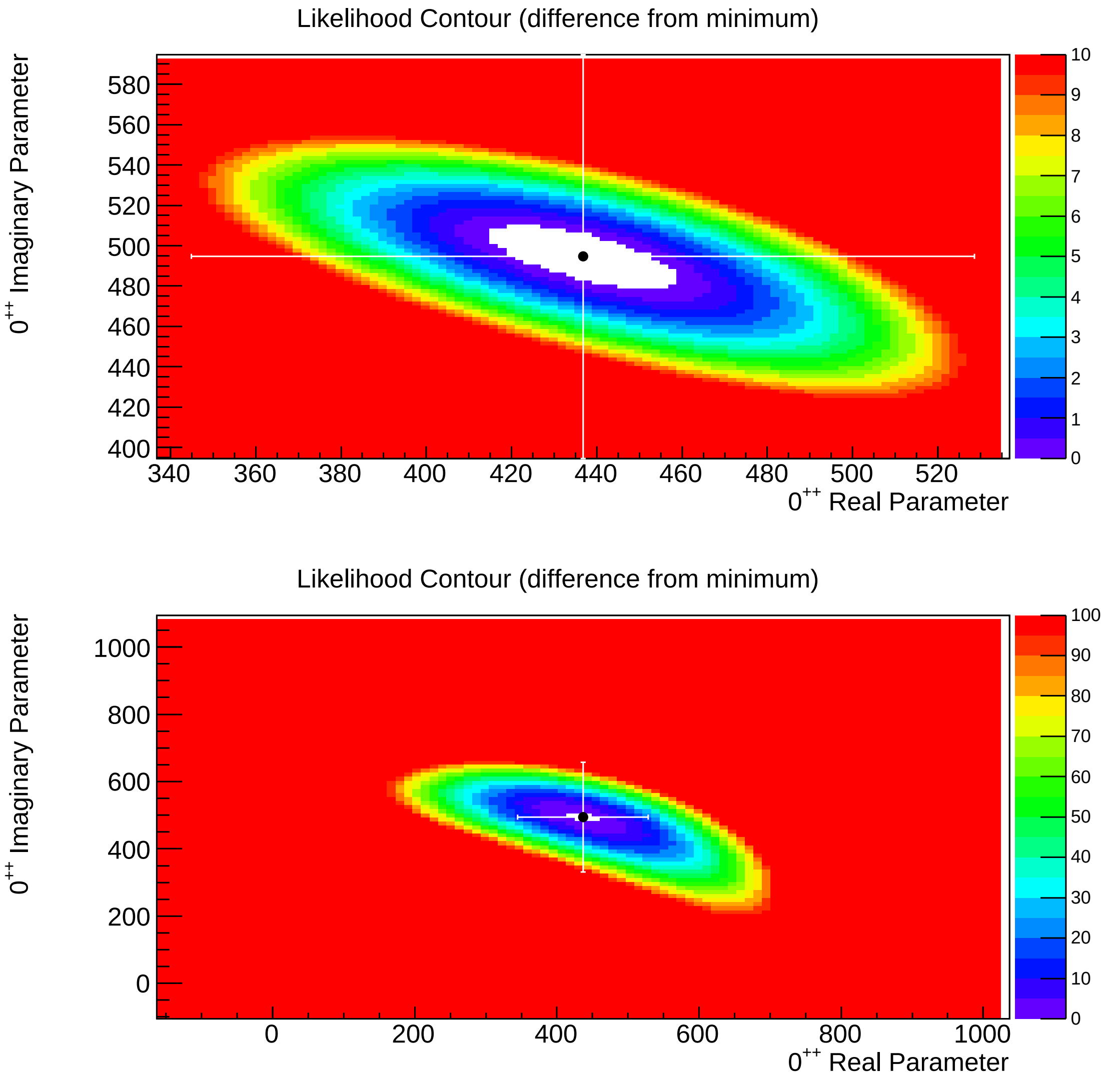

Figure 6.17: These plots show the likelihood distribution for the 0^{++} parameters near the minimum (shown by the maker and error bars). The errors in this bin are small relative to its neighbor. All other parameters are held at their minimum values according to the solution in each bin. The top plot shows likelihood values up to 10 units larger than the minimum, while the bottom plot shows up to 100 units difference.

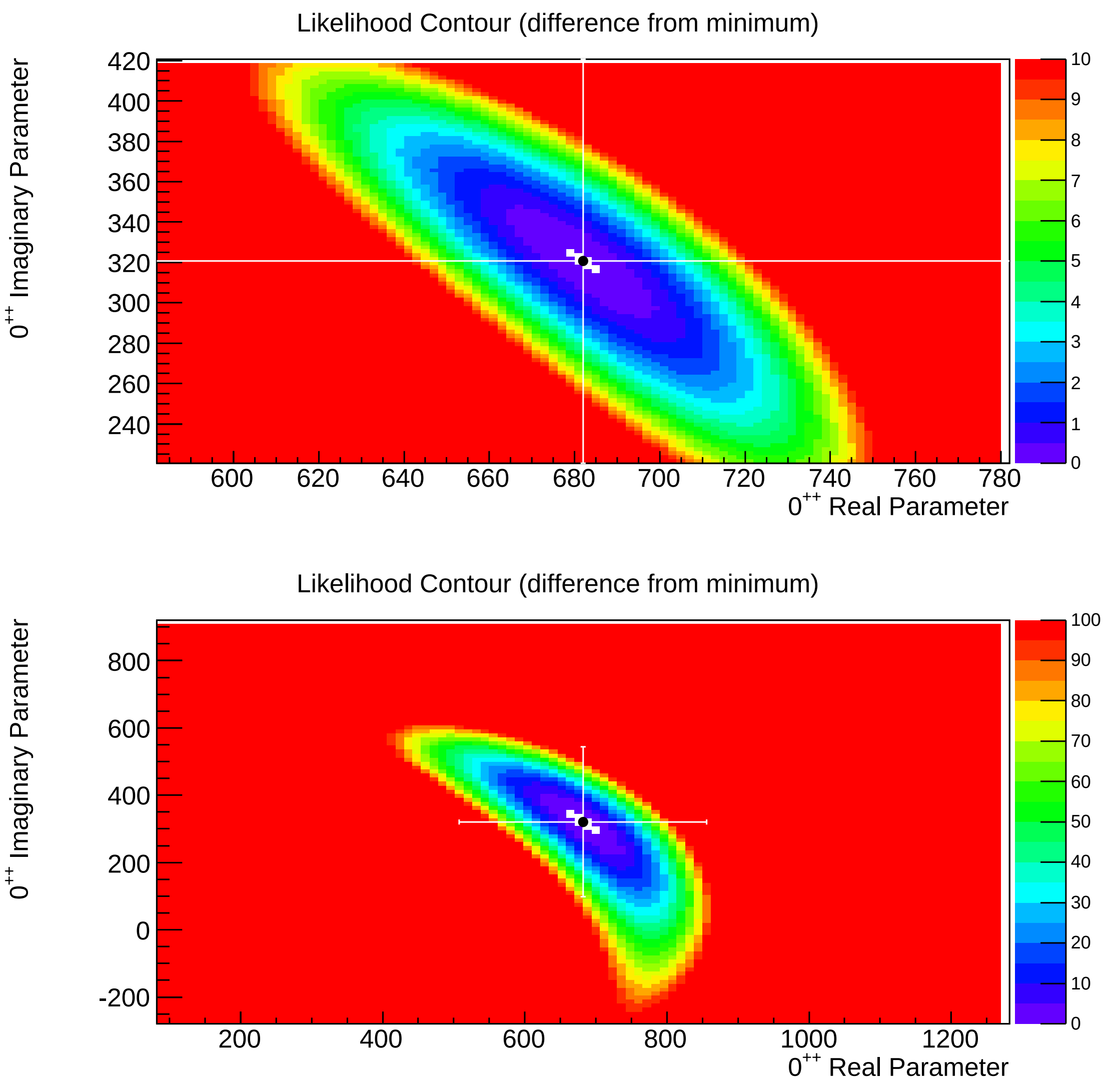

Figure 6.18: These plots show the likelihood distribution for the 0^{++} parameters near the minimum (shown by the maker and error bars). The errors in this bin are large relative to its neighbor. All other parameters are held at their minimum values according to the solution in each bin. The top plot shows likelihood values up to 10 units larger than the minimum, while the bottom plot shows up to 100 units difference.

6.3 Mass Dependent Analysis Results

The mass dependent fits are carried out in a series of steps. Based on the results of the mass independent analysis and previous studies of this channel, a preliminary set of resonances is selected. The mass and width of each of these amplitudes is allowed to float individually, along with the complex couplings, in a series of fits. This process is repeated iteratively until the mass and width parameters are stable for subsequent fits. For parameters that do not converge, the PDG value is used in the fit. Instability in the resonance parameters occurs only for the tensor states in the high mass region, where the 2^{++} wave is least significant. Once a satisfactory set of parameters is determined, a simple fit is performed with the masses and widths of each resonance are fixed to the nominal values. The best fit is that with the minimum value of -2 $\ln L$.

The results of the mass dependent fit are plotted in Fig. 6.19. As expected, the 2^{++} amplitude is dominated by an $f_2(1270)$, with some additional contributions by several additional resonances including the $f_2'(1525)$, the $f_2(1950)$ and the $f_2(2150)$. The 0^{++} amplitude is composed of several resonances, each of which contribute a significant amount to the intensity. These resonances include the $f_0(500)$ (the σ), $f_0(1500)$, $f_0(1710)$, $f_0(2020)$, and $f_0(2330)$. There is also some evidence of an $f_0(980)$, which is discussed below. The masses, widths, etc. for each resonance in the fit are given in Table 6.2).

The mass independent results provide complementary information on the structure of the amplitudes in the mass dependent fit. Thus it is useful to overlay the two types of solutions to gauge the consistency between the two types of analysis methods. Figure 6.20 shows this comparison for each wave and the phase difference between the 0^{++} and 2^{++} E1 amplitudes. One area of concern is the comparison in the 0^{++} amplitude and the phase difference, wherein the two analysis types diverge fairly strongly (Fig. 6.21). This may suggest the need for an $f_0(980)$.

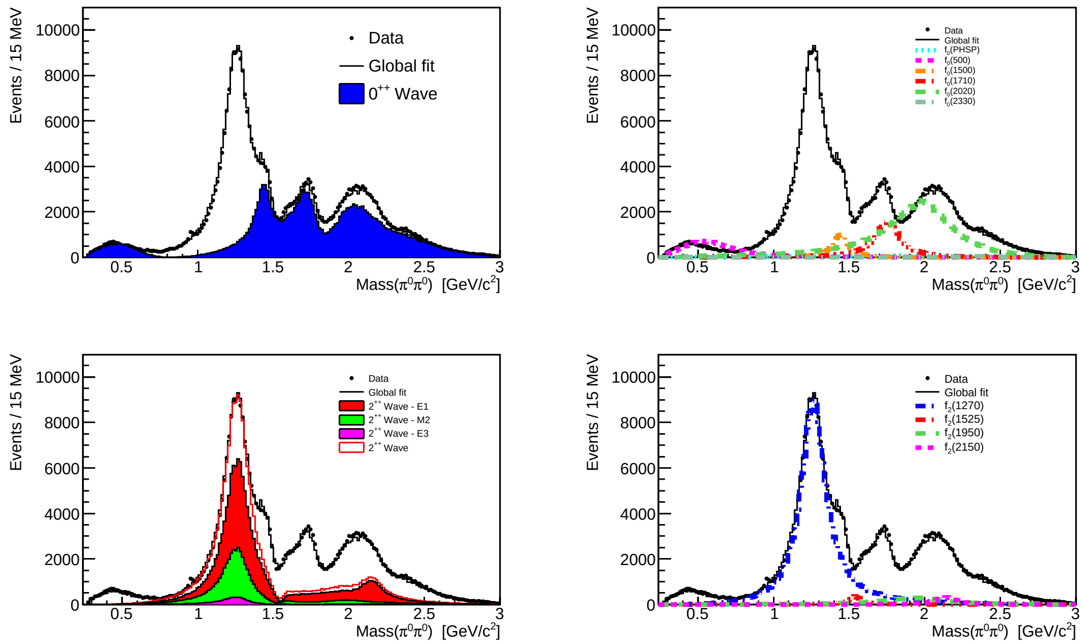

Figure 6.19: The results of a mass dependent fit of the $\gamma\pi^0\pi^0$ couplings is plotted here as a function of $\pi^0\pi^0$ invariant mass. The left two plots show the contributions of each total amplitude (0^{++}, 2^{++}E1, etc.), while the right two plots show the contribution of each resonance to these amplitudes. The black markers show the intensity of the data, while the black, empty histogram shows the total intensity from the fit. The resonances and their BW parameters are given in Tab. 6.2.

To quantify the comparison between the mass dependent and mass independent results, a χ^2 is calculated according to the following procedure. The results of the mass dependent fit is used to determine the value of each (complex) coupling at the center of each bin of $\pi^0\pi^0$ invariant mass. This may then be compared with the mass independent fit results for each bin. The vector, Δ, is the difference between the amplitudes in the mass independent analysis and the mass dependent analysis. The error matrix, Err, is the inverse of the correlation matrix from the mass independent results. Then,

$$\chi^2 = \Delta^T Err \Delta \tag{6.4}$$

Amplitude	Mass	Width	Efficiency	Fit Fraction
$f_0(PHSP)$	–	–	0.233	2.0 ± 0.1
$f_0(500)$	0.508 ± 0.004	0.442 ± 0.009	0.216	6.5 ± 0.1
$f_0(1500)$	1.443 ± 0.001	0.118 ± 0.003	0.222	3.4 ± 0.1
$f_0(1710)$	1.752 ± 0.001	0.189 ± 0.004	0.237	7.9 ± 0.2
$f_0(2020)$	1.980 ± 0.003	0.481 ± 0.008	0.242	27.4 ± 0.6
$f_0(2330)$	2.342 ± 0.004	0.313 ± 0.041	0.250	0.30 ± 0.04
$f_2(1270)$	1.264 ± 0.001	0.196 ± 0.001	0.231	46.9 ± 0.3
$f_2(1565)$	1.540 ± 0.002	0.096 ± 0.004	0.252	0.9 ± 0.1
$f_2(1950)$	1.943 ± 0.016	0.283 (fixed)	0.241	3.1 ± 0.1
$f_2(2150)$	2.143 ± 0.014	0.272 (fixed)	0.301	1.0 ± 0.1

Table 6.2: The characteristics of the resonances from the mass dependent fit are described here. These parameters represent the best fit results which do not include the $f_0(980)$.

may be calculated for each bin. Here Gaussian errors have been assumed. The sum of this quantity over each bin is then a measure of the similarity of the two results. A comparison between one set of solutions from the nominal results and the mass dependent results given in Fig. 6.19 gives a χ^2 of 104,071 and a χ^2/DOF of 99.2.

The significance of each resonance in the fit is tested by removing each resonance individually and comparing the best value of -2 $\ln L$ with and without the resonance. The results of these tests are shown in Tab. 6.3. The middle set of values are for the removal of each amplitude individually. Several additional resonances are also checked by adding it to the fit and comparing the likelihood values as above. These additional resonances include the $f_0(980)$, the $f_4(2050)$ and the $f_4(2300)$, each with masses and widths given by the PDG. The results are shown in the bottom group of values in Tab. 6.3. The $f_0(980)$ does appear to be significant, especially considering the comparison of the fits above.

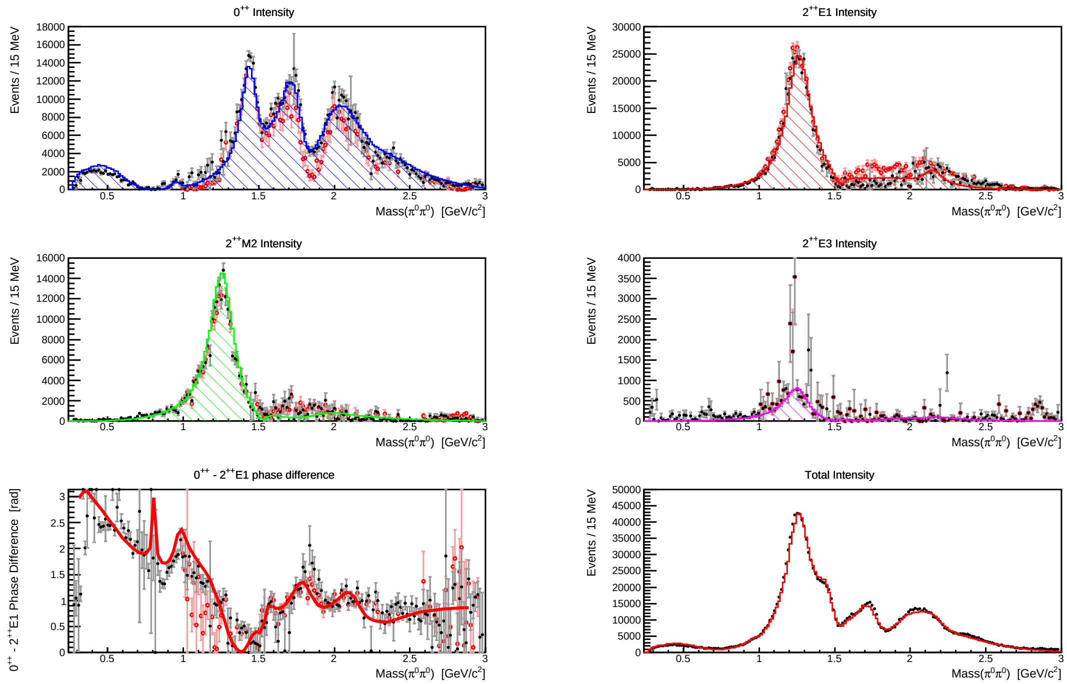

Figure 6.20: The nominal mass independent results are overlaid here with the results of the mass dependent fit. The colored histograms show the mass dependent solutions for each amplitude, while the markers show the mass independent results.

Resonance	-2 ln L	Difference
Best Fit	-8955117.576	—
$f_0(500)$	-8941288.419	-13829.157
$f_0(1500)$	-8950719.865	-4397.711
$f_0(1710)$	-8945770.755	-9346.821
$f_0(2020)$	-8949484.995	-5632.581
$f_0(2330)$	-8954554.941	-562.635
$f_2(1270)$	-8871079.36	-84038.216
$f_2(1525)$	-8954058.95	-1058.626
$f_2(1950)$	-8952719.432	-2398.144
$f_2(2150)$	-8953386.604	-1730.972
$f_0(980)$	-8955925.882	808.306
$f_4(2050)$	-8955351.222	233.646
$f_4(2300)$	-8955155.611	38.035

Table 6.3: The significances of the resonances in the mass dependent fit are shown here by comparing the values of -2 ln L with and without each resonance individually.

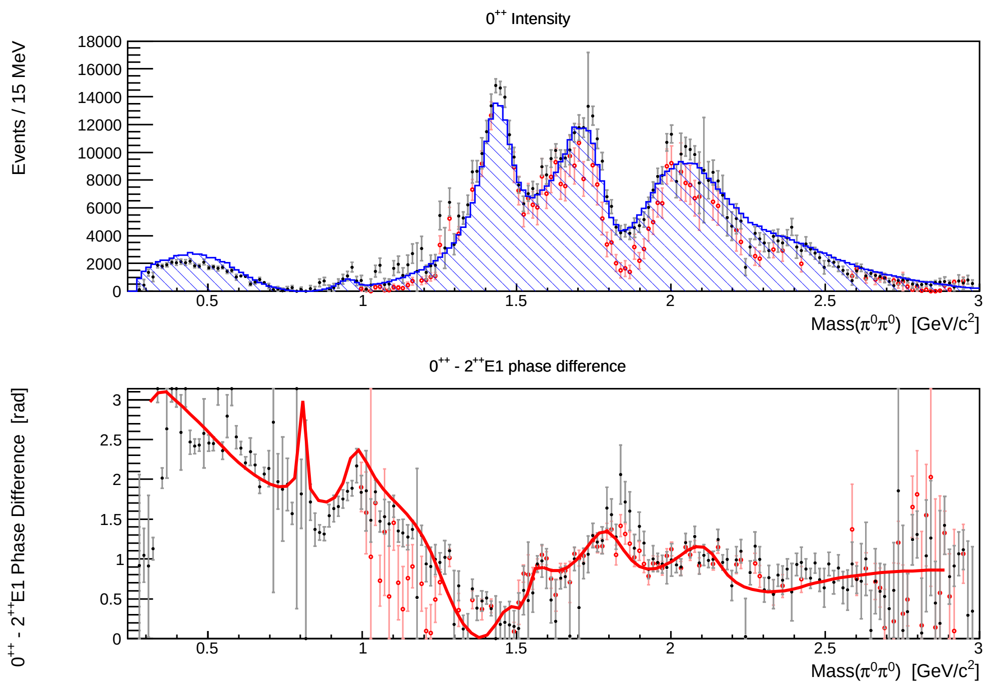

Figure 6.21: The nominal mass independent results are overlaid here with the results of a mass dependent fit. The colored histograms show the mass dependent solutions for each amplitude, while the markers show the mass independent results.

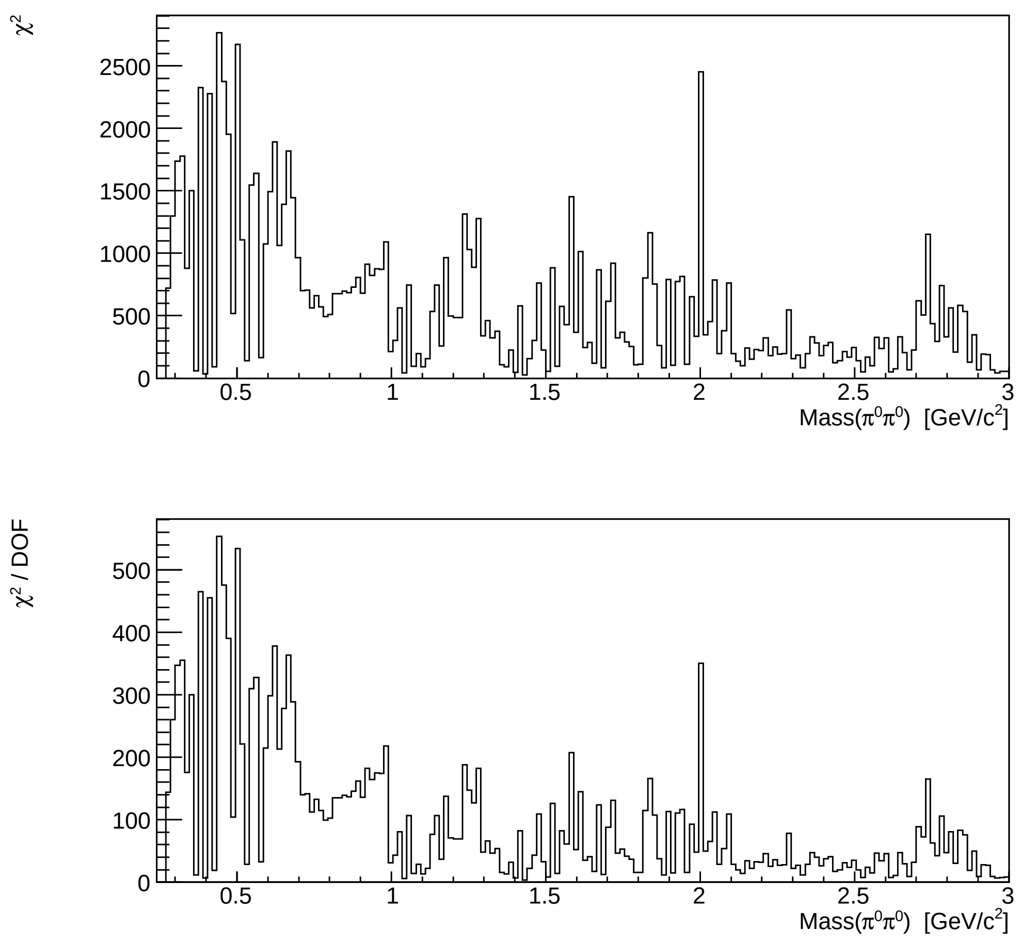

Figure 6.22: The χ^2 per bin for the nominal mass independent results and the mass dependent fit.

6.3.1 Adding an $f_0(980)$

After studying the significances above, the mass dependent fits were repeated with the inclusion of the $f_0(980)$. The mass and width of the $f_0(980)$ were allowed to float individually as in the procedure discussed above. The results are shown in Fig. 6.23 and Tab. 6.4. Comparisons with the mass independent results are shown in Fig. 6.24 and Fig. 6.25. It appears as though the $f_0(980)$ is necessary for the results of the mass dependent fit to give a phase difference between the 0^{++} and 2^{++} amplitudes which is consistent with that from the mass independent results. The χ^2 for the comparison given in Fig. 6.24 is 97,868 with a χ^2/DOF of 93.3, slightly better than the results without the $f_0(980)$.

Amplitude	Mass	Width	Efficiency	Fit Fraction (%)	Significance
$f_0(PHSP)$	–	–	0.295	3.13 ± 0.01	
$f_0(500)$	0.520 ± 0.003	0.497 ± 0.013	0.226	6.45 ± 0.01	1,588
$f_0(980)$	0.957 ± 0.002	0.039 ± 0.004	0.227	0.13 ± 0.01	411
$f_0(1500)$	1.440 ± 0.001	0.121 ± 0.002	0.296	4.93 ± 0.01	
$f_0(1710)$	1.763 ± 0.001	0.158 ± 0.003	0.312	7.52 ± 0.01	5,859
$f_0(2020)$	1.974 ± 0.004	0.441 ± 0.007	0.315	32.51 ± 0.03	6,591
$f_0(2330)$	2.229 ± 0.009	0.223 ± 0.014	0.326	0.58 ± 0.01	584
$f_2(1270)$	1.263 ± 0.001	0.186 ± 0.001	0.309	45.88 ± 0.03	10,087
$f_2(1565)$	1.547 ± 0.002	0.078 ± 0.003	0.346	0.72 ± 0.01	1,414
$f_2(1950)$	1.940 (fixed)	0.283 (fixed)	0.319	3.89 ± 0.01	5,556
$f_2(2150)$	2.157 (fixed)	0.272 (fixed)	0.396	0.95 ± 0.01	848

Table 6.4: The characteristics of the resonances from the mass dependent fit are described here. These parameters represent the best fit results which include the $f_0(980)$.

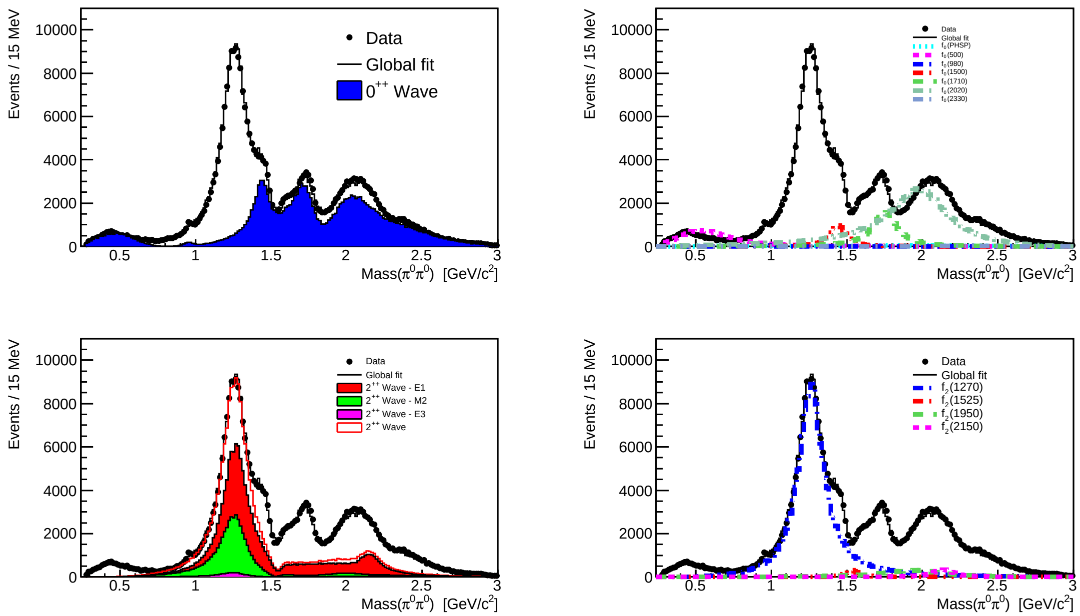

Figure 6.23: The results of a mass dependent fit including the $f_0(980)$ is plotted here as a function of $\pi^0\pi^0$ invariant mass. The left two plots show the the contributions of each total amplitude (0^{++}, 2^{++}E1, etc.), while the right two plots show the contribution of each resonance to these amplitudes. The black markers show the intensity of the data, while the black, empty histogram shows the total intensity from the fit. The resonances and their BW parameters are given in Tab. 6.4.

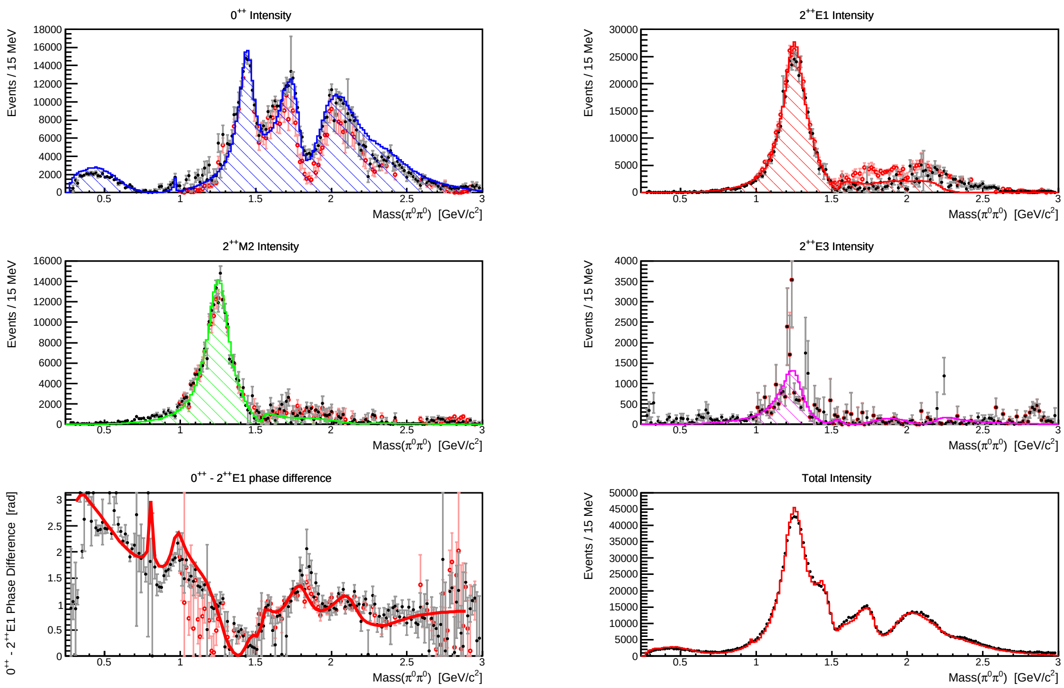

Figure 6.24: The nominal mass independent results are overlaid here with the results of a mass dependent fit with the $f_0(980)$. The colored histograms show the mass dependent solutions for each amplitude, while the markers show the mass independent results.

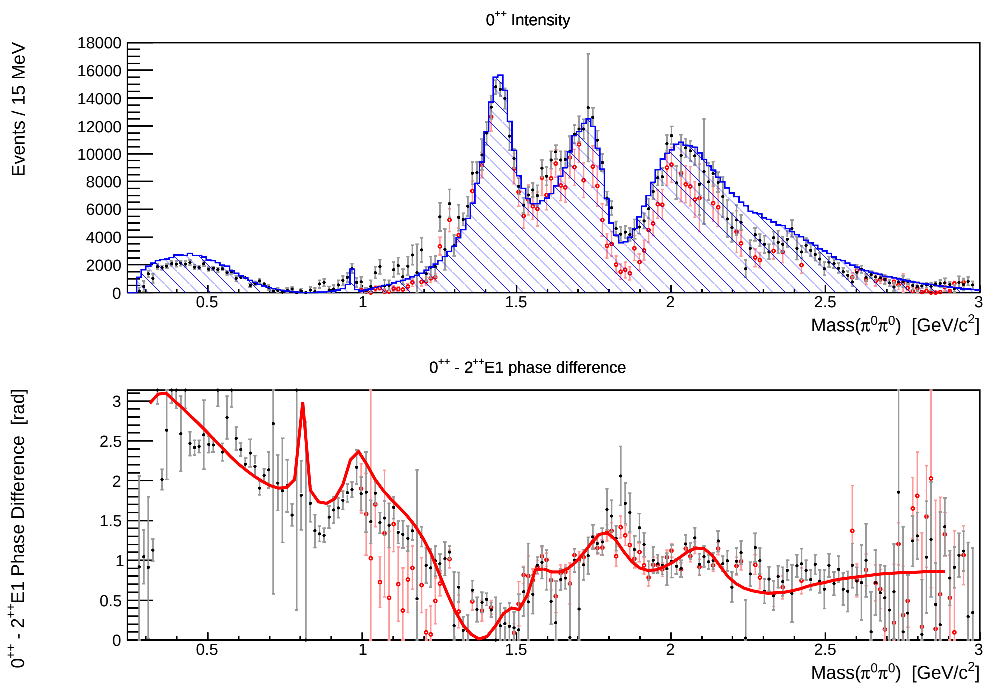

Figure 6.25: The nominal mass independent results are overlaid here with the results of a mass dependent fit with the $f_0(980)$. The colored histograms show the mass dependent solutions for each amplitude, while the markers show the mass independent results.

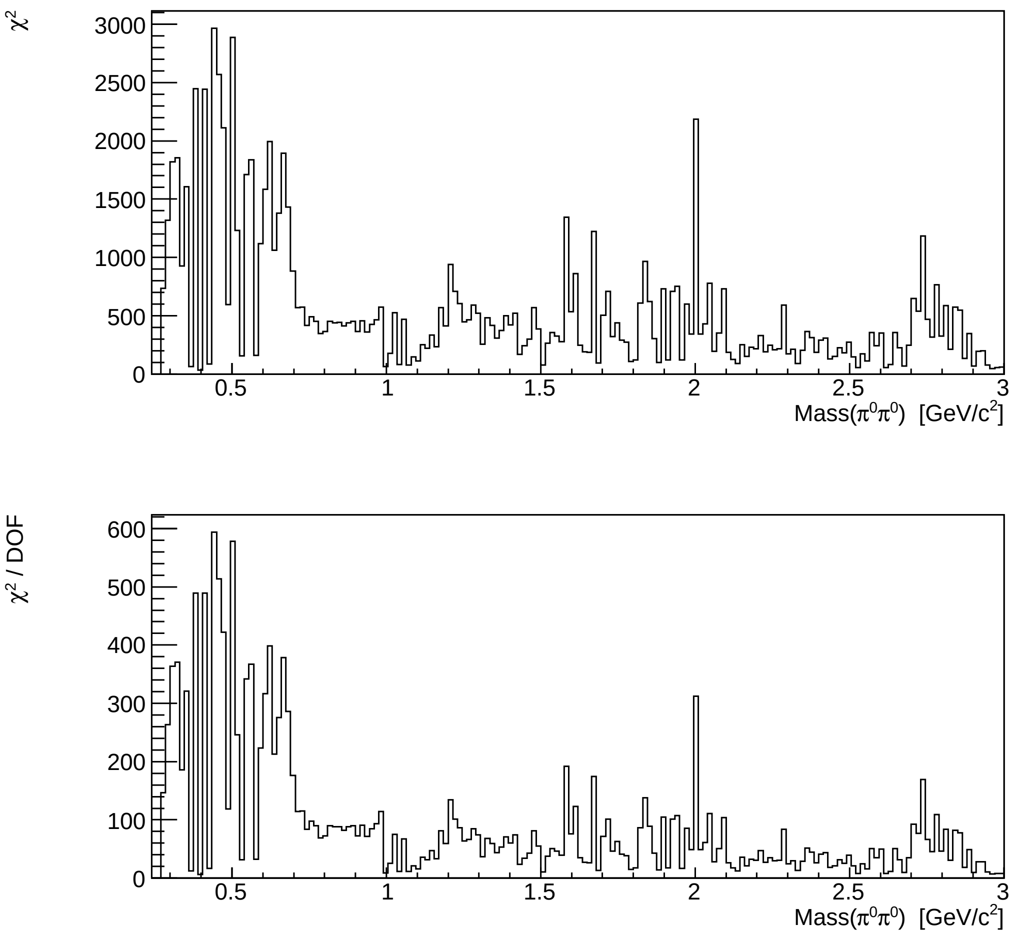

Figure 6.26: The χ^2 per bin for the nominal mass independent results and the mass dependent fit with an $f_0(980)$.

Chapter 7

Systematic Uncertainties

The systematic uncertainties for the mass independent analysis are discussed in this section. Two types of systematic uncertainties are discussed. The first type has to do with the systematic uncertainty in the overall normalization of the results. The second type of systematic uncertainty has to do with model dependencies. Rather than introduce systematic errors due to these effects, the mass independent analysis is repeated under different assumptions to allow for systematic studies of their effect on the results. This method is chosen due to the fact that the systematic uncertainties are correlated amongst all bins the in mass independent analysis. Therefore, if a subsequent analysis is to properly consider these uncertainties, the correlated shift of the nominal results is the pertinent information.

The systematic uncertainties include the assumption that phase differences between amplitudes of the same J^{PC} are allowed to float above KK threshold and the effect of assumptions about various backgrounds. Additionally, several cross checks are performed in order to study the effects of how the $\omega\pi^0$ background is addressed and to test the significance of an additional 4^{++} amplitude.

The systematic uncertainties on the branching ratio of radiative J/ψ decays to $\pi^0\pi^0$ are discussed in Sec. 6.1.1.

7.1 Normalization

Sources of systematic uncertainties to the normalization of the mass independent results include the photon detection efficiency systematic uncertainty, contamination of the data sample by background events, the uncertainty in the number of J/ψ decays, how the $\omega\pi^0$ background is addressed in the fit, possible mismodeling in the kinematic fit, and the effect of the remaining miscombined backgrounds. The uncertainty on the branching ratio of π^0 to $\gamma\gamma$ according to the PDG is 0.03%, which is negligible in relation to the other sources of error [1]. These systematic uncertainties were introduced in Sec. 6.1.1. Selected results are described below in greater detail.

7.1.1 Photon detection efficiency systematic uncertainties

The primary source of systematic uncertainty comes from the reconstruction of photons. From a study of J/ψ decays to $\pi^+\pi^-\pi^0$, which is discussed in detail in Appendix C, the uncertainty due to photon reconstruction is less than 0.5% per photon. This gives an overall uncertainty of 2.5% per event (five final state photons).

In addition to this, a study was performed to determine the uncertainty due mismodelling of the photon detection efficiency in the inclusive MC sample. The phase space MC samples in each bin of the mass independent fit were modified according to the differences in the shape of the $\cos\theta$ distribution between the inclusive MC sample and the data. This is accomplished by weighting each event of the phase space MC sample by the quantity δ, which represents the fractional difference between the efficiencies of the inclusive MC sample and the data according to $\delta = e_{data}/e_{MC}$. Here e_{MC} is the photon detection efficiency from the inclusive MC sample and e_{data} is that from the data. The value δ is determined in bins of $\cos\theta$ (Fig. 7.1). Then, each phase space MC event is weighted by δ for each photon, depending on which angular bin into which it falls. This means that each event will have a weight that is the product of five different individual weights.

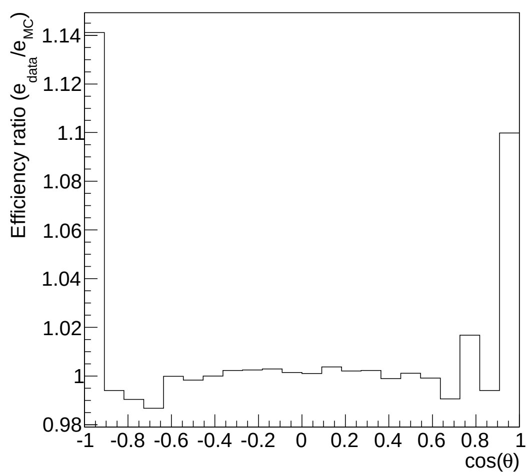

Figure 7.1: The difference between the angular distributions of the photon detection efficiency between the inclusive MC and data samples is shown here. The difference is quantified by δ, where $\delta = e_{data}/e_{MC}$.

The benefit to using this method is that the number of events in the phase space MC sample has not changed, but the effect of the difference in acceptance may be studied. This method is similar to that described in Sec. 5.1. Recall that the normalization integral is approximated using a phase space MC sampel (Eq. 5.16. In a similar way that Eq. 5.8 was used to approximate the pdf for some remaining background in the sample, the normalization integral may be approximated by

$$\frac{U}{N_{gen}} \sum_{i=1}^{N_{acc}} (A_\alpha(\vec{x_i}) A^*_{\alpha'})^{w_i} = \frac{U}{N_{gen}} \sum_{i=1}^{N_{acc}} A_\alpha(\vec{x_i}) A^*_{\alpha'}, \tag{7.1}$$

where the weights are used to account for systematic differences between data and MC samples. After the weighting process, the mass independent analysis is repeated using the same process as that described above. The results of the analysis with the reweighted MC samples are consistent with the nominal results. The pull distribution between the nominal results and those with this systematic effect are shown in Fig. 7.2. Here and below, a pull distribution is defined as the difference between the intensity or phase difference from the nominal results and those from an analysis with a systematic difference (such as a reweighted MC sample) divided by the error from the nominal results.

Normally for a systematic study like this, the difference between the results with the alternative phase space MC sample relative to the nominal results would be taken as the systematic uncertainty. In reality, the differences across the bins in the mass independent fit are correlated. This means it is not possible to simply take the difference in each bin as a systematic uncertainty. Fortunately, the differences between the results with the reweighted sample and the nominal sample as so small relative to the error on each bin that they may be neglected.

This same study was also performed for a similar systematic uncertainty due to differences in the photon detection efficiency between the inclusive MC sample and the data as a function of photon energy. The same procedure as that described above is applied using δ now as a function of photon energy (Fig. 7.3). The pull distributions are shown in Fig. 7.4.

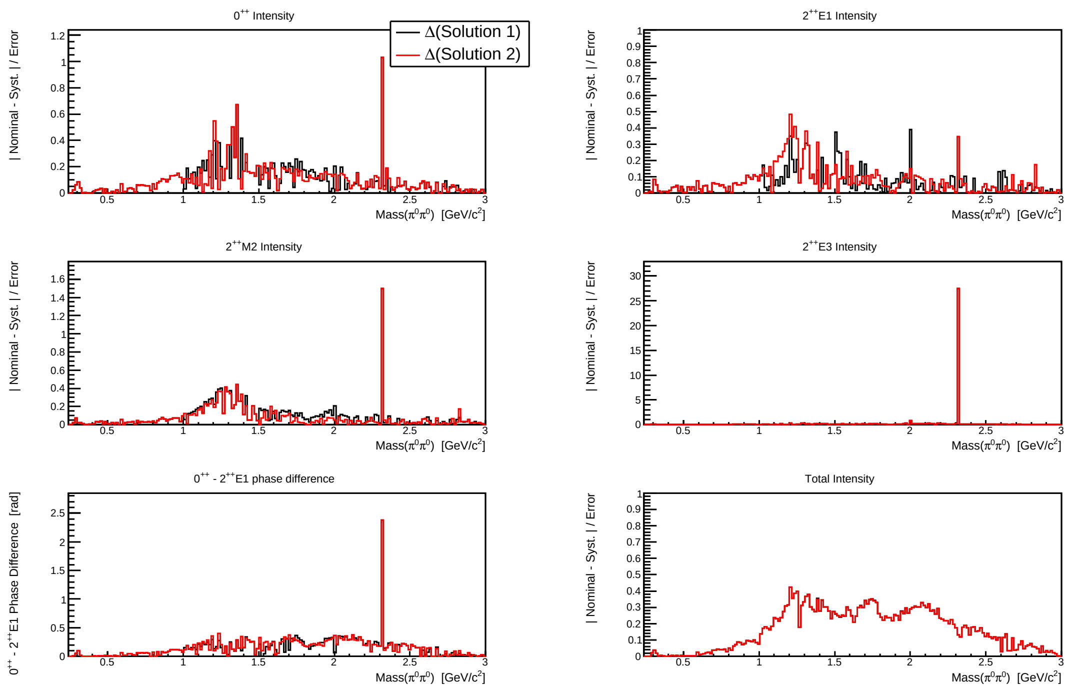

Figure 7.2: The pull distributions for the analysis with a MC sample that has been reweighted due to differences in the angular distributions of the photons for the inclusive MC sample relative to that in the data. Both the nominal results and the reweighted results exhibit ambiguous solutions in most bins. A pull distribution is plotted for each of the two sets of solutions. The results appear consistent with the nominal results.

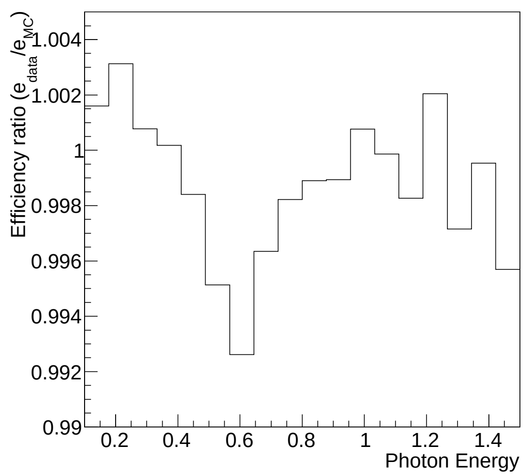

Figure 7.3: The difference in the photon detection efficiency between the inclusive MC and data samples as a function of photon energy is shown here. The difference is quantified by δ, where $\delta = e_{data}/e_{MC}$.

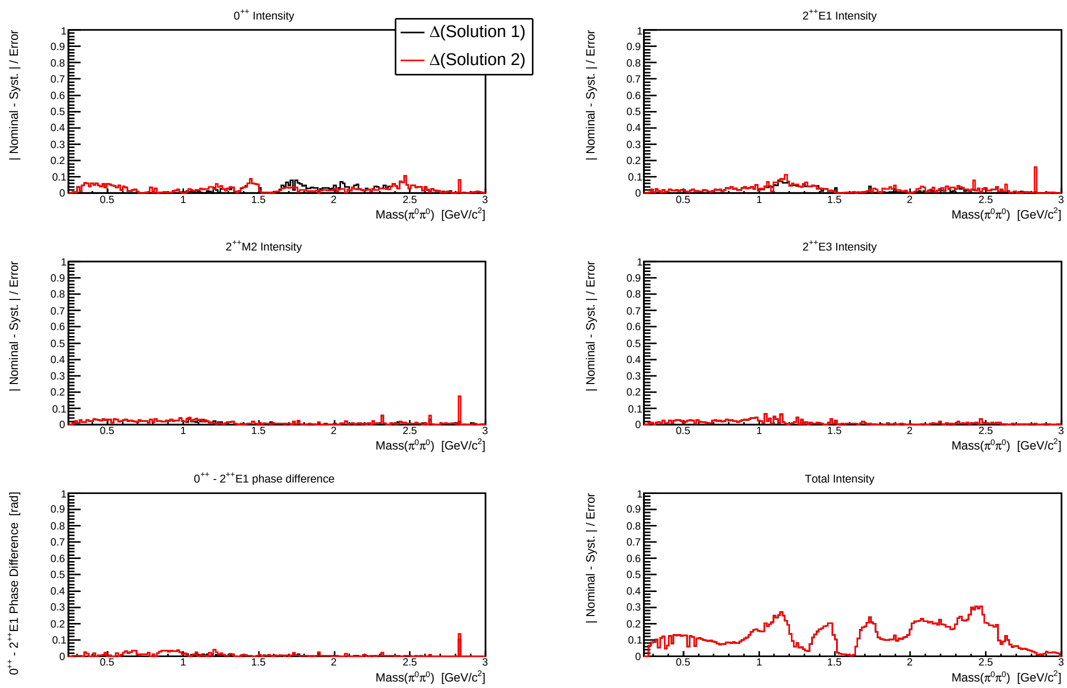

Figure 7.4: The pull distributions for the analysis with a MC sample that has been reweighted due to differences in the energy distributions of the photons in the inclusive MC sample relative to that in the data. Both the nominal results and the reweighted results exhibit ambiguous solutions in most bins. A pull distribution is plotted for each of the two sets of solutions. The results appear consistent with the nominal results.

7.1.2 Kinematic fit

Differences in the results of a kinematic fit between the data and MC sample may cause a systematic difference in the acceptance corrected signal yield. This effect was investigated by varying the selection criterion requiring each event with a $\pi^0\pi^0$ invariant mass above 0.99 GeV/c^2 to have a χ^2_{6C} from the kinematic fit to be less than 60. This restriction was instead relaxed to be less than 125. The results of the analysis with this loosened restriction are shown in Fig. 7.5 in comparison with the nominal results. The pull distributions are shown in Fig. 7.6.

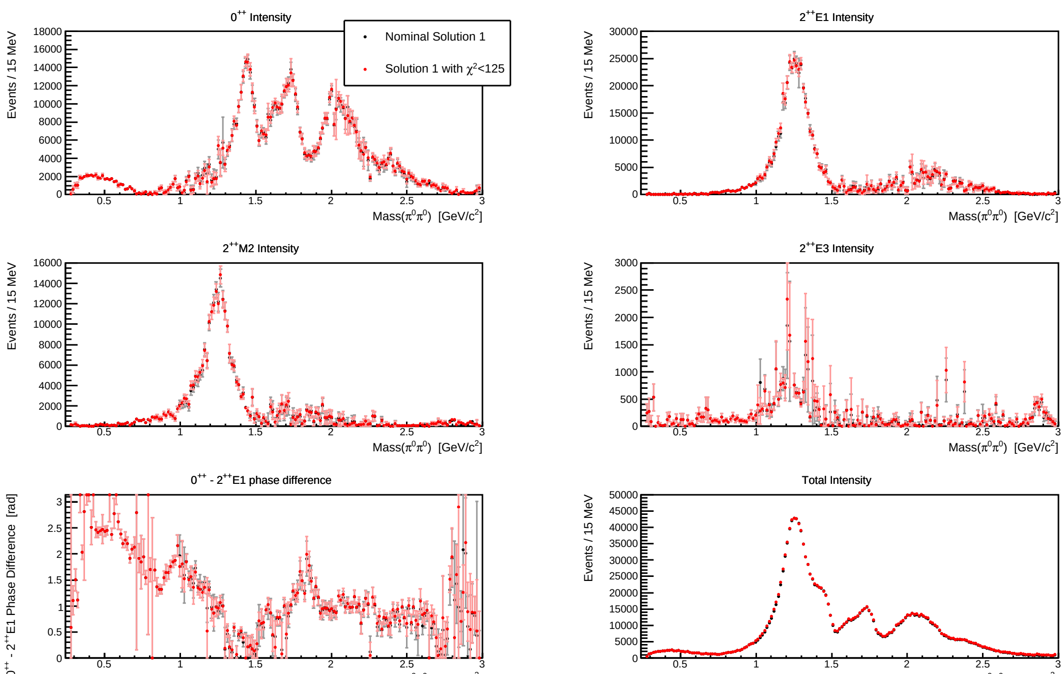

Figure 7.5: The intensity for each amplitude in the analysis with a loosened χ^2_{6C} restriction is plotted here as a function of $\pi^0\pi^0$ invariant mass by the red markers. For reference, the nominal results are shown by the black markers.

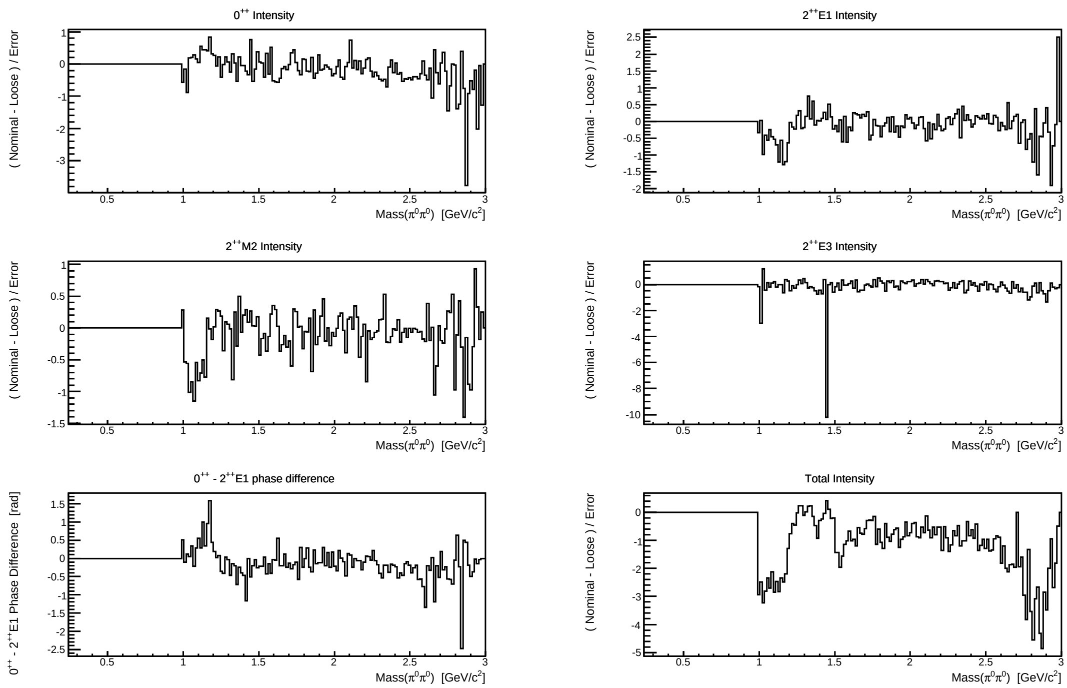

Figure 7.6: The pull distribution for each amplitude is plotted here as a function of $\pi^0\pi^0$ invariant mass. The vertical axis gives the difference between the intensities with the nominal and loosened χ^2_{6C} restriction divided by the error on the nominal results.

7.1.3 Misreconstructed backgrounds

Before the restriction on the invariant mass of the radiative photon paired with a π^0 daughter photon is applied, the background consisting of misreconstructed events causes a significant results on the fit. This effect is apparent by performing the mass independent analysis with and without the selection requirement. A comparison between these results is shown in Fig. 7.7. The pull distribution is determined by subtracting the approximate backgrounds in each bin from the total intensity. In this way, the value obtained from the nominal results is comparable to that taken from the results without the selection requirement. To confirm that this effect is due to this background, the same comparison is made with an exclusive MC sample (Fig. 7.8. The two sets of results appear consistent.

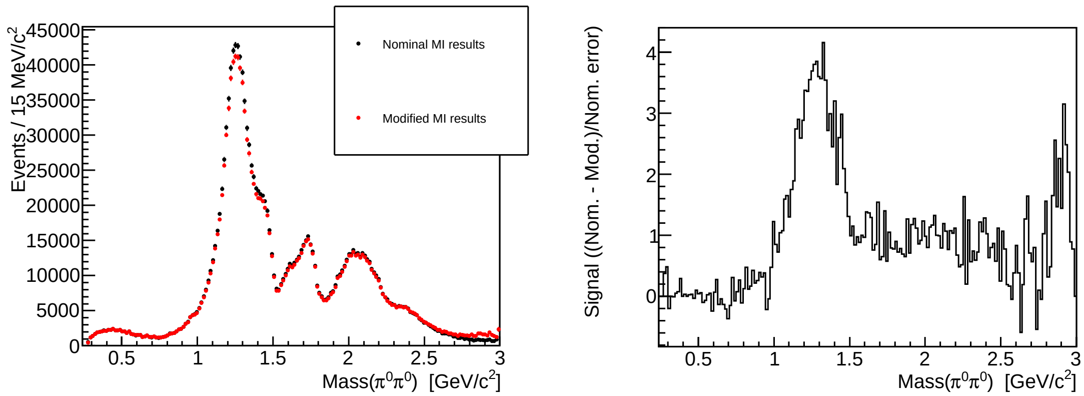

Figure 7.7: The total intensity from the mass independent analysis with and without the restriction on the radiative photon are shown on the left. The black markers give the nominal results while the red markers show the results without the restriction. On the right, the pull distribution for the results on the right is plotted.

The effect the misreconstructed backgrounds that remain after the selection requirements is studied by performing the mass independent amplitude analysis on an exclusive MC sample. This MC sample was generated according to the results of the model dependent analysis of the data and includes the proper angular distributions. After applying the same selection criteria that are applied to the data, the MC sample is passed through the mass independent analysis. This process is repeated after removing the remaining misreconstructed backgrounds from the sample. The results of the analysis with and without the misreconstructed backgrounds are shown in Fig. 7.9-7.11.

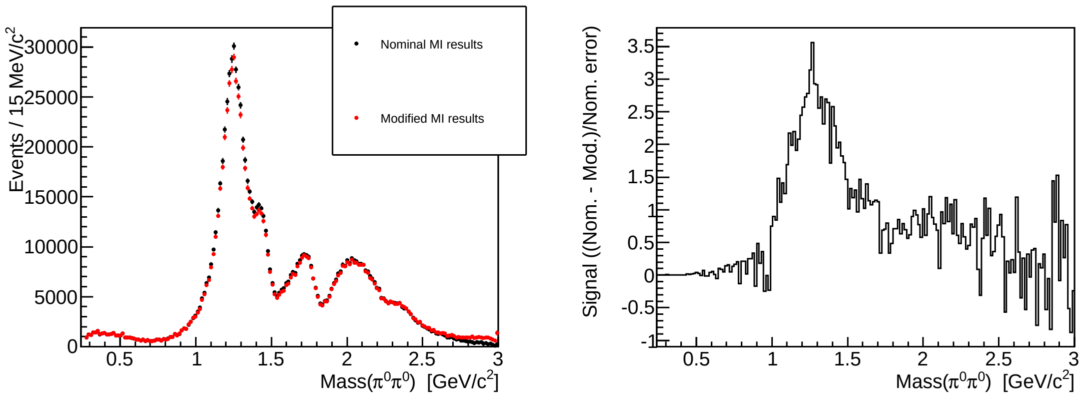

Figure 7.8: The total intensity from analysis on the MC sample with and without the restriction on the radiative photon are shown on the left. The black markers give the nominal results while the red markers show the results without the restriction. On the right, the pull distribution for the results on the right is plotted.

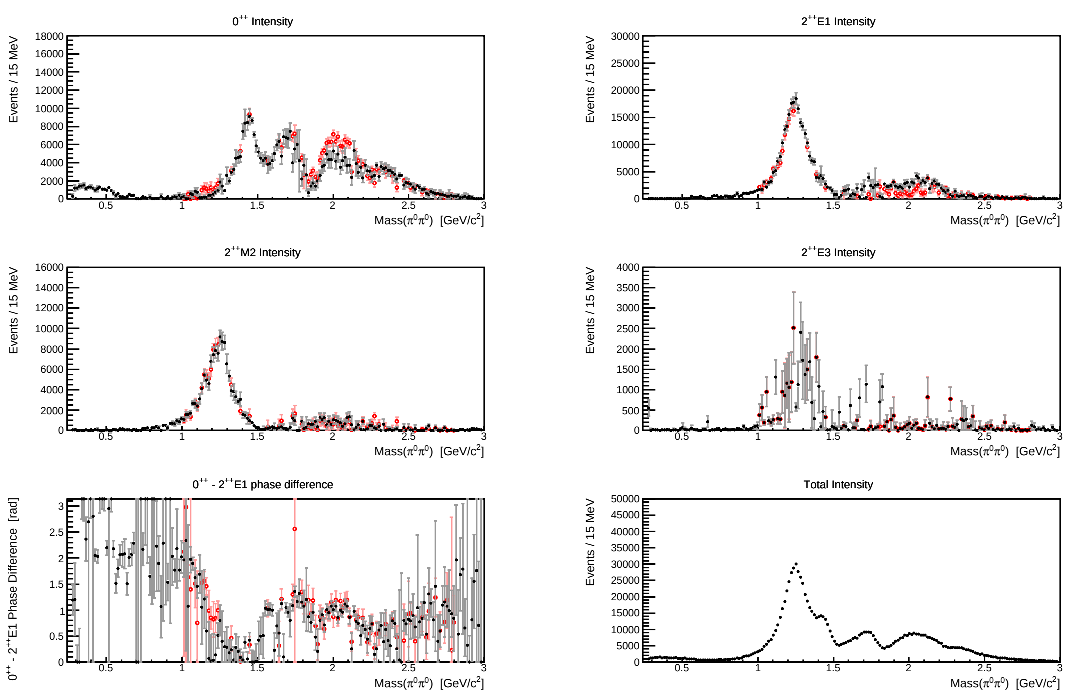

Figure 7.9: The intensity for each amplitude in the analysis with an exclusive MC sample.

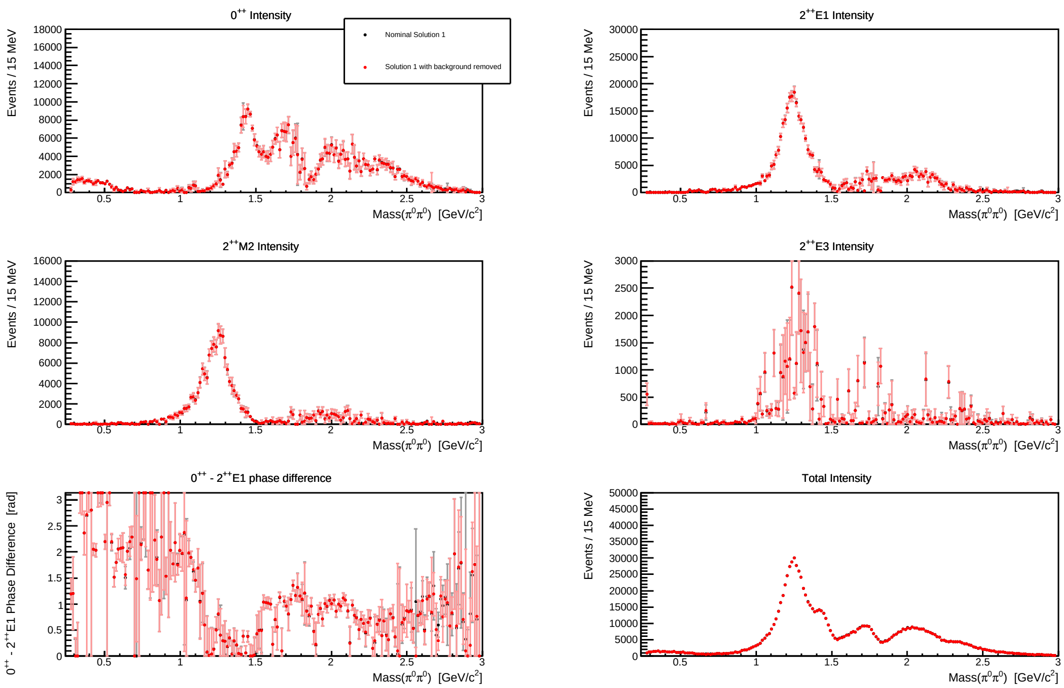

Figure 7.10: The intensity for each amplitude for the simulated results with the misreconstructed background removed is plotted here as a function of $\pi^0\pi^0$ invariant mass by the red markers. For reference, the results including the misreconstructed backgrounds are shown by the black markers.

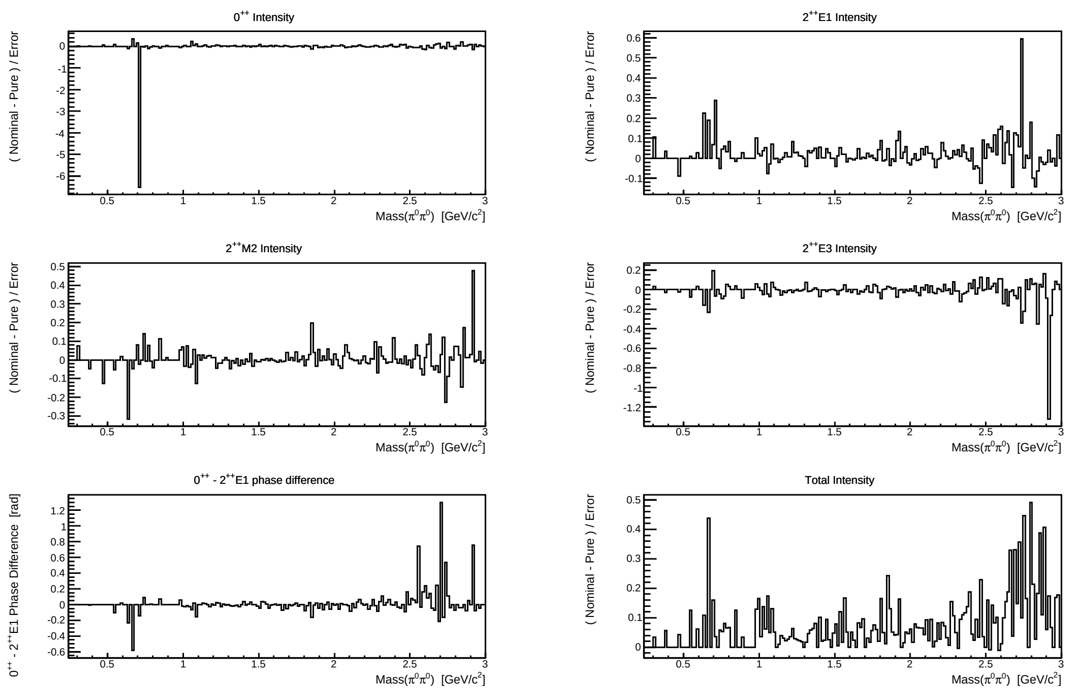

Figure 7.11: The pull distribution for each amplitude in the simulated analysis is plotted here as a function of $\pi^0\pi^0$ invariant mass. The vertical axis gives the difference between the intensities with and without the misreconstructed background divided by the error on the results including the background.

7.2 Correlated systematic uncertainties

While the mass independent amplitude analysis is intended to be model independent, several assumptions must be made. Differences in the results due to changing the conditions of or assumptions about the analysis are discussed here. Systematic differences due to these effects are correlated across mass bins in the results.

7.2.1 Model dependencies in the mass independent analysis

While the mass independent analysis is performed with the intention of eliminating as many model dependencies as possible, one remaining model assumption is whether or not to constrain the phases of the 2^{++} amplitudes. To allow for a systematic study of this model dependence, the results of the mass independent analysis are presented both with phases unconstrained (Fig. 6.3) and constrained (Fig. 6.11). These results are discussed in section 6.2.

7.2.2 Background subtraction

The uncertainty due to how the remaining backgrounds due to J/ψ decays to $\gamma\eta$ and $\gamma\eta'$ are addressed in the fit is studied in a similar manner. The mass independent analysis is repeated using the data sample with (Fig. 6.3) and without (Fig. 6.14) background subtraction. This allows for a test of how these background affect the shape of the $\pi^0\pi^0$ interaction.

7.2.3 Cross check: $\omega\pi^0$ background

One of the largest remaining backgrounds after signal isolation and background subtraction is due to the signal mimicking decay of J/ψ to $\omega\pi^0$, where the ω decays to $\gamma\pi^0$. The nominal method to address this background is to exclude the region of $\gamma\pi^0$ invariant mass within 50 MeV/c^2 of the ω mass. An alternate method of addressing this background is to remove this restriction and include an amplitude for the $\omega\pi^0$ final state in the analysis. The mass independent analysis is performed for both model assumptions. The results of the fits with phases unconstrained are shown in Figure 7.12. The pull distributions are shown in Fig. 7.13.

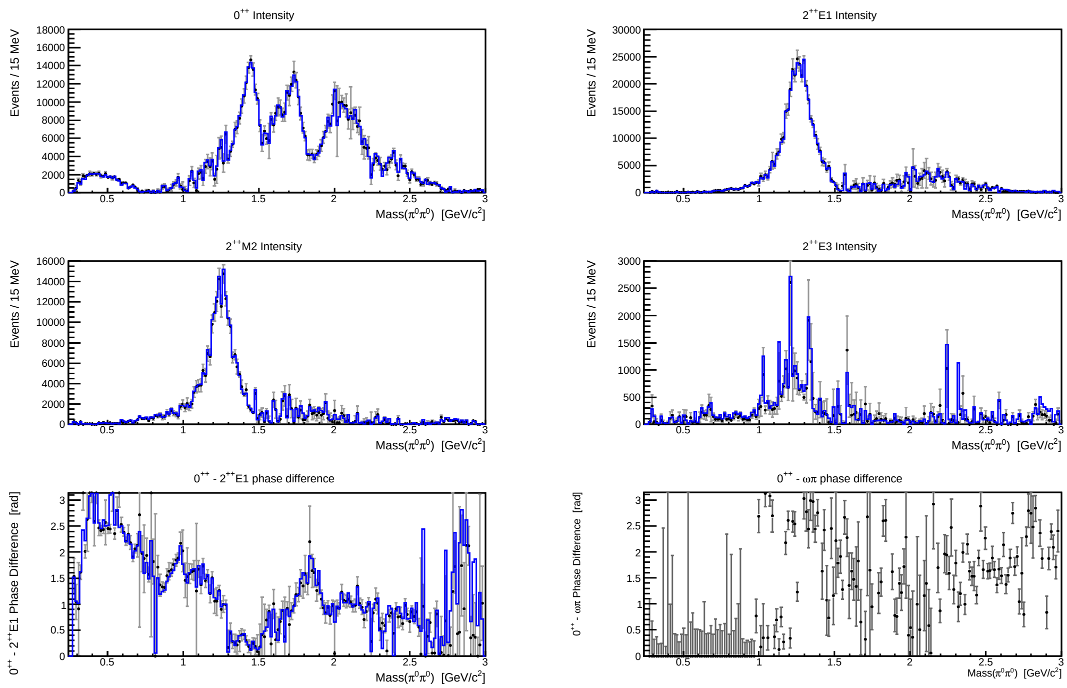

Figure 7.12: The intensity for each amplitude is plotted here as a function of $\pi^0\pi^0$ invariant mass. The results that include the $\omega\pi^0$ backgrounds, and an $\omega\pi^0$ amplitude, are given by the blue histogram. For reference, the nominal results are shown by the black markers. The intensity for the $\omega\pi^0$ amplitude is shown in the bottom left frame.

One additional result of the inclusion of an $\omega\pi^0$ amplitude to the analysis is the possibility of using the phase of the $\omega\pi^0$ to establish the phases of the other amplitudes in the fit. The results of the analysis, suggest that this is not feasible. This is primarily due to the fact that both the $\omega\pi^0$ amplitude and at least one other amplitude are only significant for a severely restricted region of phase space. The phase difference of the 0^{++} amplitude relative to the $\omega\pi^0$ is shown in the bottom right plot in Fig. 7.12.

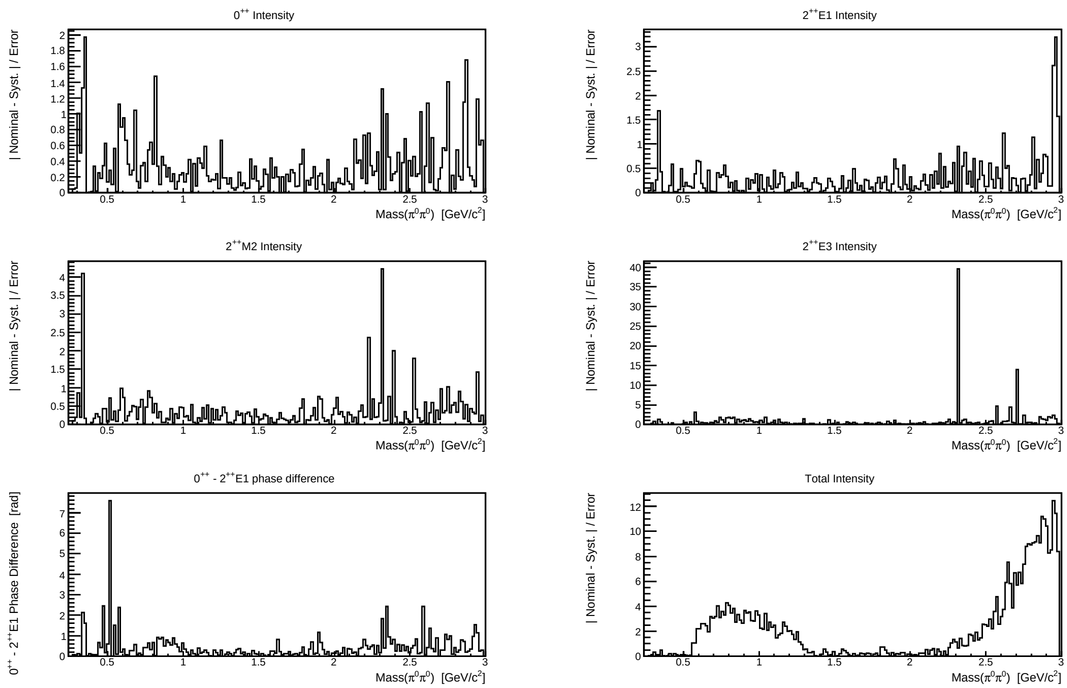

Figure 7.13: The pull distribution for each amplitude is plotted here as a function of $\pi^0\pi^0$ invariant mass. The vertical axis gives the difference between the intensities with and without the $\omega\pi^0$ backgrounds divided by the error on the nominal results for that amplitude.

7.2.4 Cross check: 4^{++} amplitude

As discussed above, angular momentum and parity considerations dictate that the only amplitudes that contribute to decays of the J/ψ to $\gamma\pi^0\pi^0$ must have even J and positive parity and charge conjugation. Both the 0^{++} and 2++ amplitudes have obvious contributions to the spectrum, but additional amplitudes may make some contributions as well. To test this hypothesis, the mass independent analysis is repeated with the addition of a 4^{++} amplitude.

In the radiative multipole basis, the 4^{++} amplitude has three pieces (similarly to the 2^{++} amplitude). The mass independent analysis is repeated, including each permutation of the three 4^{++} amplitudes (E3, M4, and E5). For each combination, the difference in likelihood for each bin with and without the 4^{++} amplitude(s) is plotted. The significance of the additional amplitude can be approximated by taking the ratio of the log likelihoods and treating the result as a χ^2 value in the high statistics limit [80]. The significance would then be given by

$$S(2) = \sqrt{-2\ln L_{\text{with }4^{++}} + 2\ln L_{\text{without }4^{++}}}, \tag{7.2}$$

where the addition of the 4^{++} introduces two additional degrees of freedom to the fit. Thus, a difference of $-2\ln L$ of 9 would correspond to a 3σ significance for the 4^{++} wave. No significant contribution from a 4^{++} amplitude is obvious.

Figures 7.14-7.20 show the results of the fits with 4^{++} amplitudes along with the intensity for the most significant component of the 4^{++} amplitude included in each fit. For each of these plots, the y-axis is the difference in -2ln L without the additional wave minus the likelihood with it. Therefore, a positive value of likelihood indicates that the fit prefers the inclusion of the amplitude. For comparison purposes, the likelihood difference with the removal of the 2^{++} E3 component, which certainly appears significant, is shown in Fig. 7.21. For reference, the intensity of the 2^{++} E3 component across all mass bins is about 2% of the total intensity.

One interesting aspect of this study is the possibility to compare these results with those from the mass dependent analysis (section 6.3). Including an $f_4(2050)$ in the mass dependent analysis improves the likelihood by about 234 units, but the intensity is very small. Including instead an $f_4(2300)$ only improves the likelihood by about 38 units and also has a very small intensity. The masses of these resonances do not appear stable in the fit. That is, when allowed to float, the mass parameters are moved to the upper limit of the parameter. When floated the width of the $f_4(2300)$ is determined to be a reasonable 0.32 GeV/c^2, but the width of the $f_4(2050)$ blows up over 0.7 GeV/c^2. The contribution from these resonances from the mass dependent analysis are overlaid on the mass independent results with a 4^{++} amplitude in Fig.

7.14 and Fig. 7.20.

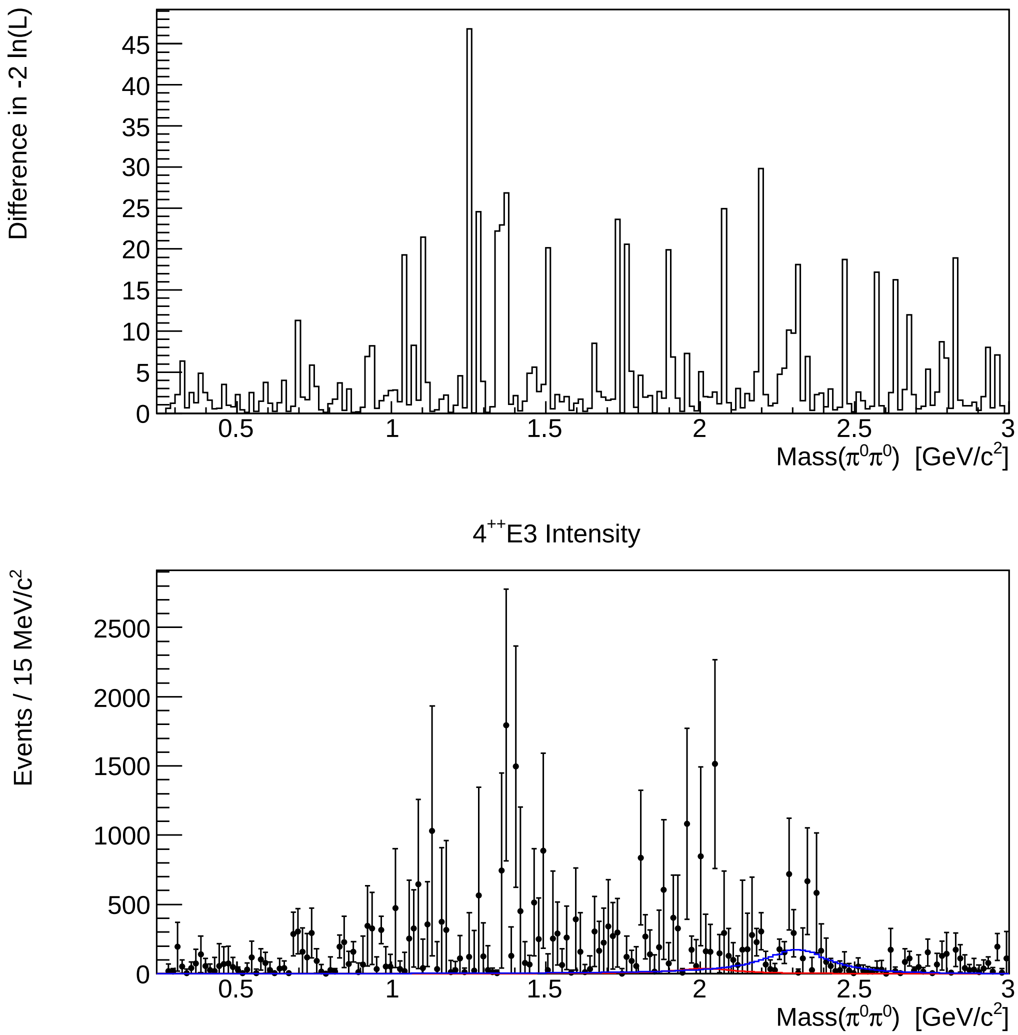

Figure 7.14: The top plot shows the likelihood difference between the nominal results and those with an additional 4^{++} E3 component. The bottom plot shows the intensity for the most significant 4^{++} amplitude in the fit (E3). The red histogram shows the contribution of an $f_4(2050)$ to the mass dependent fit, while the blue histogram shows that of an $f_4(2300)$.

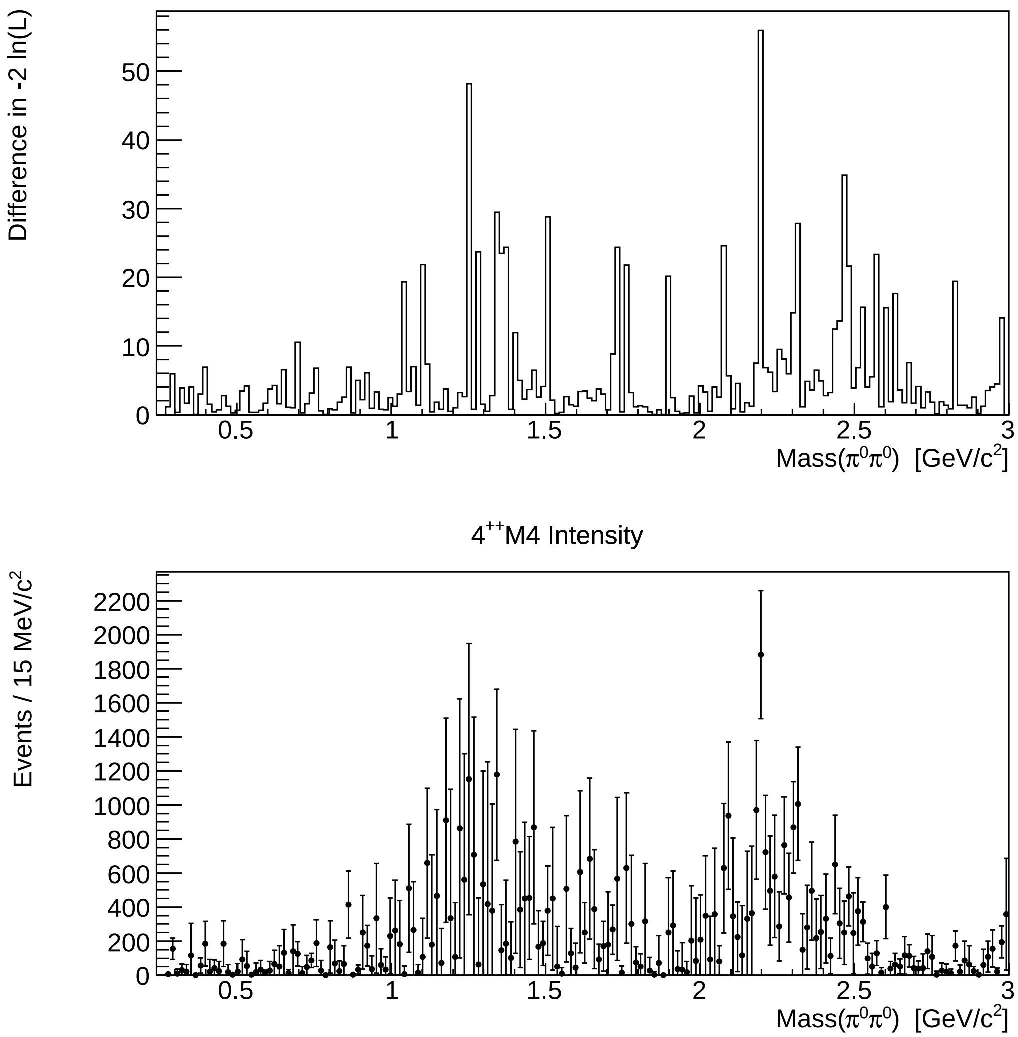

Figure 7.15: The top plot shows the likelihood difference between the nominal results and those with an additional 4^{++} M4 component. The bottom plot shows the intensity for the most significant 4^{++} amplitude in the fit (M4).

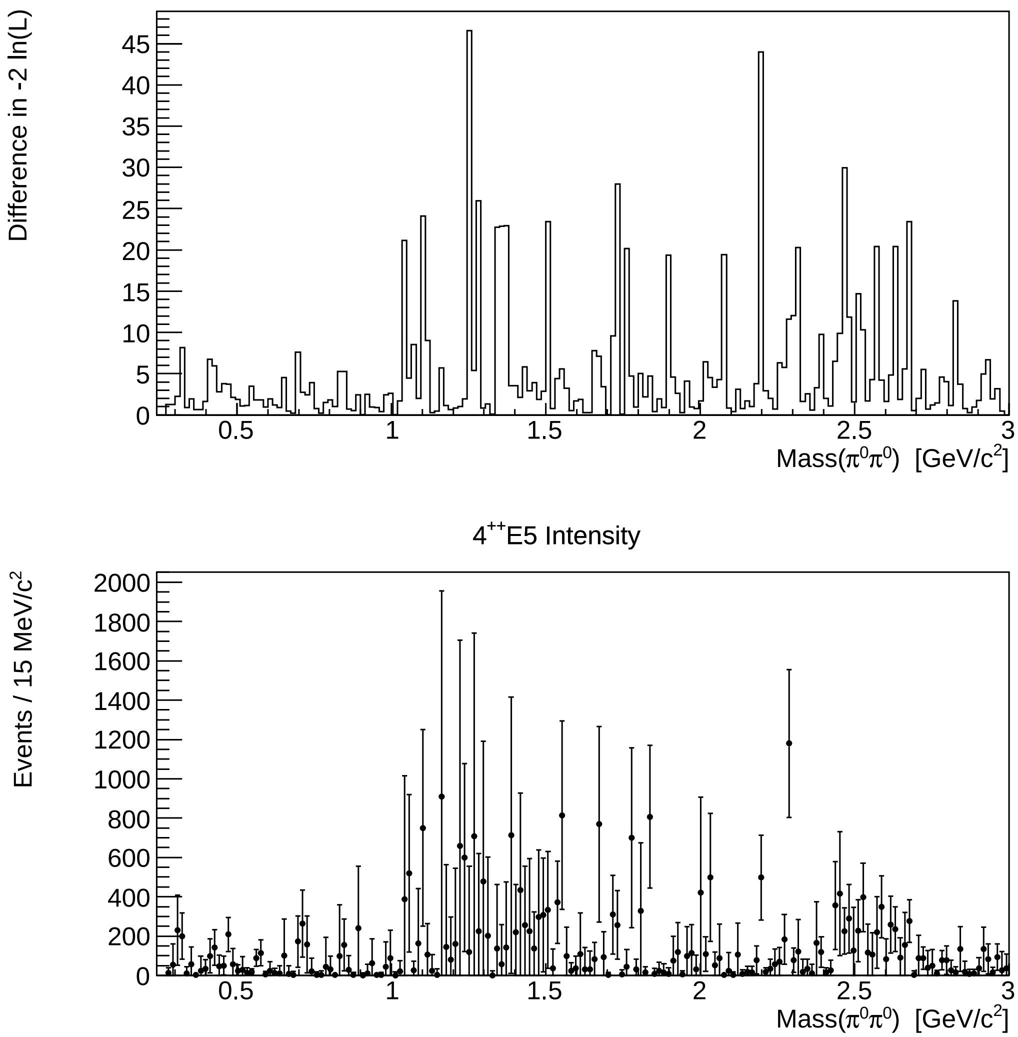

Figure 7.16: The top plot shows the likelihood difference between the nominal results and those with an additional 4^{++} E5 component. The bottom plot shows the intensity for the most significant 4^{++} amplitude in the fit (E5).

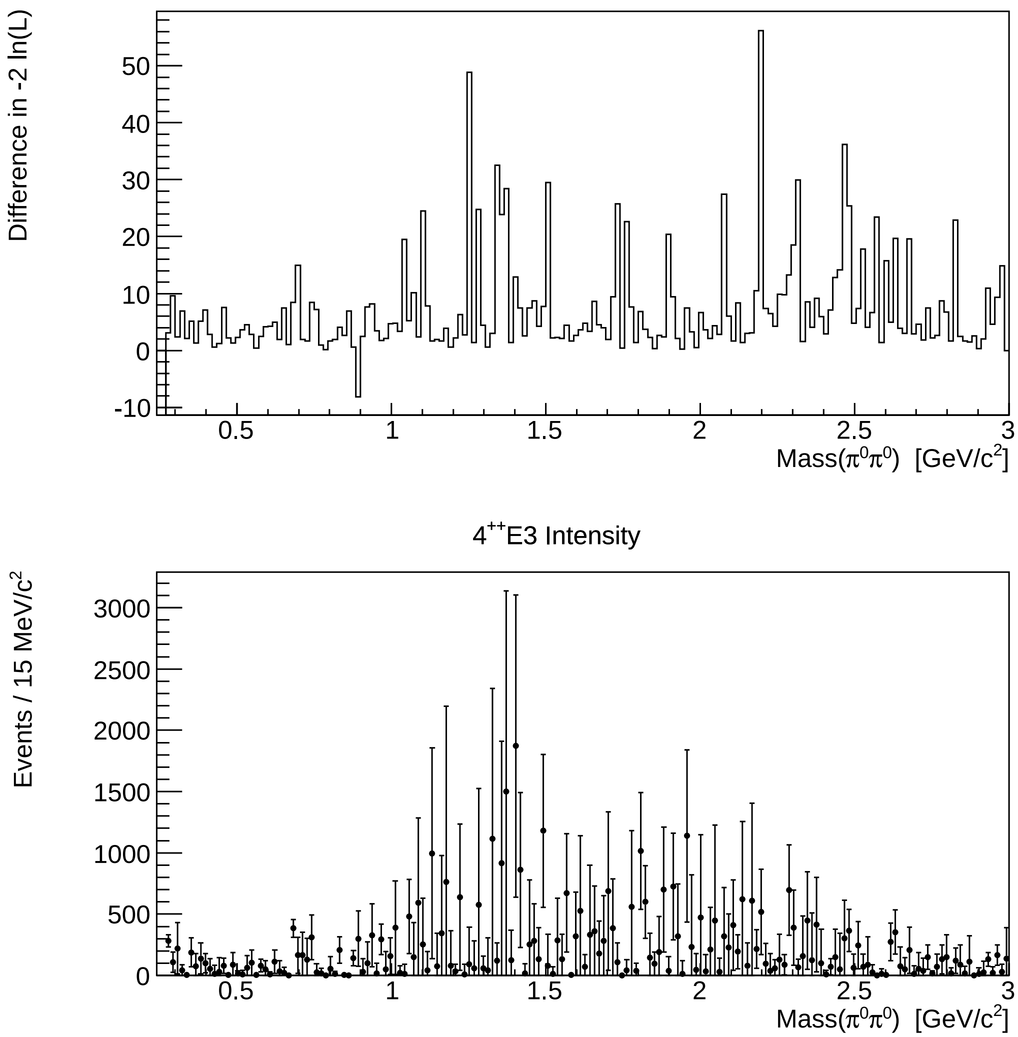

Figure 7.17: The top plot shows the likelihood difference between the nominal results and those with an additional 4^{++} E3 and M4 component. The bottom plot shows the intensity for the most significant 4^{++} amplitude in the fit (E3).

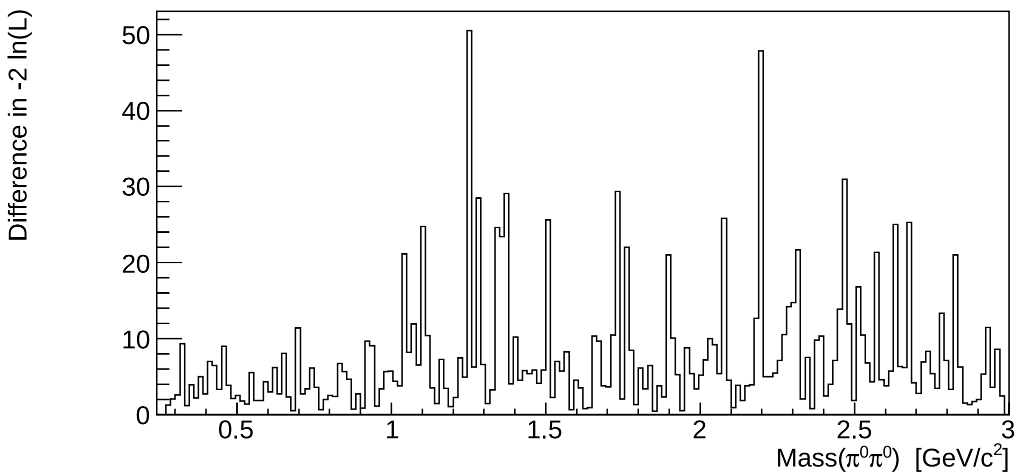

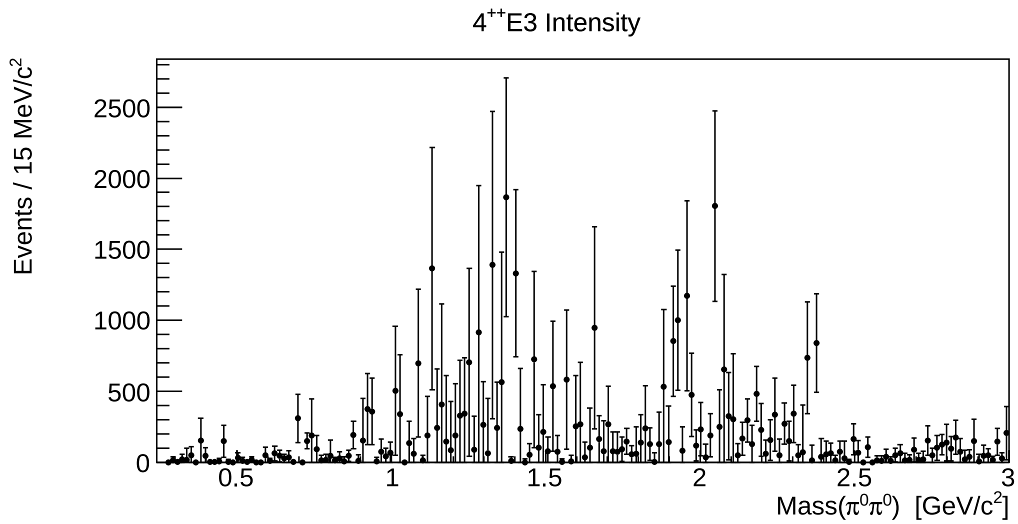

Figure 7.18: The top plot shows the likelihood difference between the nominal results and those with an additional 4^{++} E3 and E5 component. The bottom plot shows the intensity for the most significant 4^{++} amplitude in the fit (E3).

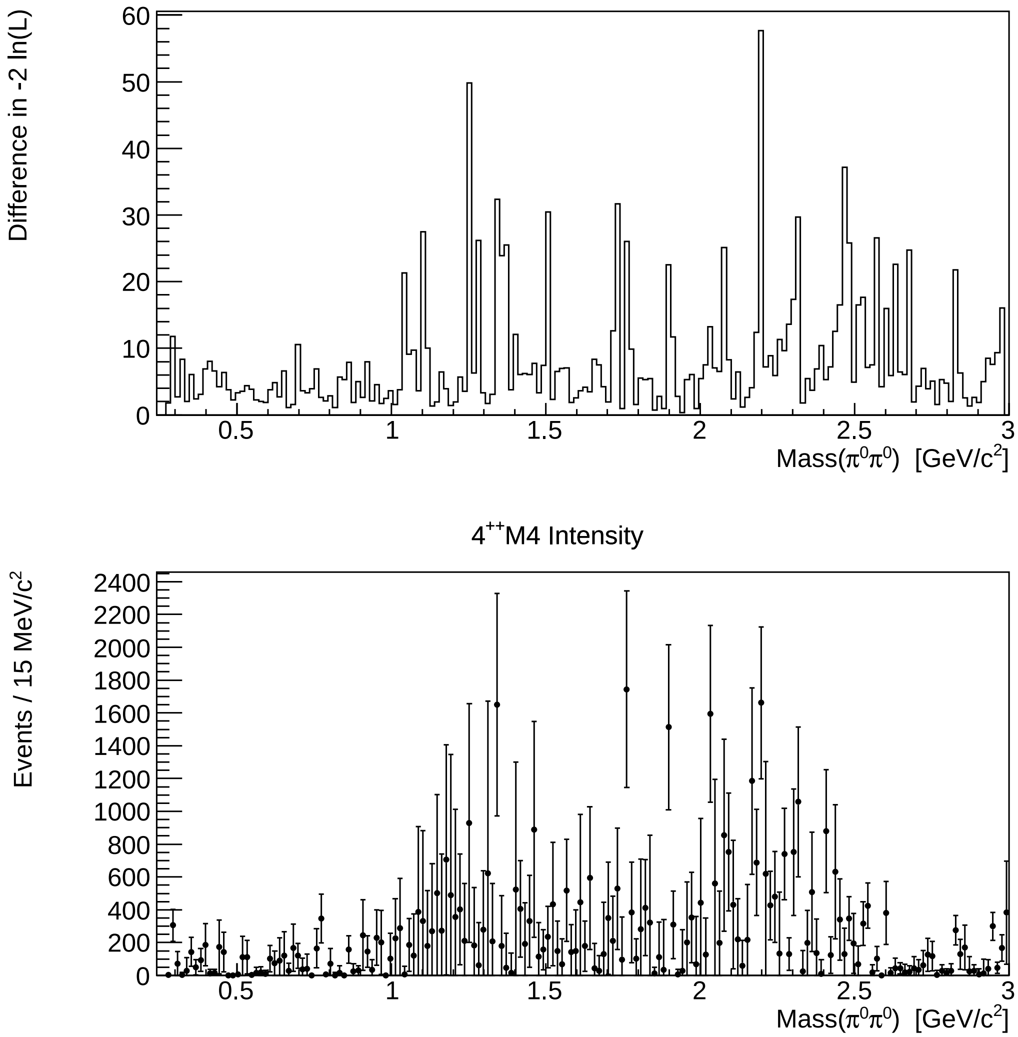

Figure 7.19: The top plot shows the likelihood difference between the nominal results and those with an additional 4^{++} M4 and E5 component. The bottom plot shows the intensity for the most significant 4^{++} amplitude in the fit (M4).

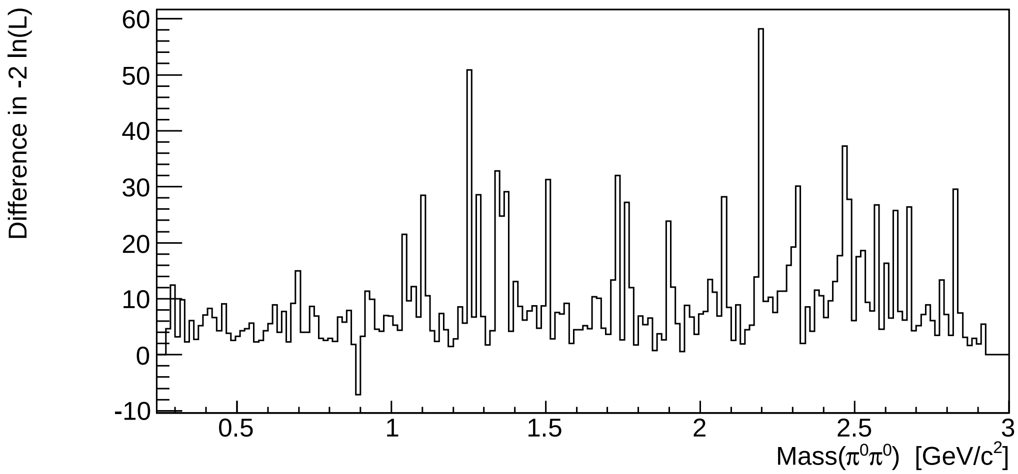

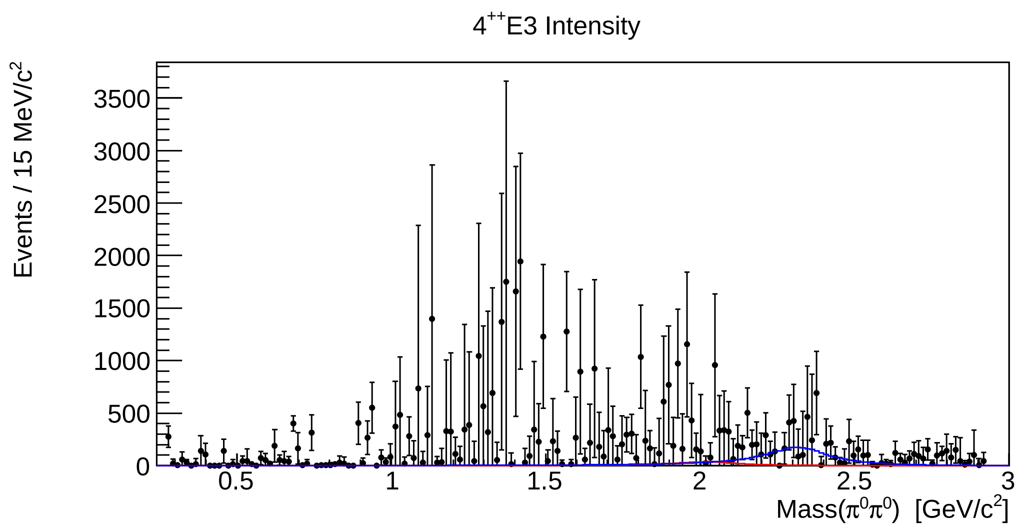

Figure 7.20: The top plot shows the likelihood difference between the nominal results and those with an additional 4^{++} E3, M4, and E5 component. The bottom plot shows the intensity for the most significant 4^{++} amplitude in the fit (E3). The red histogram shows the contribution of an $f_4(2050)$ to the mass dependent fit, while the blue histogram shows that of an $f_4(2300)$.

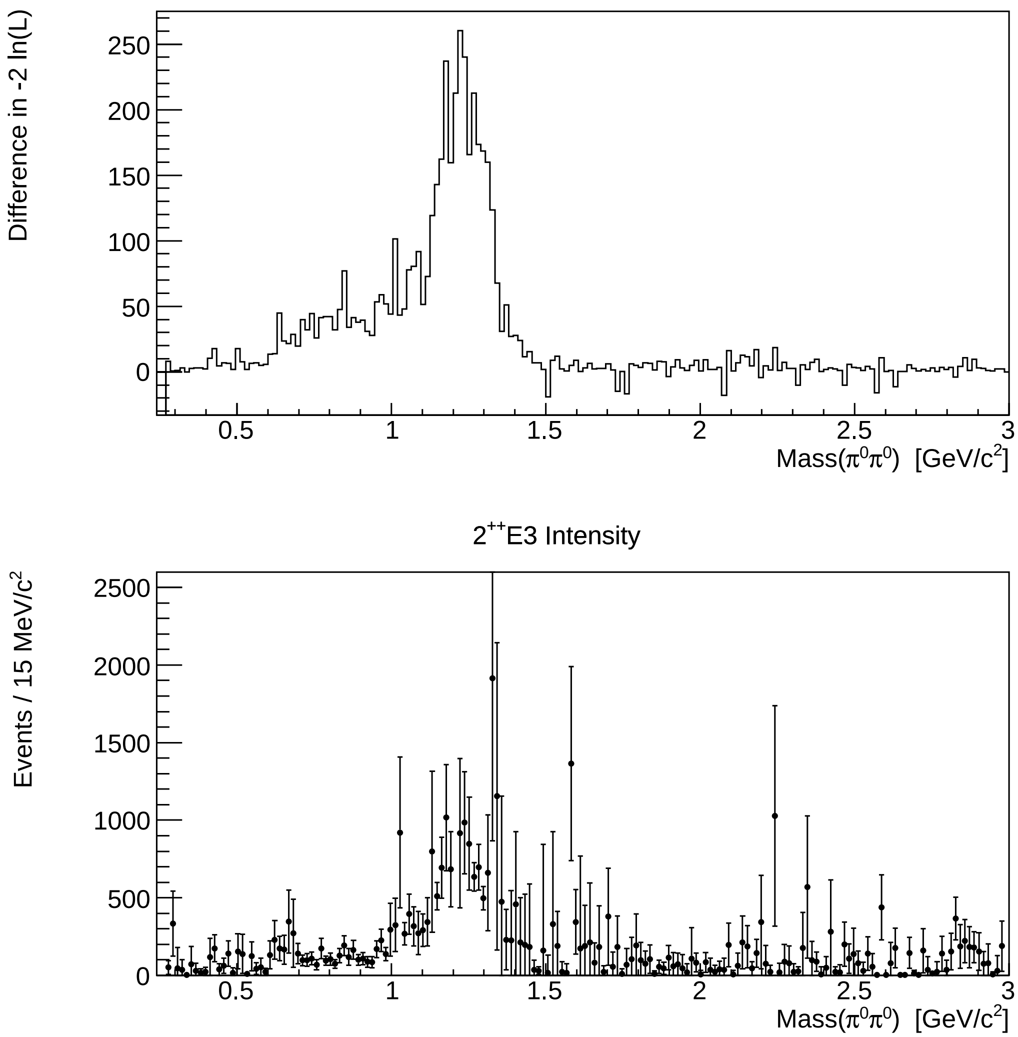

Figure 7.21: The top plot shows the likelihood difference between the nominal results with and without the 2^{++} E3 component. The bottom plot shows the intensity for the 2^{++} E3 amplitude.

Chapter 8

Conclusions

An amplitude analysis of the $\pi^0\pi^0$ system in radiative J/ψ decays has been performed using the world's largest data sample of its type, collected by the BESIII collaboration. A mass independent amplitude analysis is presented under several different assumptions in order to allow for systematic studies of model dependencies. The intensities and phase differences for the amplitudes in the fit are presented as a function of $\pi^0\pi^0$ invariant mass. Additionally, the amplitudes in each bin will be made available along with the correlation matrices and normalization information. These results may be of use for more complete analyses of the scalar spectrum.

In addition to the mass independent analysis, a mass dependent analysis is performed using interacting Breit-Wigner line shapes. The results of each analysis type appear consistent with each other. This suggests that the results of the mass independent amplitude analysis are a faithful representation of the data sample. The structures present in the mass independent analysis also appear in the mass dependent analysis. The 2^{++} amplitude is dominated by an $f_2(1270)$, with some additional contributions by the $f_2'(1525)$. There also appears to be some contribution from several higher mass tensor resonances, for example the $f_2(1950)$ and the $f_2(2150)$. Visible in the 0^{++} amplitude is the $f_0(500)$ (the σ), the $f_0(1500)$, the $f_0(1710)$, the $f_0(2020)$, and the $f_0(2300)$. There is also some evidence of an $f_0(980)$. The mass, width, and fit fraction of each resonance included in the mass dependent analysis is presented in Tab. 6.2.

The presence of the $f_0(1500)$ in both the mass independent and mass dependent analyses is an important observation. A glueball state is expected to be observed in a glue-rich environment like radiative decays of the J/ψ, but not in two photon collisions [59]. The fact that this is true for the $f_0(1500)$ provides important information for the interpretation of this state.

Finally, the branching ratio of radiative J/ψ decays to $\pi^0\pi^0$ is measured to be $(1.147 \pm 0.002 \pm 0.042) \times 10^{-3}$, where the first error is statistical and the second is systematic. This is the first measurement of this reaction.

Bibliography

[1] J. Beringer et al [Particle Data Group], Phys. Rev. D **86**, 010001 (2012).

[2] J. Gunter et al [E852 Collaboration], Phys. Rev. D **64**, 072003 (2001).

[3] A. Abele et al [Crystal Barrel Collaboration], Phys. Lett. B **380**, 453 (1996).

[4] R. Bellazzini et al [GAMS Collaboration], Phys. Lett. B **467**, 296 (1999).

[5] M. Ablikim et al [BES Collaboration], Phys. Lett. B **645**, 19 (2007).

[6] M. Ablikim et al [BES Collaboration], Phys. Lett. B **607**, 243 (2005).

[7] M. Ablikim et al [BES Collaboration], Phys. Lett. B **598**, 149 (2004).

[8] M. Ablikim et al [BES Collaboration], Phys. Lett. B **603**, 138 (2004).

[9] J. P. Lees et al [BaBar Collaboration], Phys. Rev. D **85**, 112010 (2012).

[10] G. Bonvicini et al [CLEO Collaboration], Phys. Rev. D **76**, 012001 (2007).

[11] J. R. Batley et al [NA48/2 Collaboration], Eur. Phys. J. C **54**, 411 (2008).

[12] T. Mori at al [Belle Collaboration], Phys. Rev. D **75**, 051101 (2007).

[13] A. Aloisio et al [KLOE Collaboration], Phys. Lett. B **537**, 21 (2002).

[14] J. R. Pelaez and F. J. Yndurain, Phys. Rev. D **71**, 074016 (2005).

[15] G. S. Bali, K. Shilling, A. Hulsebos, A. C. Irving, C. Michael, and P. Stephenson, Phys. Lett. B **309**, 378 (1993).

[16] C. J. Morningstar and M. J. Peardon, Phys. Rev. D **60**, 034509 (1999).

[17] Y. Chen, A. Alexandru, S. Dong, T. Draper, I. Horvath, F. Lee, K. Liu, N. Mathur, C. Morningstar, M. Peardon, S. Tamhankar, B. Young, and J. Zhang, Phys. Rev. D **73**, 014516 (2006).

[18] M. Ablikim et al [BES Collaboration], Phys. Lett. B **642**, 441 (2006).

[19] R. Molina, D. Nicmorus, and E. Oset, Phys. Rev. D **78**, 114018 (2008).

[20] L. S. Geng, F. K. Guo, C. Hanhart, R. Molina, E. Oset, and B. S. Zou, Eur. Phys. J. A **44**, 305 (2010).

[21] J. Z. Bai et al [BES Collaboration], Phys. Rev. D **68** (2003).

[22] F. E. Close and A. Kirk, Eur. Phys. J. C **21**, 531 (2001).

[23] C. Amsler and N. A. Tornqvist, Phys. Rep. **389**, 61 (2004).

[24] R. L. Lander, ed., *Proceedings of the VI International Workshop on Photon-Photon Collisions* (World Scientific, 1984).

[25] R. Barate et al [ALEPH Collaboration], Phys. Lett. B **472**, 189 (2000).

[26] F. E. Close, G. R. Farrar, and Z. Li, Phys. Rev. D **55** (1997).

[27] J. Becker et al [Mark-III Collaboration], Phys. Rev. D **35** (1987).

[28] J.E. Augustin et al [DM2 Collaboration], Z. Phys. C **36** (1987).

[29] J. Z. Bai et al [BES Collaboration], Phys. Rev. Lett. **76** (1996).

[30] L. Kopke and N. Wermes, Phys. Rep. **36**, 67 (1989).

[31] J. Z. Bai et al [BES Collaboration], Phys. Rev. Lett. **81** (1998).

[32] W. N. Cottingham and D. A. Greenwood, *An introduction to the standard model of particle physics*, 2nd ed. (Cambridge University Press, 2007).

[33] D. Griffiths, *Introductino to Elementary Particles* (Wiley-VCH, 2008).

[34] G. Aad et al [Atlas Collaboration], Phys. Lett. B **710**, 49 (2012).

[35] S. Chatrchyan et al [CMS Collaboration], Phys. Lett. B **710**, 26 (2012).

[36] J. J. Dudek, R. G. Edwards, P. Guo, and C. E. Thomas, Phys. Rev. D **88**, 0945505 (2013).

[37] V. Anisovich and A. Sarantsev, Eur. Phys. J. A **16**, 229 (2003).

[38] R. Garcia-Martin, R. Kaminski, J. R. Pelaez, and J. R. de Elvira, Phys. Rev. Lett. **107**, 072001 (2011).

[39] E. Klempt and A. Zaitsev, Phys. Rep. **454**, 1 (2007).

[40] G. Grayer, B. Hyams, C. Jones, P. Schlein, P. Weihammer, W. Blum, H. Dietl, W. Koch, E. Lorenz, G. Lutjens, W. Manner, J. Meissburger, W. Ochs, and U. Stierlin, Nucl. Phys. B **75**, 189 (1974).

[41] H. Becker et al [CERN-Cracow-Munich Collaboration], Nucl. Phys. B **151**, 46 (1979).

[42] J.R. Batley et al [NA48/2 Collaboration], Eur. Phys. J. C **70**, 635 (2010).

[43] D. H. Cohen, D. S. Ayers, R. Diebold, S. L. Kramer, A. J. Pawlicki, and A. B. Wicklund, Phys. Rev. D **22**, 2595 (1980).

[44] A. Etkin et al, Phys. Rev. D **25**, 1786 (1982).

[45] C. Amsler et al [Crystal Barrel Collaboration], Phys. Lett. B **355**, 425 (1995).

[46] D. Alde et al [GAMS Collaboration], Phys. Lett. B **397**, 350 (1997).

[47] A. Gallegos, J. L. L. M., and J. Pestieau, Phys. Rev. D **69**, 074033 (2004).

[48] M. Ishida, S. Ishida, T. Komada, and S.-I. Matsumoto, Phys. Lett. B **518**, 47 (2001).

[49] N. Achasov and G. Shestakov, Phys. Rev. D **58**, 054011 (1998).

[50] A. Aloisio et al [KLOE Collaboration], Phys. Lett. B **536**, 209 (2002).

[51] F. Ambrosino et al [KLOE Collaboration], Eur. Phys. J. C **49**, 473 (2007).

[52] J. Weinstein and N. Isgur, Phys. Rev. Lett. **48** (1982).

[53] H.-J. Lee, N. Kochelev, and Y. Oh, Phys. Rev. D **87**, 117901 (2013).

[54] A. J. Pawlicki, D. S. Ayers, D. H. Cohen, R. Diebold, S. L. Kramer, and A. B. Wicklund, Phys. Rev. D **15**, 3196 (1977).

[55] P. Estabrooks, Phys. Rev. D **19**, 2678 (1979).

[56] L. Li, B.-S. Zou, and G.-L. Li, Phys. Rev. D **67**, 034025 (2003).

[57] D. V. Bugg, Eur. Phys. J. C **52**, 55 (2007).

[58] D. Barberis et al [WA102 Collaboration], Phys. Lett. B **462**, 462 (1999).

[59] M. Acciarri, Phys. Lett. B **501**, 173 (2001).

[60] C. Edwards et al, Phys. Rev. Lett. **48**, 458 (1982).

[61] C. Amsler et al [Crystal Barrel Collaboration], Eur. Phys. J. C **23**, 29 (2002).

[62] S. Uehara et al [Belle Collaboration], Prog. Theor. Exp. Phys. (2013).

[63] J. Z. Bai et al [BES Collaboration], Phys. Lett. B **472**, 207 (2000).

[64] A. V. Anisovich, C. A. Baker, C. J. Batty, D. V. Bugg, C. Hodd, H. C. Lu, V. A. Nikonov, A. V. Sarantsev, V. V. Sarantsev, and B. S. Zou, Phys. Lett. B **491**, 47 (2000).

[65] F. G. Binon et al, Phys. At. Nucl. **70**, 1713 (2007).

[66] Z.-C. Ye, X. Wang, X. Liu, and Q. Zhao, Phys. Rev. D **86**, 054025 (2012).

[67] F. G. Binon et al, Phys. At. Nucl. **68**, 960 (2005).

[68] D. V. Amelin et al, Phys. At. Nucl. **69**, 690 (2006).

[69] D. Barberis et al [WA102 Collaboration], Phys. Lett. B **484**, 198 (2000).

[70] M. Ablikim et al [BES Collaboration], Nucl. Instr. and Metho. A **614**, 345 (2010).

[71] R. A. Briere et al [CLEO Collaboration], "CLEO-c and CESR-c: a new frontier of weak and strong interactions," (2001), cornell LEPP preprint CLNS 01/1742.

[72] W. Li et al, Proceeding of CHEP2006 (2006).

[73] G. Barrand, I. Belyaev, P. Binko, M. Cattaneo, R. Chytracek, G. Corti, M. Frank, G. Gracia, J. Harvey, E. van Herwijnen, P. Maley, P. Mato, S. Probst, and F. Ranjard, Comput. Phys. Commun. **140**, 45 (2001).

[74] C. Arnault, Proceeding of CHEP2000 (2000).

[75] Z. Y. Deng, G. F. Cao, C. D. Fu, M. He, H. M. Liu, Y. J. Mao, Y. Xia, Z. Y. You, Y. Yuan, and R. Tang, Chinese Physics C **30**, 371 (2006).

[76] S. Jadach, B. F. L. Ward, and Z. Was, Comput. Phys. Commun. **130** (2000).

[77] R. G. Ping, Chinese Physics C **32** (2008).

[78] J. C. Chen, G. S. Huang, X. R. Qi, D. H. Zhang, and Y. S. Zhu, Phys. Rev. D **62**, 034003 (2000).

[79] T. Kunihiro, Prog. Theor. Phys. Supplement **149**, 56 (2003).

[80] F. James, *Statistical Methods in Experimental Physics* (World Scientific, 2006).

[81] T. Skwarnicki, *A study of the radiative CASCADE transitions between the Upsilon − Prime and Upsilon resonances*, Ph.D. thesis (1986).

[82] A. M. Badalyan, Phys. Rep. **82** (1982).

[83] M. Ablikim et al [BES Collaboration], "Determination of the number of J/ψ events with $J/\psi \to$*inclusive* decays," (2014), BAM-00123.

[84] E. Eisenhandler, W. R. Gibson, C. Hojvat, P. I. P. Kalmus, L. C. Y. Lee, T. W. Pritchard, E. C. Usher, and D. T. Williams, Nucl. Phys. B **96** (1975).

[85] A. Etkin, K. J. Foley, R. S. Longacre, W. A. Love, T. W. Morris, E. D. Platner, V. A. Polychronakos, A. C. Saulys, and C. D. Wheeler, Phys. Rev. Lett. **49** (1982).

[86] R. S. Longacre and S. J. Lindenbaum, Phys. Rev. D **70** (2004)

Appendix A

Ambiguities

One of the difficulties of amplitude analyses is the problem of ambiguous solutions, two solutions that give the same distribution. In this section, the ambiguous solutions for radiative J/ψ decays to $\pi^0\pi^0$ are studied.

In the radiative multipole basis, the decay amplitude is given by

$$\begin{aligned} A_{\alpha=(M,\lambda_\gamma)\beta=(J_\gamma,j_{12},\mu_{12})}(\vec{x}) = \sum_{\mu_{12}} N_{J_\gamma} D^{J}_{M,\mu_{12}-\lambda_\gamma}(\pi+\phi_\gamma,\pi-\theta_\gamma,\phi_1) N_{j_{12}} d^{j_{12}}_{\mu_{12},0}(\theta_1) \\ \langle J_\gamma,-\lambda_\gamma; j_{12},\mu_{12}|J,\mu_{12}-\lambda_\gamma\rangle \frac{1}{\sqrt{2}}[\delta_{\lambda_\gamma,1}+\delta_{\lambda_\gamma,-1}(-1)^{J_\gamma-1}] \end{aligned} \tag{A.1}$$

where (ϕ_γ,θ_γ) represent the angular distribution of the radiated photon in the J/ψ rest frame and (ϕ_1,θ_1) represents the angular distribution of one of the π^0 mesons in the $\pi^0\pi^0$ rest frame. N_j is a normalization factor which is given by

$$N_j = \sqrt{\frac{2j+1}{4\pi}}. \tag{A.2}$$

By expanding out the Wigner D functions,

$$
\begin{aligned}
A_{\alpha,\beta}(\vec{x}) =& \sum_{\mu_{12}} c^{J_\gamma,\lambda_\gamma}_{j_{12},\mu_{12}} N_{J_\gamma} N_{j_{12}} D^{1}_{M,\mu_{12}-\lambda_\gamma}(\pi+\phi_\gamma, \pi-\theta_\gamma, \phi_1) \\
& \times d^{j_{12}}_{\mu_{12},0}(\theta_1) \frac{1}{\sqrt{2}} [\delta_{\lambda_\gamma,1} + \delta_{\lambda_\gamma,-1}(-1)^{J_\gamma-1}] \\
=& \sum_{\mu_{12}} c^{J_\gamma,\lambda_\gamma}_{j_{12},\mu_{12}} N_{J_\gamma} N_{j_{12}} e^{-\imath M(\pi+\phi_\gamma)} d^{1}_{M,\mu_{12}-\lambda_\gamma}(\pi-\theta_\gamma) e^{-\imath(\mu-\lambda_\gamma)\phi_1} \\
& \times d^{j_{12}}_{\mu_{12},0}(\theta_1) \frac{1}{\sqrt{2}} [\delta_{\lambda_\gamma,1} + \delta_{\lambda_\gamma,-1}(-1)^{J_\gamma-1}]
\end{aligned}
\tag{A.3}
$$

where the constants $c^{J_\gamma,\lambda_\gamma}_{j_{12},\mu_{12}}$ contain the Clebsch Gordan factors. The angular momentum of the J/ψ is also explicitly written as one. Additionally, let us restrict our attention only to values of $j_{12} = 0, 2$ (the two lowest order partial waves allowed by parity considerations). We can also realize that the Clebsch Gordan factors restrict the signs of μ_{12} to be the same as that of λ_{gamma}. Thus, for $j_{12} = 2$ and $\lambda_\gamma = 1$, only the values $\mu_{12} = 0, 1, 2$ give non-zero amplitude contributions. It is also important to note that the sign of the Clebsch Gordan coefficients will change sign under $\lambda_\gamma \to -\lambda_\gamma$, but only for $J_\gamma = 2$. This will cancel the delta functions in the decay amplitude, with the result

$$
\begin{aligned}
A_{\alpha,\beta}(\vec{x}) =& \sum_{\mu_{12}} c^{J_\gamma,\lambda_\gamma}_{j_{12},\mu_{12}} N_{J_\gamma} N_{j_{12}} e^{-\imath M(\pi+\phi_\gamma)} d^{1}_{M,\mu_{12}-\lambda_\gamma}(\pi-\theta_\gamma) \\
& \times e^{-\imath(\mu-\lambda_\gamma)\phi_1} d^{j_{12}}_{\mu_{12},0}(\theta_1) [\delta_{\lambda_\gamma,1} + \delta_{\lambda_\gamma,-1}(-1)^{J_\gamma-1}].
\end{aligned}
\tag{A.4}
$$

Recall that, for the small d functions, $d^1_{1,\pm1}(\pi-\theta) = d^1_{1,\mp1}(\theta)$ and $d^1_{1,0}(\pi-\theta) = d^1_{1,0}(\theta)$. Then, $d^1_{M,\mu-\lambda_\gamma}(\pi-\theta) = d^1_{M,\lambda_\gamma-\mu_{12}}(\theta)$. Also, note that the restrictions on μ_{12} mean that the factor $\mu_{12}-\lambda_\gamma = \pm1, 0$. It is also useful to note that $\mu-\lambda_\gamma = \lambda_\gamma, 0, -\lambda_\gamma$, for $\mu = \pm2, \pm1, 0$ respectively. The usefulness of these features appears when one writes out the intensity for a given choice of M and λ_γ. It is also useful to plug in the values for the constants, which are given by

$$
\begin{array}{ccc}
 & c^{J_\gamma,\lambda_\gamma}_{0,0} = 1 & \\
c^{1,\pm1}_{2,0} = \sqrt{\frac{1}{10}} & c^{2,\pm1}_{2,0} = \pm\sqrt{\frac{3}{10}} & c^{3,\pm1}_{2,0} = \sqrt{\frac{6}{35}} \\
c^{1,\pm1}_{2,1} = \sqrt{\frac{3}{10}} & c^{2,\pm1}_{2,1} = \pm\sqrt{\frac{1}{10}} & c^{3,\pm1}_{2,1} = -\sqrt{\frac{8}{35}} \\
c^{1,\pm1}_{2,2} = \sqrt{\frac{3}{5}} & c^{2,\pm1}_{2,2} = \mp\sqrt{\frac{1}{5}} & c^{3,\pm1}_{2,2} = \sqrt{\frac{1}{35}}
\end{array}
$$

Now, the intensity for a given choice of observables is given by

$$
\begin{aligned}
I_{M,\lambda_\gamma}(\vec{x}) =& \frac{1}{32\pi^2}|\sqrt{3}d^1_{M,\lambda_\gamma}(\theta_\gamma)[V_{0,1} + \frac{1}{2}d^2_{0,0}(\theta_1)(V_{2,1} + \sqrt{5}V_{2,2} + 2V_{2,3})]e^{\imath\lambda_\gamma\phi_1} \\
&+\frac{1}{\sqrt{2}}d^1_{M,0}(\theta_\gamma)d^2_{1,0}(\theta_1)(3V_{2,1} + \sqrt{5}V_{2,2} - 4V_{2,3}) \\
&+d^1_{M,-\lambda_\gamma}(\theta_\gamma)d^2_{2,0}(\theta_1)(3V_{2,1} - \sqrt{5}V_{2,2} + V_{2,3})]e^{-\imath\lambda_\gamma\phi_1}|^2,
\end{aligned}
\tag{A.5}
$$

where $V_{\alpha,\beta}$ is given by V_{j_{12},J_γ}. Each term has a specific value for μ_{12} and therefore $\mu_{12} - \lambda_\gamma$ as described above. Hence it is possible to group terms with the same angular dependencies. The values of the coefficients have also been written explicitly. Things will simplify a bit if we group the θ_1 dependence into new functions, $h_{\mu_{12}}(\theta_1)$ as defined by

$$
\begin{aligned}
I(\vec{x}) = \sum_{M,\lambda_\gamma} & |h_0(\theta_1)d^1_{M,\lambda_\gamma}(\theta_\gamma)e^{\imath\lambda_\gamma\phi_1} + h_1(\theta_1)d^1_{M,0}(\theta_\gamma) \\
& + h_2(\theta_1)d^1_{M,-\lambda_\gamma}(\theta_\gamma)e^{-\imath\lambda_\gamma\phi_1}|^2.
\end{aligned}
\tag{A.6}
$$

Then,

$$
\begin{aligned}
h_0(\theta_1) &= \sqrt{3}V_{0,1} + \sqrt{\frac{3}{2}}(V_{2,1} + \sqrt{5}V_{2,2} + 2V_{2,3})d^2_{0,0}(\theta_1) \\
h_1(\theta_1) &= \frac{1}{\sqrt{2}}(3V_{2,1} + \sqrt{5}V_{2,2} - 4V_{2,3})d^2_{1,0}(\theta_1) \\
h_2(\theta_1) &= (3V_{2,1} - \sqrt{5}V_{2,2} + V_{2,3})d^2_{2,0}(\theta_1).
\end{aligned}
\tag{A.7}
$$

The amplitudes for which M and λ_γ have the same (opposite) sign, $M = \lambda_\gamma = \pm1$ ($M = -\lambda_\gamma = \pm1$) are related to each other by a sign change in the exponential factor.

Note that the terms with a factor of $d^1_{M,0}$ will change sign under $M \to -M$ and terms with a factor of $d^{j_{12}}_{\mu_{12},0}$ will change sign under $\lambda_\gamma \to -\lambda_\gamma$. Then, the intensity becomes

$$\begin{aligned} I(\vec{x}) = & \sum_{M=\lambda_\gamma=\pm1} |h_0(\theta_1) d^1_{1,1}(\theta_\gamma) e^{\pm\imath\phi_1} + h_1(\theta_1) d^1_{1,0}(\theta_\gamma) \\ & \qquad + h_2(\theta_1) d^1_{1,-1}(\theta_\gamma) e^{\mp\imath\phi_1}|^2 \\ + & \sum_{M=-\lambda_\gamma=\pm1} |h_0(\theta_1) d^1_{1,-1}(\theta_\gamma) e^{\pm\imath\phi_1} - h_1(\theta_1) d^1_{1,0}(\theta_\gamma) \\ & \qquad + h_2(\theta_1) d^1_{1,1}(\theta_\gamma) e^{\mp\imath\phi_1}|^2. \end{aligned} \tag{A.8}$$

Note that the term with $h_1(\theta_1)$ has changed sign in the opposite combination. The properties of small d functions, $d^j_{m',m}(\theta) = (-1)^{m-m'} d^j_{m,m'}(\theta) = d^j_{-m,-m'}(\theta)$, have been used to write the incoherent pieces of the intensity in the same way.

Now we can write the intensity in several pieces (in terms of ϕ_1 dependence);

$$\begin{aligned} I_0(\vec{x}) =& 2[(h_0)^2 (d^1_{1,1})^2 + (h_1)^2 (d^1_{1,0})^2 + (h_2)^2 (d^1_{1,-1})^2] \\ & + 2[(h_0)^2 (d^1_{1,-1})^2 + (h_1)^2 (d^1_{1,0})^2 + (h_2)^2 (d^1_{1,1})^2] \\ =& [(h_0)^2 + (h_2)^2][1 + \cos^2\theta_\gamma] + 2(h_1)^2 \sin^2\theta_\gamma, \end{aligned} \tag{A.9}$$

$$\begin{aligned} I_1(\vec{x}) =& 2[(h_0 h_1^* + h_0^* h_1) d^1_{1,1} d^1_{1,0} + (h_2 h_1^* + h_2^* h_1) d^1_{1,-1} d^1_{1,0}] \cos\phi_1 \\ & -2[(h_0 h_1^* + h_0^* h_1) d^1_{1,-1} d^1_{1,0} + (h_2 h_1^* + h_2^* h_1) d^1_{1,1} d^1_{1,0}] \cos\phi_1 \\ =& \sqrt{2}(-h_0 h_1^* - h_0^* h_1 + h_2 h_1^* + h_2^* h_1) \sin\theta_\gamma \cos\theta_\gamma \cos\phi_1, \end{aligned} \tag{A.10}$$

$$\begin{aligned} I_2(\vec{x}) =& 4(h_0 h_2^* + h_0^* h_2) d^1_{1,1} d^1_{1,-1} \cos 2\phi_1 \\ =& (h_0 h_2^* + h_0^* h_2) \sin^2\theta_\gamma \cos 2\phi_1 \end{aligned} \tag{A.11}$$

So the total intensity is given by

$$\begin{aligned}
I(\vec{x}) =& [(h_0)^2 + (h_2)^2][1 + \cos^2\theta_\gamma] + 2(h_1)^2 \sin^2\theta_\gamma \\
&+ \sqrt{2}(-h_0 h_1^* - h_0^* h_1 + h_2 h_1^* + h_2^* h_1) \sin\theta_\gamma \cos\theta_\gamma \cos\phi_1 \\
&+ (h_0 h_2^* + h_0^* h_2) \sin^2\theta_\gamma \cos 2\phi_1
\end{aligned} \tag{A.12}$$

Which can be modified slightly to give

$$\begin{aligned}
I(\vec{x}) =& \frac{3}{2}[(h_0)^2 + (h_2)^2] + (h_1^2) + \{\frac{1}{2}[(h_0)^2 + (h_2)^2] - (h_1)^2\} \cos 2\theta_\gamma \\
&+ \frac{1}{2}(h_0 h_2^* + h_0^* h_2) \cos 2\phi_1 \\
&+ \frac{1}{\sqrt{2}}(-h_0 h_1^* - h_0^* h_1 + h_2 h_1^* + h_2^* h_1) \sin 2\theta_\gamma \cos\phi_1 \\
&- \frac{1}{2}(h_0 h_2^* + h_0^* h_2) \cos 2\theta_\gamma \cos 2\phi_1
\end{aligned} \tag{A.13}$$

It is instructive to write the intensity function as

$$\begin{aligned}
I(\vec{x}) =& f_0 + f_1 \cos 2\theta_\gamma + \frac{1}{2} f_2 \cos 2\phi_1 \\
&+ \frac{1}{2} f_3 \sin 2\theta_\gamma \cos\phi_1 - \frac{1}{2} f_4 \cos 2\theta_\gamma \cos 2\phi_1.
\end{aligned} \tag{A.14}$$

Comparing the two expressions for the intensity, it is apparent that

$$\begin{aligned}
f_0 &= \frac{3}{2}[(h_0)^2 + (h_2)^2] + (h_1^2) \\
f_1 &= \frac{1}{2}[(h_0)^2 + (h_2)^2] - (h_1)^2 \\
f_2 &= f_4 = (h_0 h_2^* + h_0^* h_2) \\
f_3 &= \sqrt{2}(-h_0 h_1^* - h_0^* h_1 + h_2 h_1^* + h_2^* h_1).
\end{aligned} \tag{A.15}$$

Now, assume a set of production amplitudes, V_i, have been found by fitting the intensity function in Eq. A.14 to the data. Ambiguities would arise if an alternative set of amplitude couplings, V_i', would give the same angular dependence as the original set. In other words, the new set of amplitudes must give the same values for the f_i

functions ($f_i' = f_i$).

Consider f_2, which can be written as a linear combination of two quadratic forms

$$f_2 = \frac{1}{2}(|h_0 + h_2|^2 - |h_0 - h_2|^2). \tag{A.16}$$

These quadratic forms are given by

$$|h_0 \pm h_2|^2 = [\cos^2\theta_1(3a_1 \mp a_3) + (b - a_1 \pm a_3)] \times [\cos^2\theta_1(3a_1^* \mp a_3^*) + (b^* - a_1^* \pm a_3^*)], \tag{A.17}$$

where for simplicity the production coefficients have been combined into new variables given by

$$\begin{aligned} b &= \sqrt{3}V_{0,1} \\ a_1 &= \frac{\sqrt{6}}{4}(V_{2,1} + \sqrt{5}V_{2,2} + 2V_{2,3}) \\ a_2 &= -\frac{\sqrt{3}}{4}(3V_{2,1} + \sqrt{5}V_{2,2} - 4V_{2,3}) \\ a_3 &= \frac{\sqrt{6}}{4}(3V_{2,1} - \sqrt{5}V_{2,2} + V_{2,3}). \end{aligned} \tag{A.18}$$

Since the only the absolute square of each combination of h_0 and h_2 appears in the intensity, nontrivial ambiguous solutions only appear when the production coefficients are replaced by their complex conjugate for one choice of sign in Eq. A.17. That is, if $u_1 = (b, a_1, a_2, a_3)$ and $u_2 = (b', a_1', a_2', a_3')$, the solutions $\{u_1, u_2\}$ and $\{u_1, u_2^*\}$ should give consistent values for $h_0 \pm h_2$. This requires that either

$$\begin{aligned} h_0 + h_2 &= h_0' + h_2' \\ h_0 + h_2 &= h_0'^* + h_2'^* \end{aligned} \tag{A.19}$$

or

$$
\begin{aligned}
h_0 - h_2 &= h_0' - h_2' \\
h_0 - h_2 &= h_0'^* - h_2'^*.
\end{aligned}
\tag{A.20}
$$

Therefore, either

$$
\begin{aligned}
3a_1' - a_3' &= 3a_1^* - a_3^* \\
b' - a_1' + a_3' &= b^* - a_1^* + a_3^* \\
3a_1' + a_3' &= 3a_1 + a_3 \\
b' - a_1' - a_3' &= b - a_1 - a_3
\end{aligned}
\tag{A.21}
$$

or

$$
\begin{aligned}
3a_1' - a_3' &= 3a_1 - a_3 \\
b' - a_1' + a_3' &= b - a_1 + a_3 \\
3a_1' + a_3' &= 3a_1^* + a_3^* \\
b' - a_1' - a_3' &= b^* - a_1^* - a_3^*.
\end{aligned}
\tag{A.22}
$$

Now, Eq. A.21 requires that

$$
\begin{aligned}
\text{Im } b &= -2\text{Im } a_1 \\
\text{Re } b' &= \text{Re } b \\
\text{Im } b' &= -\frac{2}{3}\text{Im } a_3.
\end{aligned}
\tag{A.23}
$$

A.22 requires instead that

$$
\begin{aligned}
\text{Im } b &= -2\text{Im } a_0 \\
\text{Re } b' &= \text{Re } b \\
\text{Im } b' &= -\frac{2}{3}\text{Im } a_2,
\end{aligned}
\tag{A.24}
$$

which simply implies that there is a phase ambiguity. One can choose a convention for the sign of the phase of the total amplitude, which resolves this ambiguity. Let us choose the phase convention given by Eq. A.21. Finally, invariance of f_1, given the conditions above, requires that $a'_2 = a_2$. Therefore, the alternate set of solutions can be written in terms of the original set

$$\begin{aligned}
\text{Re } V'_{0,0} &= \text{Re } V_{0,0} \\
\text{Im } V'_{0,0} &= -\frac{1}{3\sqrt{2}}(3\text{Im } V_{2,1} - \sqrt{5}\text{Im } V_{2,2} + \text{Im } V_{2,3}) \\
\text{Re } V'_{2,1} &= \text{Re } V_{2,1} \\
\text{Im } V'_{2,1} &= \text{Im } V_{2,1} + \frac{2\sqrt{5}}{3}\text{Im } V_{2,2} + \frac{5}{6}\text{Im } V_{2,3} \\
\text{Re } V'_{2,2} &= \text{Re } V_{2,2} \\
\text{Im } V'_{2,2} &= -\text{Im } V_{2,2} - \frac{sqrt5}{2}\text{Im } V_{2,3} \\
\text{Re } V'_{2,3} &= \text{Re } V_{2,3} \\
\text{Im } V'_{2,3} &= \text{Im } V_{2,3}.
\end{aligned} \tag{A.25}$$

In a practical sense, these results are useful to compare the mathematical predictions to what is found experimentally. Essentially, the predicted ambiguous partner for a set of fit results in a given bin may be calculated in the following way. First, the results much be rotated in phase space such that the condition in Eq. A.23 is satisfied. Next, the ambiguous partner may be determined using Eq. A.25. Finally, this predicted solutions must be rotated back into the original phase convention. Now, the predicted ambiguous partner may be compared with the experimentally determined fit results. Such a comparison is shown in Fig. A.1.

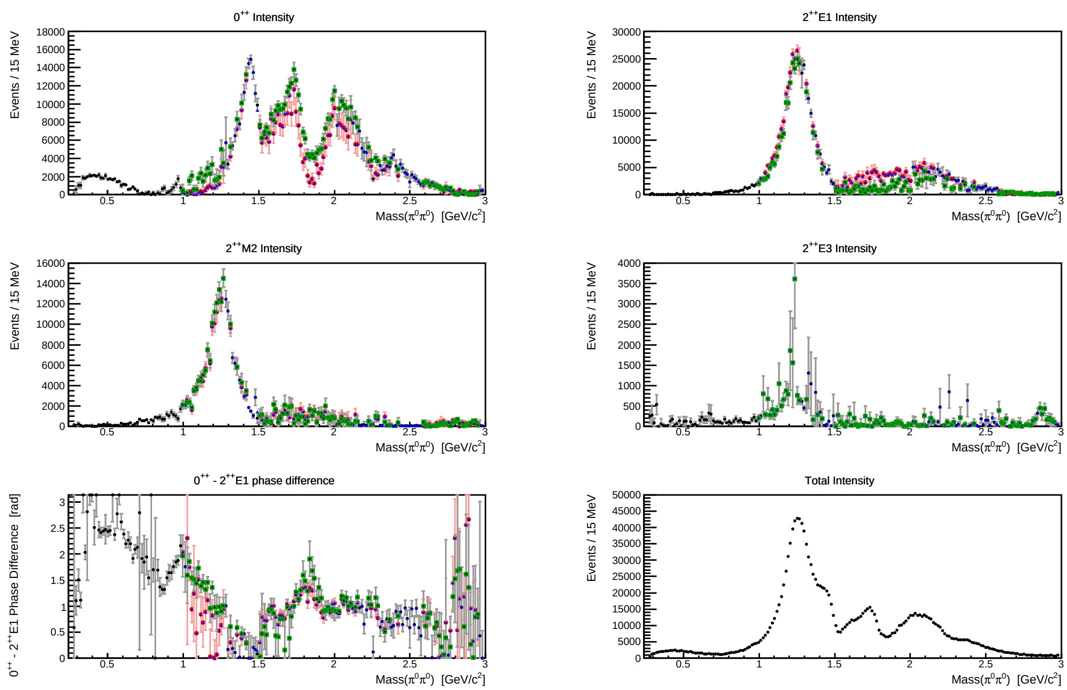

Figure A.1: The intensities for each amplitude as well as the phase differences between selected amplitudes are plotted here as a function of $\pi^0\pi^0$ invariant mass. The solid black markers give the results for one set of solutions while the empty red circles show the results for the ambiguous partner. The blue triangles show the predicted ambiguous partner to the solutions represented by the black markers. Similarly, the green squares predict the partners of the open red circle solutions. The fit results are consistent with the prediction.

Appendix B

Input-Output Study

In order to test the efficacy of the fitting machinery to predict the correct intensity distributions, a study was performed in which exclusive MC samples were fitted with the same procedure as the data. The results of the fit may then be compared to the generated information. Consistency between the generated and reconstructed values suggests that the fitting mechanism is effectively representing the data.

B.1 Single Resonance

Exclusive MC samples were generated with a single resonance in one of the amplitudes (0^{++} or 2^{++}) and fit with both resonances. This provides a means to test whether the fitting mechanism can properly predict an intensity of zero for an amplitude that contains no resonant structure. It is also a very clean method to test whether the true intensity for the amplitude can be determined. This process was repeated with an exclusive MC sample containing only a 0^{++} resonance and another sample containing only a 2^{++} resonance. In this context, a resonance in the 2^{++} wave implies that each component amplitude has a resonant structure (E1, M2, and E3).

One hundred statistically independent exclusive MC samples were generated for each set of resonances. Each of these samples was binned in terms of $\pi^0\pi^0$ invariant mass. Many fits were performed in each bin with randomized initial parameters. The best fit results (the ambiguous pair) were then compared to the generated information. One set of solutions gives an intensity distribution very similar to the generated information while the other set of solutions is significantly different than the generated information. The latter is the ambiguous partner to the selected set of solutions.

Pull distributions were generated for the set of solutions that more closely matches the generated information. Here the pull of a variable is defined as the difference between the experimentally measured information (x_i) and the true value of the variable (x) divided by the error on the measurement (σ_i):

$$p_i = \frac{x_i - x}{\sigma_i}. \tag{B.1}$$

The pull distributions are shown in Figure B.1-B.2. For each bin that has an appreciable intensity, the pull distribution includes the results from each MC sample. As a check on the efficacy of the fitting procedure, the number of events falling within ± 1 units of a pull value of zero is calculated. If the pull distributions are Gaussian distributed, as expected, the number of events in this window should be about 68.2% of the total distribution. The fraction of events within this window is overlaid in the figures below. These numbers appear reasonable.

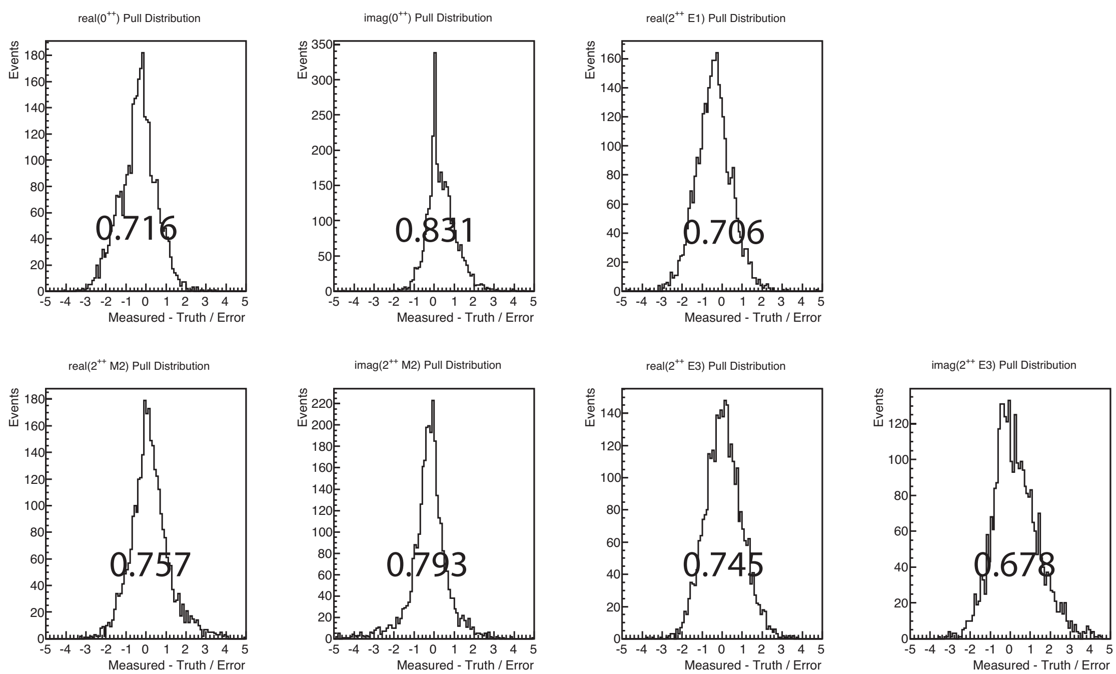

Figure B.1: The pull distributions for a set of exclusive MC samples with a single resonance in the 2^{++} wave, but fit with both the 0^{++} and 2^{++} waves, are shown here. The fraction of events within ± 1 of a pull value of zero are given for each distribution.

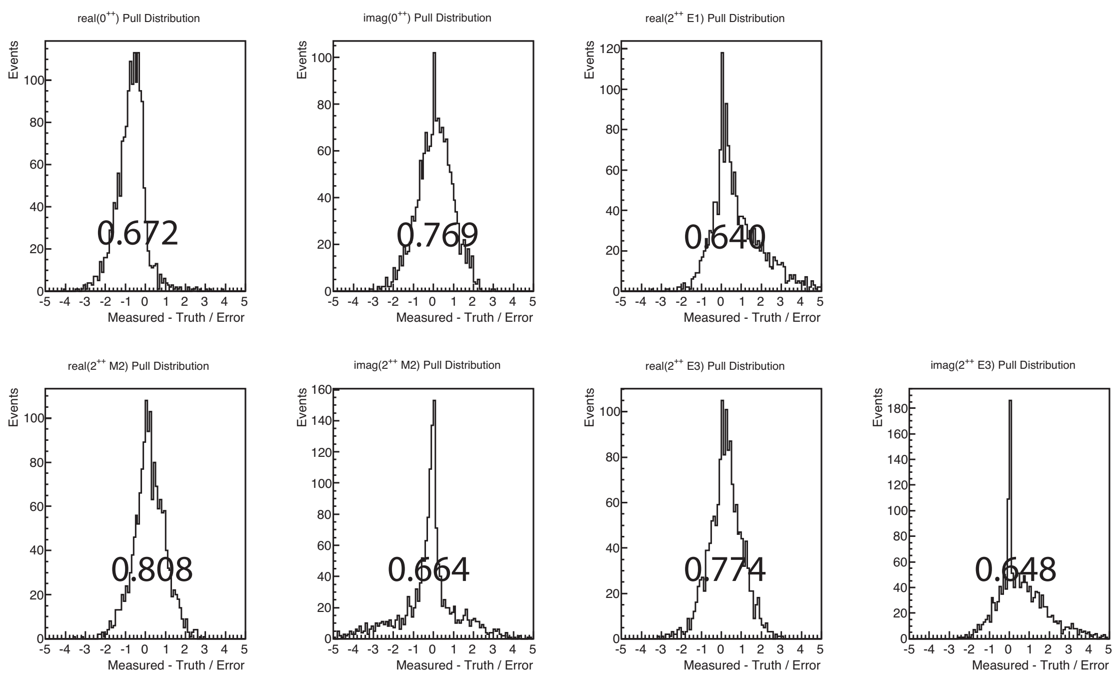

Figure B.2: The pull distributions for a set of exclusive MC samples with a single resonance in the 0^{++} wave, but fit with both the 0^{++} and 2^{++} waves, are shown here. The fraction of events within ± 1 of a pull value of zero are given for each distribution.

B.2 Two Resonances

In addition to the exclusive MC samples described above, a set of 100 statistically independent exclusive MC samples were generated with a resonance in each amplitude. These samples are fitted using the procedure described above. The results of these fits were similar to the simple case. The pull distributions are shown in Figure B.3.

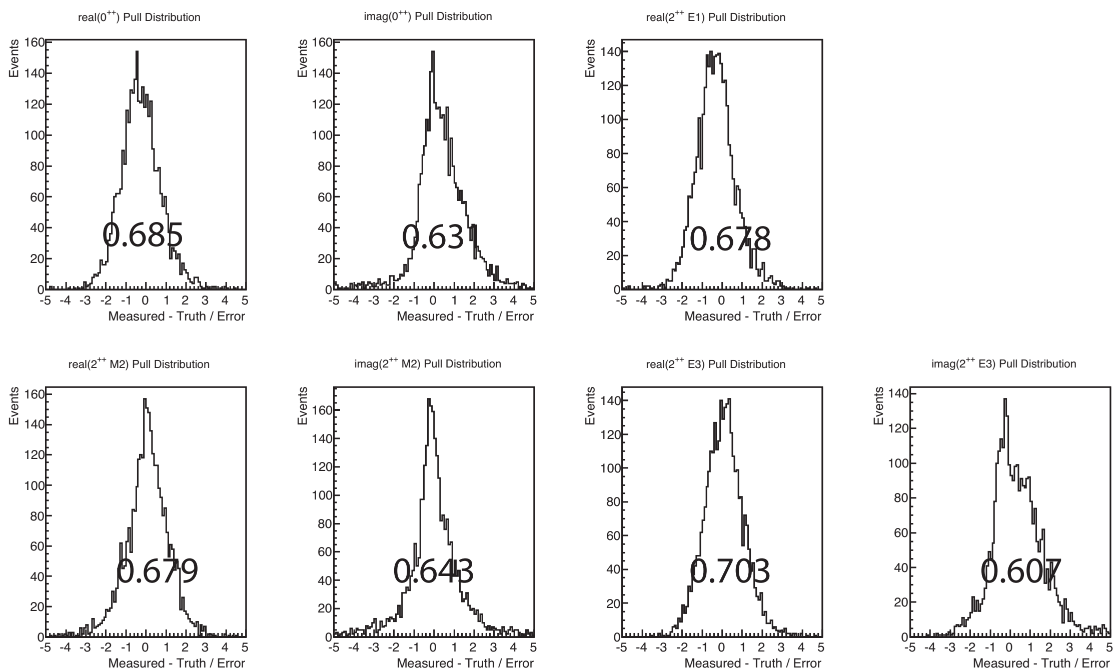

Figure B.3: The pull distributions for a set of exclusive MC samples with a resonance in each wave are shown here. The fraction of events within ± 1 of a pull value of zero are given for each distribution.

B.3 Full IO Study

Finally, an exclusive MC sample was generated according to the results of the mass dependent analysis. This sample was fit using the typical mass independent procedure and compared to the generated information (Figure B.4). The sample in Figure B.4

do not contain any effects due to the detector acceptance or resolution. In addition to this study, the MC events were sent through a detector simulation to add the effects of detector acceptance and resolution. This reconstructed MC sample was also fit in the typical manner. The results are shown in Figure B.5.

For each case, with and without detector acceptance and resolutions effects, the results of the mass independent fit are consistent with the generated information. The error bars are significantly larger for the case of actual acceptance and resolution effects. Based on this study, the fitting procedure appears to give a valid representation of the data sample.

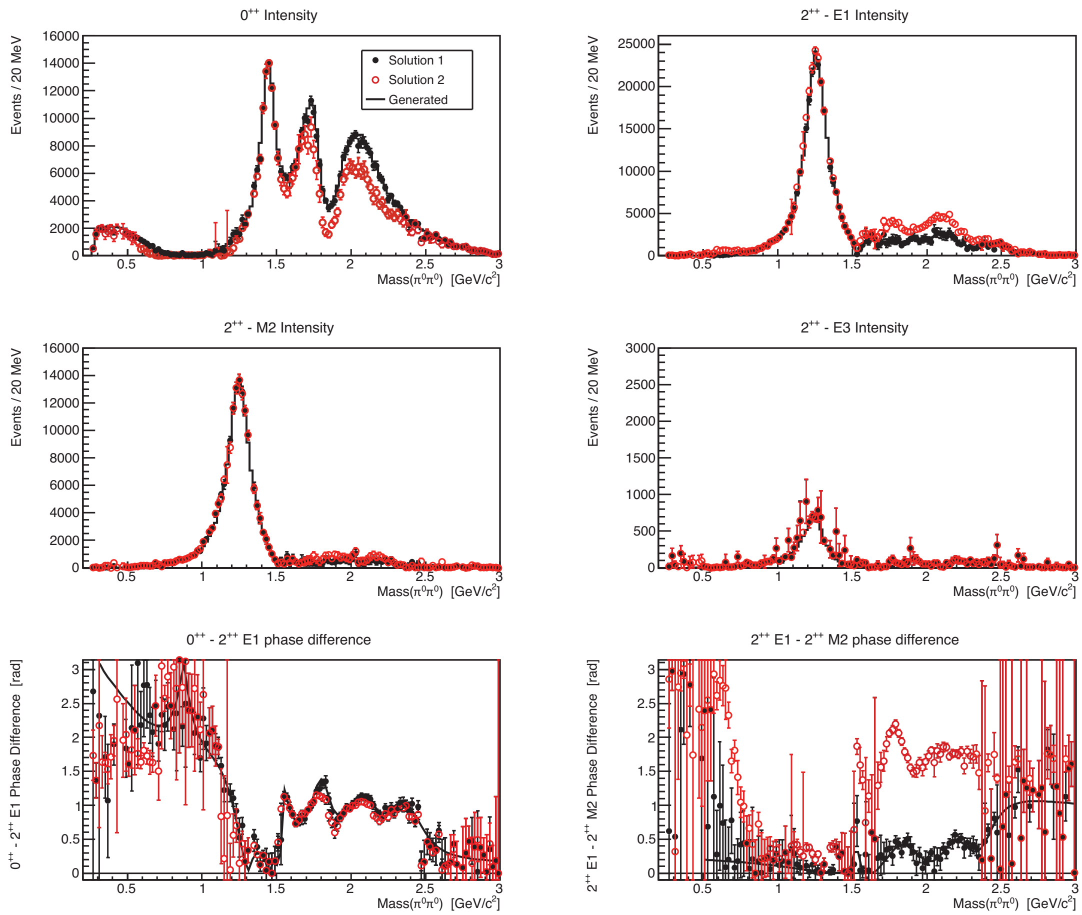

Figure B.4: These plots show the results of fits to an exclusive MC sample that closely resembles the data. The black markers give one set of results, while the red markers show the ambiguous partner. The black histogram depicts the generated distribution. This sample has perfect detector acceptance and resolution.

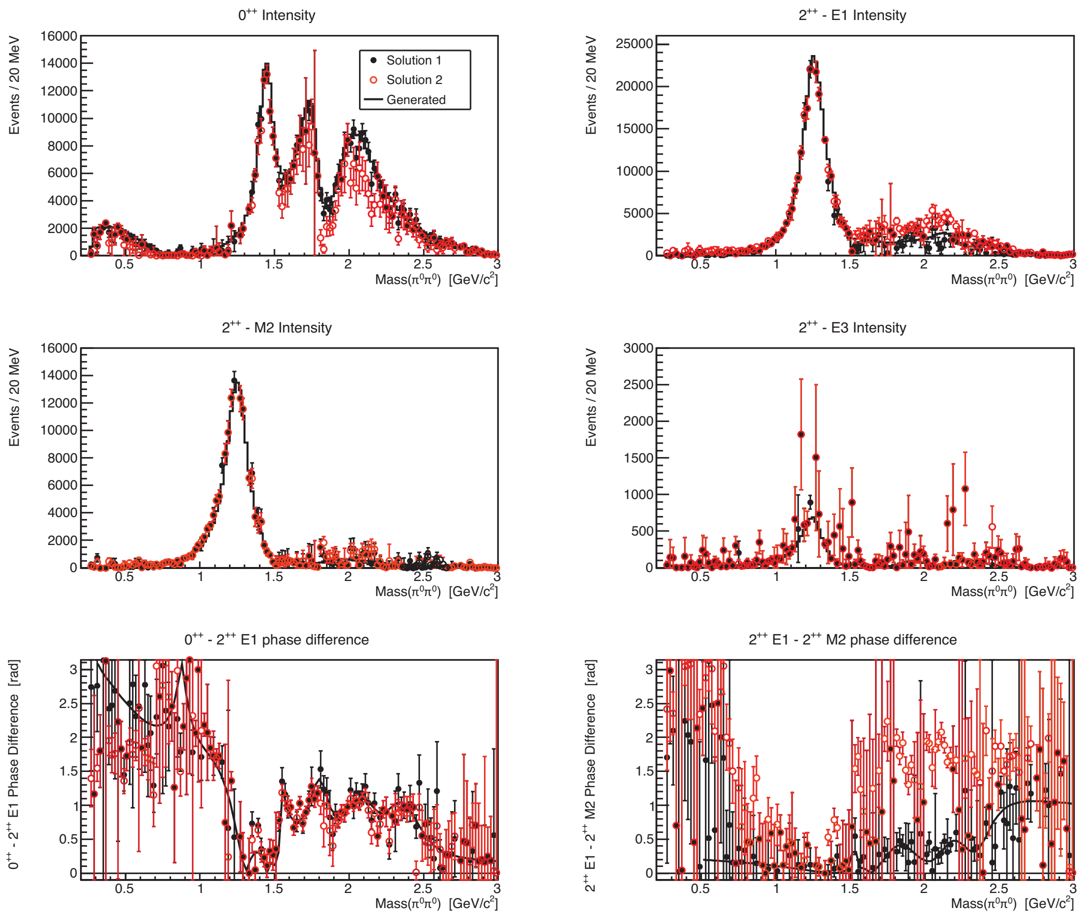

Figure B.5: These plots show the results of fits to an exclusive MC sample that closely resembles the data. The black markers give one set of results, while the red markers show the ambiguous partner. The black histogram depicts the generated distribution. This sample has actual detector acceptance and resolution.

Appendix C

Photon Detection Efficiency

Analyses at BESIII with multiple final state photons, such as J/ψ and ψ' decays to $\gamma\pi^0\pi^0$, require good knowledge of the photon detection efficiency of the BESIII detector. In particular, analyses like these are likely to have significant systematic errors from photon reconstruction effects. It is therefore important to possess an accurate measurement of the systematic uncertainty due to the photon detection efficiency. This efficiency is studied by calculating the difference in the expected number of photons and the number of photons that are actually detected.

The photon detection efficiency of the BESIII detector is studied using a sample of $J/\psi \to \pi^+\pi^-\pi^0$ events, where the π^0 decays into two photons. One of these final state photons is reconstructed, along with the two charged tracks, while the other photon is left as a missing particle in the event. This information can then be used to determine the region in the detector where the missing photon is expected. By retaining the reconstruction information for each additional photon in the event, it is possible to calculate the photon detection efficiency by taking the ratio of the number of photons which are detected in this region to the number that are expected. The number of detected and expected photons are determined by fits to the two photon invariant mass distributions.

The systematic error due to photon reconstruction is determined by investigating the differences between the photon detection efficiencies for the inclusive MC sample and the data. The inclusive MC sample consists of 225×10^6 J/ψ events, which are reconstructed using BOSS version 6.6.4. Two sets of data were analyzed. These include the older BESIII data set of $(225 \pm 2.8) \times 10^6$ J/ψ events, which are also reconstructed with BOSS version 6.6.4, and the new BESIII data set of approximately 1086×10^6 J/ψ events, which are reconstructed with the same BOSS version. The combined data set contains $(1.3106 \pm 0.0072) \times 10^9$ J/ψ decays. To justify the use of the older inclusive MC sample, two sets of exclusive MC were generated, one each for the run conditions of the old and new J/ψ data sets. The photon detection efficiencies determined from these two exclusive MC samples are consistent, suggesting that it is appropriate to use the inclusive MC sample in comparison with the new data set.

C.1 Event Selection

The data selection begins by requiring each event to have two oppositely charged tracks and at least one good photon. A good photon has an energy greater than 25 (50) MeV in the barrel (endcap) of the detector. If an event has more than one good photon, each combination of $\gamma\pi^+\pi^-$ is reconstructed. In this way, each photon from the π^0 is used in the calculation of the photon detection efficiency, effectively doubling the statistics of the sample. A 1C kinematic fit constrains the missing 4-momentum for each event to be a photon (have a mass of zero). This kinematically fitted missing photon is used to identify the region in the EMC in which the real photon is expected to be found. The reconstruction information for each additional photon in the event is retained in order to search for a candidate shower in the region of interest. The $\gamma\gamma$ invariant mass distribution is shown in Fig. C.1 before any additional selection criteria are applied.

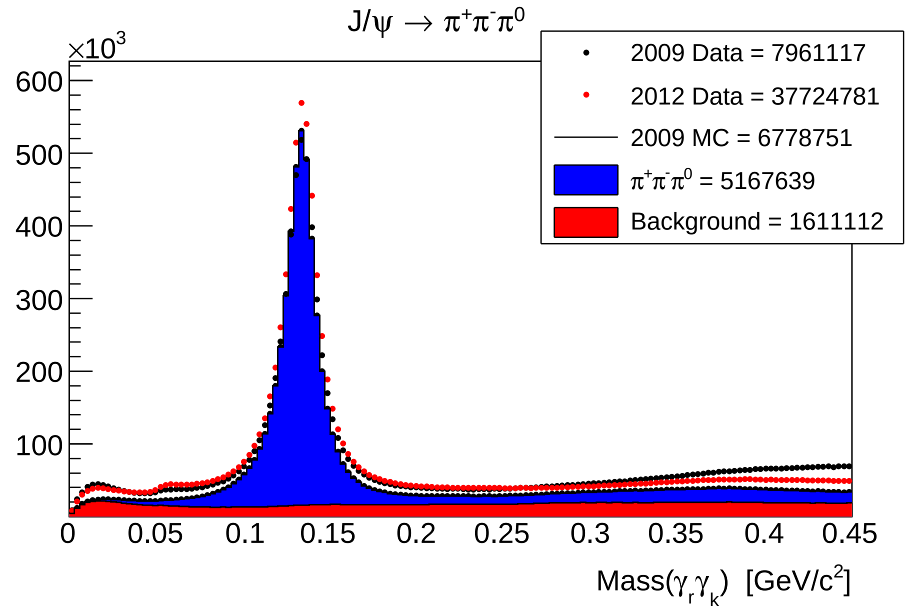

Figure C.1: The two photon invariant mass distribution is shown here after minimal selection criteria. Significant backgrounds include $J/\psi \to \mu^+\mu^-$, $J/\psi \to e^+e^-$, and $J/\psi \to \gamma\pi^+\pi^-$ as well as final states with extra π^0s and/or photons.

Each combination of $\gamma\pi^+\pi^-$ plus a missing photon must pass a series of additional selection criteria, which are designed to reduce backgrounds and maximize the signal. Where applicable, these criteria are also designed to match the typical reconstruction criteria. For example, the restriction on the opening angle of a photon with respect to a charged track matches the restriction that is applied by the BOSS reconstruction code. The charged tracks must satisfy a very loose restriction on the PID (the probability to be a pion must be greater than 10^{-5}). The largest backgrounds include $J/\psi \to \mu^+\mu^-$, $J/\psi \to e^+e^-$, and $J/\psi \to \gamma\pi^+\pi^-$ as well as final states with extra π^0s and/or photons ($J/\psi \to \pi^+\pi^-\pi^0\pi^0$ or $\gamma\pi^+\pi^-\pi^0$ for example). A large amount of background also comes from combinatoric effects. Signal events in which a fake photon is used as the reconstructed photon produce a $\gamma\gamma$ invariant mass which should not peak in the π^0 mass range.

The χ^2 from the 1C kinematic fit is required to be less than 6.3. This restriction eliminates a large portion of the background events with extra π^0s. The $\mu^+\mu^-$ and e^+e^- backgrounds can be greatly reduced by restricting the opening angle between the reconstructed photon and the nearest charged track to be greater than 20 degrees. This restriction is also applied to the kinematically fitted missing photon. In order to further reduce $J/\psi \to \mu^+\mu^-$ and $J/\psi \to e^+e^-$ backgrounds, the invariant mass of the reconstructed photon plus the two charged tracks is required to be less than $3GeV/c^2$. This quantity is also required to be greater than $1GeV/c^2$ in order to reduce a large background from $J/\psi \to \gamma\eta'$, where the η' decays to $gamma\pi^+\pi^-$. Other radiative decays of the J/ψ are reduced by restricting the energy of the reconstructed photon to be less than $1.36GeV$. Finally, to remove backgrounds from fake photons, the energy of the reconstructed photon is required to be greater than 0.1 GeV. The $\gamma\gamma$ invariant mass spectrum after all selection criteria is shown in Fig. C.2.

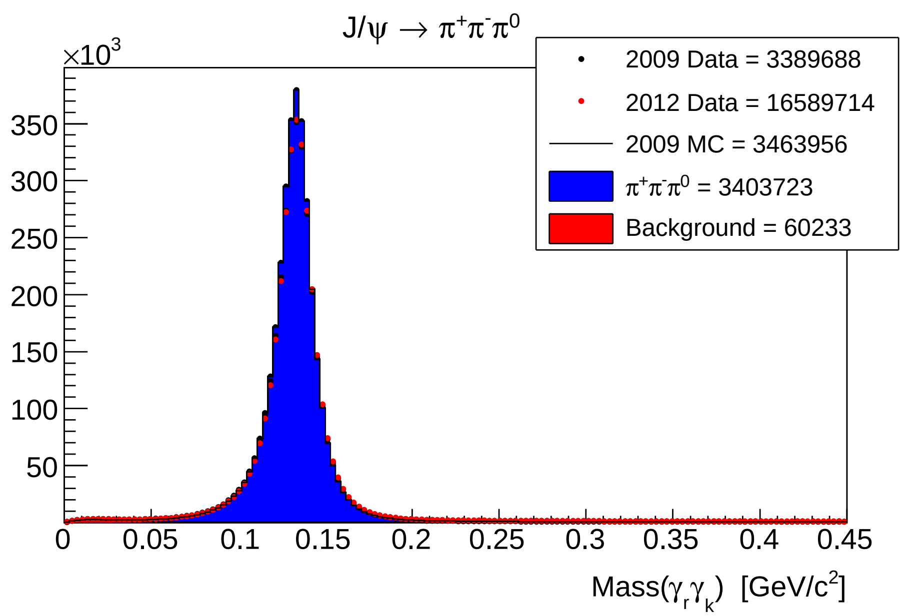

Figure C.2: The two photon invariant mass distribution is shown here after all selection criteria have been applied. The remaining background is less than 2% of the size of the signal.

The kinematically fitted missing photon is used to define an angular acceptance window in which to search for a candidate shower. If a candidate shower falls within the angular window, the photon is interpreted as having been detected, while if no candidate shower falls within the window, the missing photon is interpreted as being undetected.

The angular acceptance window is determined by fitting a two-dimensional Gaussian distribution to the difference between the angular distributions ($\cos(\theta)$ and ϕ) of the missing photon and the candidate shower. The width of the Gaussian function for each distribution is taken as one σ deviation for that variable. In order to account for resolution effects, which are more significant at lower photon energies, these windows are calculated in bins of the energy of the missing photon. A wide (10σ) acceptance window is defined for each energy bin. A sample angular distribution for one such window is shown in Fig. C.3.

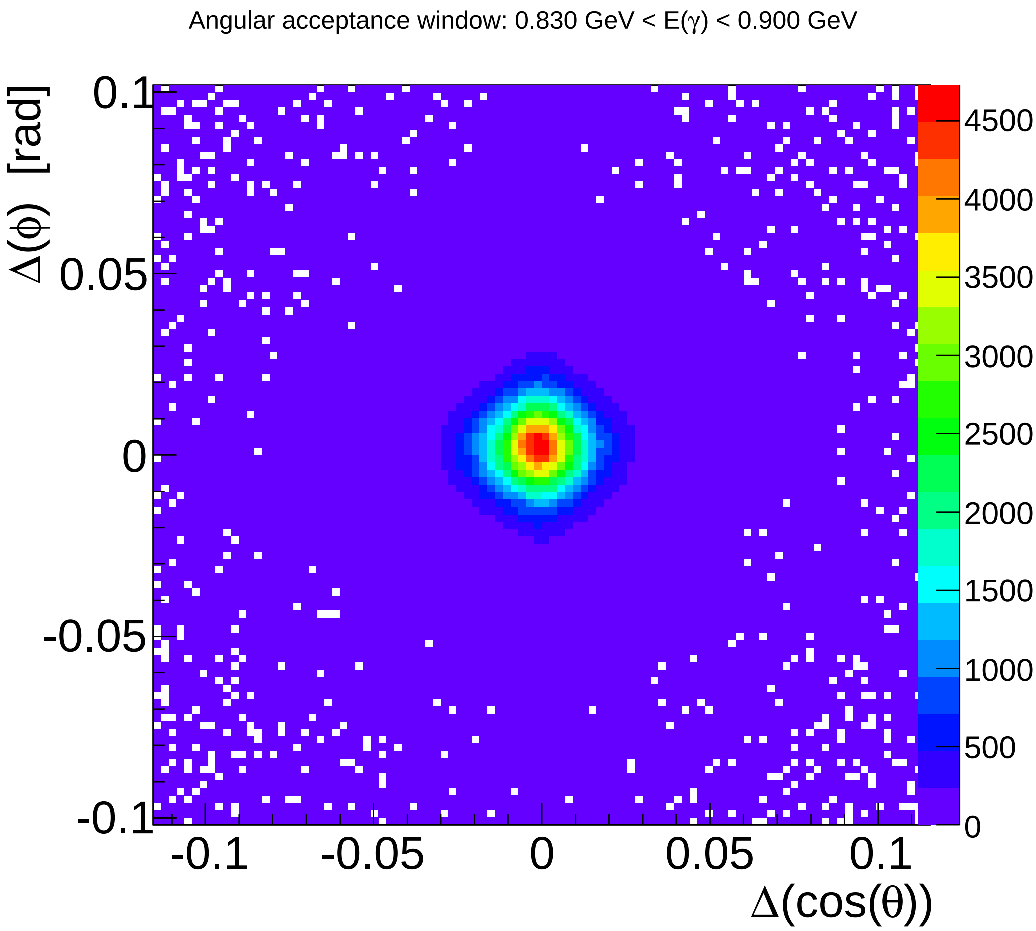

Figure C.3: For a single bin in energy, the kinematically defined angular acceptance window for the candidate shower is defined by a fit to the difference of the angular distributions of the kinematically fitted missing photon and each candidate shower. This distribution is fitted to a double Gaussian shape to determine the width of the angular window for each variable ($\cos(\theta)$ and ϕ).

C.2 Fitting Methods

Two complementary methods are used to calculate the photon detection efficiency. In each method, the expected number of missing photons (the denominator of the efficiency ratio) is determined by fitting the invariant mass distribution of the reconstructed photon plus the kinematically fitted missing photon. A clear peak is evident for the parent π^0 (Fig. C.4). The numerator of the efficiency ratio is determined by a similar fit, but only for events which have a candidate shower that is detected within the angular window defined by the missing photon. The background for each distribution is represented with a second order Chebychev polynomial function. The two methods differ in that one uses the missing photon itself in the $\gamma\gamma$ fit, while the other uses the real candidate shower. This necessarily changes the signal shape. Each method is described in more detail below.

C.2.1 Method 1

The first method calculates the number of detected photons using the invariant mass distribution of the reconstructed photon and the kinematically missing photon. This method has the benefit that the invariant mass distribution for events that have a real photon within the angular window is a subset of the same distribution that is used to calculated the expected number of photons. That is, the numerator of the efficiency ratio is a subset of the denominator. Method 1 may overestimate the photon detection efficiency, though, because a fake photon within the angular window may cause an event to be accepted (a form of background). For such events, the reconstructed and kinematically fitted photon pair may still have an invariant mass that falls in the π^0 mass range. In other words, an event which should have failed the acceptance test is accepted by chance.

C.2.2 Method 2

Method 2 fits the invariant mass distribution of the reconstructed photon with the candidate shower that falls within the angular window. That is, the invariant mass distribution for the numerator contains only photons that are actually detected. In this way, the two photon invariant mass distribution created by fake photons that fall within the angular window should not peak in the π^0 mass range. This method has a drawback in that it is necessary to calculate the expected and detected numbers of photons from two different distributions. This means that the two distributions may have different signal line shapes. Therefor, the distribution for the numerator of the photon detection efficiency is no longer a subset of the distribution for the denominator. In particular, the $\gamma\gamma$ invariant mass distribution using the kinematically fitted photon (denominator) has a resolution that is worse than the same distribution using only reconstructed photons (numerator).

Sample type	BOSS version	Method 1	Method 2
Inclusive MC	6.6.4	0.98201 ± 0.00007	0.983 ± 0.003
Old J/ψ data	6.6.4	0.98381 ± 0.00007	0.985 ± 0.007
New J/ψ data	6.6.3	0.98445 ± 0.00003	0.982 ± 0.002

Table C.1: This table gives the photon detection efficiency as calculated by global fits over all photon energies and angles.

C.3 Results

The $\gamma\gamma$ invariant mass distributions for method 1 are fitted by a double crystalball shape over a second order chebychev polynomial. Method 2 differs in that the denominator is fitted with a double crystalball shape and the numerator with a crystalball plus a Gaussian function. The results of global fits according to methods 1 and 2 are shown in Table C.1. Both methods 1 and 2 show good consistency between the inclusive MC sample and both of the data samples (Fig. C.5). The difference between data and MC is always less than 0.5%.

In order to check the stability of the results, the global fits were repeated after varying the background shape and angular acceptance window. To probe the effect of the shape of the background, the second order chebychev polynomial was replaced with a third order background. The angular acceptance window was loosened from 10σ to 15σ and 5σ in order to probe the effects of the uncertainty of the missing four momentum from the 1C kinematic fit. The differences between the photon detection efficiencies for the inclusive MC sample, old and new data sets for each of these variations are consistent with the best fit method (Table C.4). The difference between fits to the inclusive MC sample and the data sets for each method is shown in Fig. C.12.

C.3.1 Energy and Anglular Distributions

In addition to the global fits over all energies and angles, the $\gamma\gamma$ invariant mass distributions were also divided into bins of energy (Fig. C.6 and C.7) and $\cos(\theta)$ (Fig. C.8 and C.9) for the missing photon. Each bin in energy or angle is fitted as in the global fits. For each distribution, the results of the fits for data and MC samples are consistent. As a check on the global fits, the results of the fits in bins of angle and energy were combined to obtain a global value for the photon detection efficiency from these methods. The results are consistent with the values obtained from the global fits (Table C.2 and C.3).

It is important to note that the background due to misreconstructed signal events, in which a fake photon is used as either the reconstructed or missing photon, may artificially inflate the efficiency. Not only does this background exist in Method 1 (as expected), it also peaks near enough the π^0 peak in the numerator of Method 2 that it inflates the efficiency. This inflation of the efficiency appears in both the inclusive

MC sample and the data. Fake photon backgrounds exists primarily in the low $E_{(\gamma_k)}$ region and result in an inflated value for the detection efficiency as is evident in Fig. C.6. As the primary purpose of this study is to determine the systematic error due to differences between the modeled and actual detection efficiency and not the absolute efficiency itself, this effect does not pose a major problem (see Fig. C.6).

Sample type	BOSS version	Method 1	Method 2
Inclusive MC	6.6.4	0.98163 ± 0.00007	0.982 ± 0.006
Old J/ψ data	6.6.4	0.98243 ± 0.00007	0.980 ± 0.006
New J/ψ data	6.6.3	0.98188 ± 0.00003	0.979 ± 0.003

Table C.2: This table shows the combined results for the photon detection efficiency from fits in bins of photon energy.

Sample type	BOSS version	Method 1	Method 2
Inclusive MC	6.6.4	0.98246 ± 0.00007	0.982 ± 0.007
Old J/ψ data	6.6.4	0.98307 ± 0.00007	0.983 ± 0.006
New J/ψ data	6.6.3	0.98204 ± 0.00003	0.982 ± 0.002

Table C.3: This table shows the combined results for the photon detection efficiency from fits in bins of photon angle.

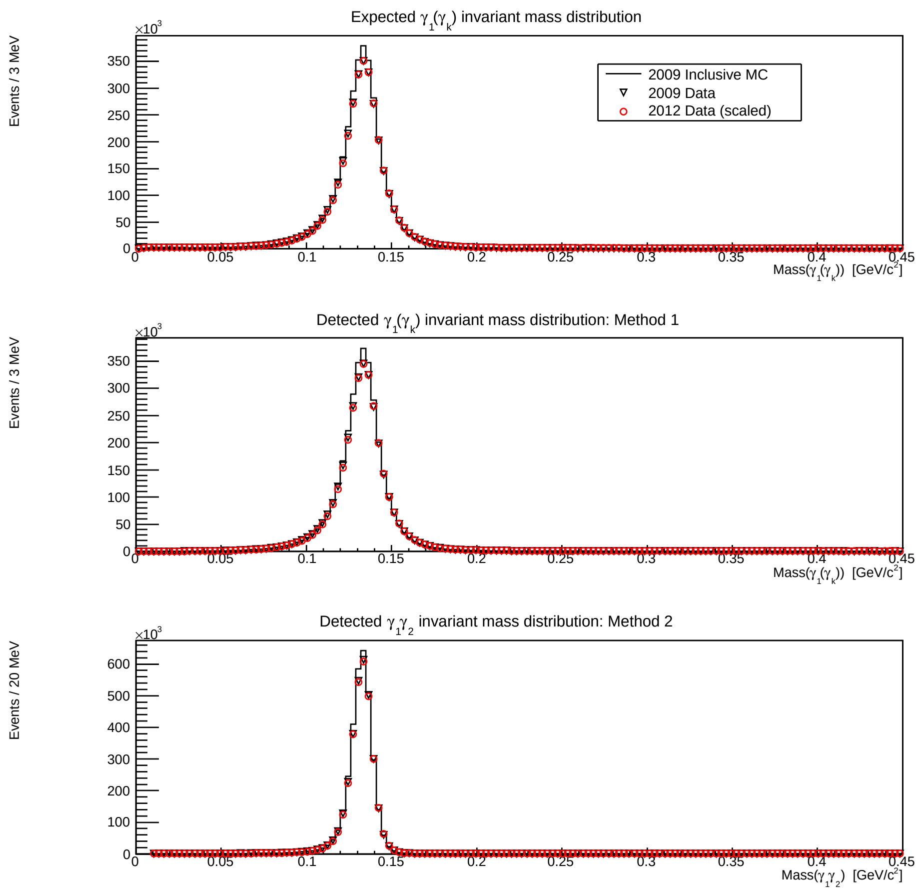

Figure C.4: These plots show a comparison of the two photon invariant mass distributions for the inclusive MC and data samples. In each plot, the black histogram shows the distribution for the inclusive MC, the red markers show this distribution for the old J/ψ data, and the green markers show the same for the new J/ψ data. Figure C.4(a) shows the invariant mass distribution of the reconstructed (γ_1) and missing (γ_k) photons before looking for the missing photon in the detector. Figures C.4(b) and C.4(c) show the accepted invariant mass distributions for methods 1 and 2 respectively.

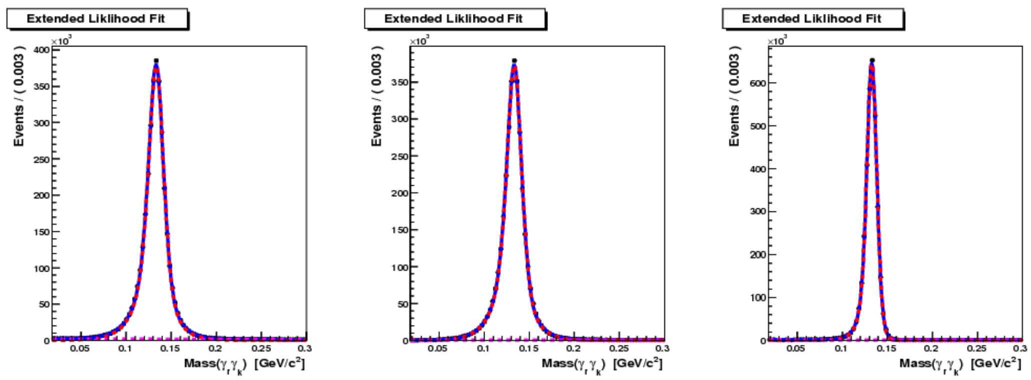

Figure C.5: These plots show the results of fits to the inclusive MC. The plot on the left shows the result of a fit to the full distribution of $\gamma\gamma$ invariant mass (the denominator of the photon detection efficiency). The dashed red line shows the Crystalball shape, while the dashed pink line is the polynomial background. The solid blue line shows the fitted line shape. The middle plot shows the result of a fit to the accepted distribution for method 1, while that for method 2 is shown in the plot on the right.

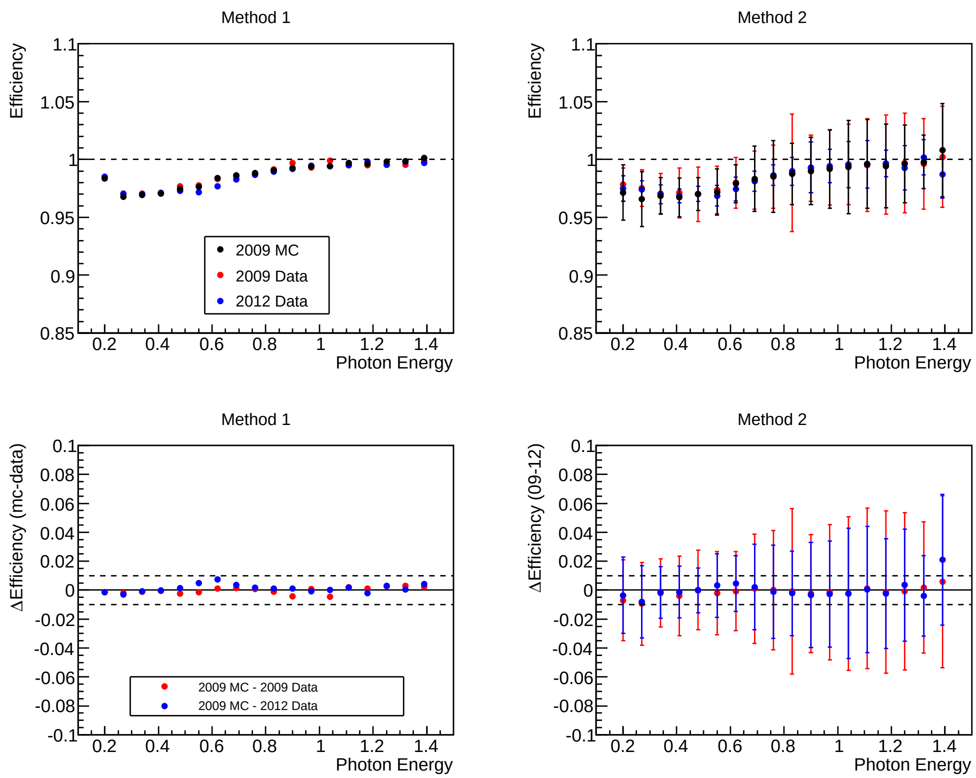

Figure C.6: These plots show the results of fits in each bin of photon energy. The photon detection efficiency for inclusive MC (black histogram), old J/ψ data (red markers) and new J/ψ data (green markers) are shown in the top two plots. The difference between the MC and the data is plotted in shown in the bottom two plots for the old (red) and new (green) data samples.

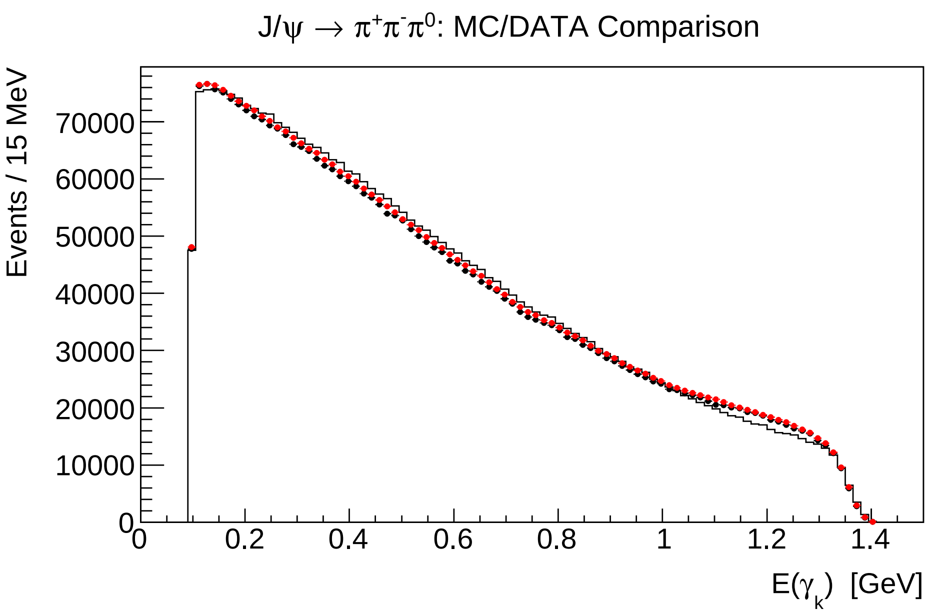

Figure C.7: This plot shows a comparison of the photon energy distributions for the inclusive MC and data samples. The black histogram shows the distribution for the inclusive MC, the red markers show this distribution for the old J/ψ data, and the green markers show the same for the new J/ψ data.

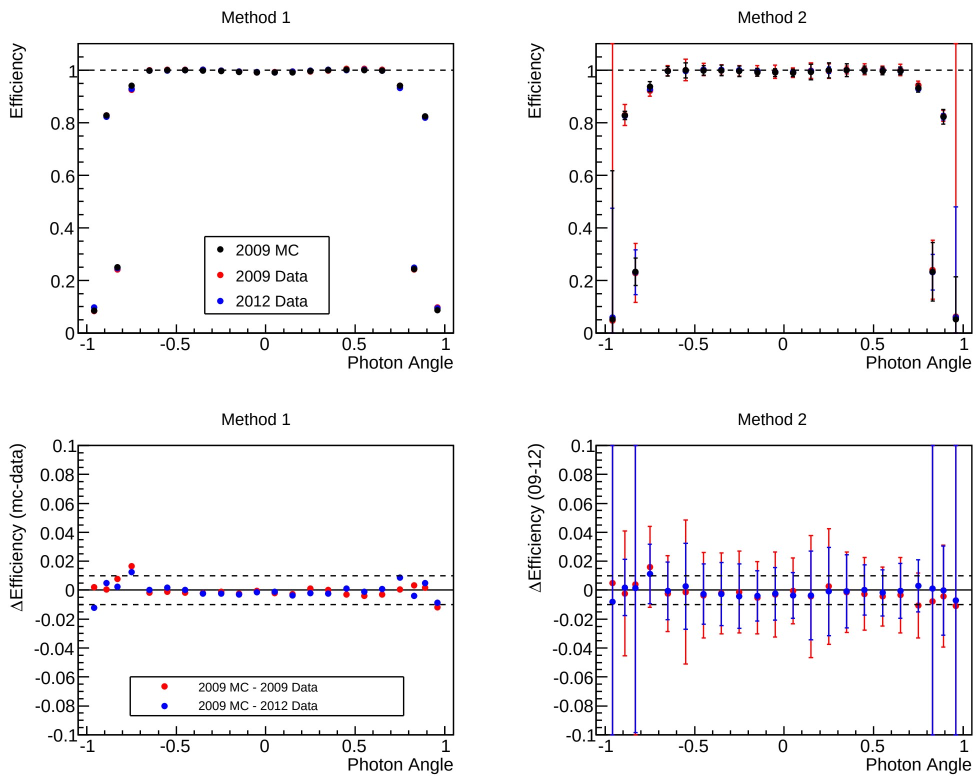

Figure C.8: These plots show the results of fits in each bin of photon angle. The photon detection efficiency for inclusive MC (black histogram), old J/ψ data (red markers) and new J/ψ data (green markers) are shown in the top two plots. The difference between the MC and the data is plotted in the bottom two plots for the old (red) and new (green) data samples.

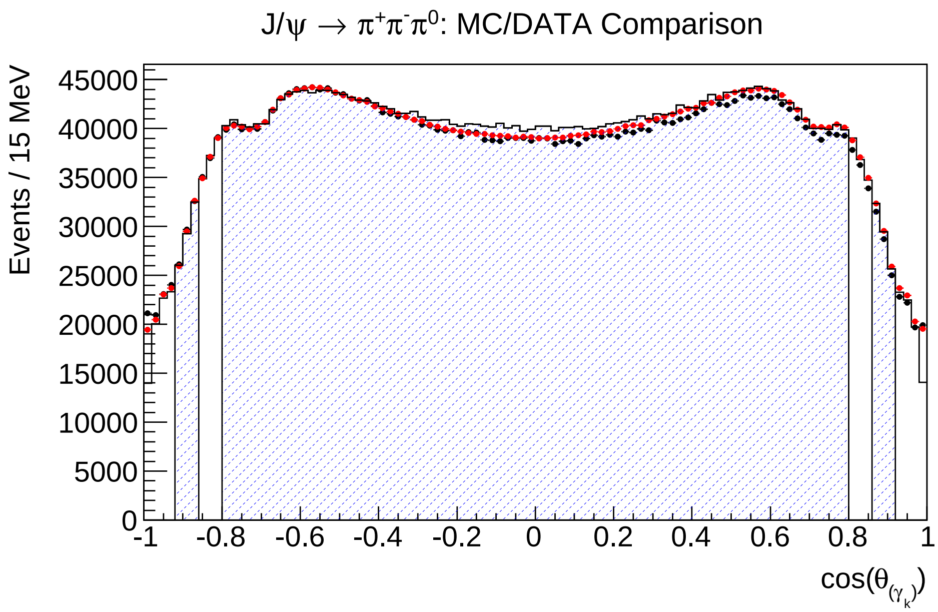

Figure C.9: This plot shows a comparison of the $\cos(\theta_\gamma)$ distributions for the inclusive MC and data samples. The black histogram shows the distribution for the inclusive MC, the red markers show this distribution for the old J/ψ data, and the green markers show the same for the new J/ψ data. The shaded region indicates the regions of the detector that are used for photon reconstruction. The open regions (including the beam line and the gap between the barrel and endcap of the EMC) are excluded in calculating the total photon detection efficiency.

C.3.2 MC Consistency Check

Due to the lack of an inclusive MC sample for comparison with the 2012 J/ψ data set, the 2009 inclusive MC sample of 225 M J/ψ decays was used in this study. To validate the use of this older MC sample, a MC consistency check was performed using exclusive MC samples generated with the run conditions of both the 2009 and 2012 J/ψ data sets. These MC samples were not used to determine the systematic error due to the photon detection efficiency because they do not contain the backgrounds that exist in the data and 2009 exclusive MC sample. Each MC sample is divided into bins of energy and angle and fit as described above. The results of such fits show that the MC with different run conditions are consistent. This suggests that the use of the 2009 MC sample is appropriate for this study.

Sample type	BOSS version	Method 1	Method 2
Nominal results			
Inclusive MC	6.6.4	0.98201 ± 0.00007	0.983 ± 0.003
Old J/ψ data	6.6.4	0.98381 ± 0.00007	0.985 ± 0.007
New J/ψ data	6.6.3	0.98445 ± 0.00003	0.982 ± 0.002
3rd order background			
Inclusive MC	6.6.4	0.97765 ± 0.00008	0.983 ± 0.006
Old J/ψ data	6.6.4	0.98120 ± 0.00007	0.982 ± 0.005
New J/ψ data	6.6.3	0.97896 ± 0.00004	0.983 ± 0.003
Loose (15σ) window			
Inclusive MC	6.6.4	0.98450 ± 0.00007	0.987 ± 0.003
Old J/ψ data	6.6.4	0.98531 ± 0.00007	0.990 ± 0.003
New J/ψ data	6.6.3	0.98394 ± 0.00003	0.990 ± 0.001
Tight (5σ) window			
Inclusive MC	6.6.4	0.96636 ± 0.00010	0.966 ± 0.001
Old J/ψ data	6.6.4	0.96620 ± 0.00010	0.965 ± 0.003
New J/ψ data	6.6.3	0.96435 ± 0.00005	0.9650 ± 0.0004

Table C.4: This table gives the results for the photon detection efficiency for fits with different background shapes and angular acceptance windows.

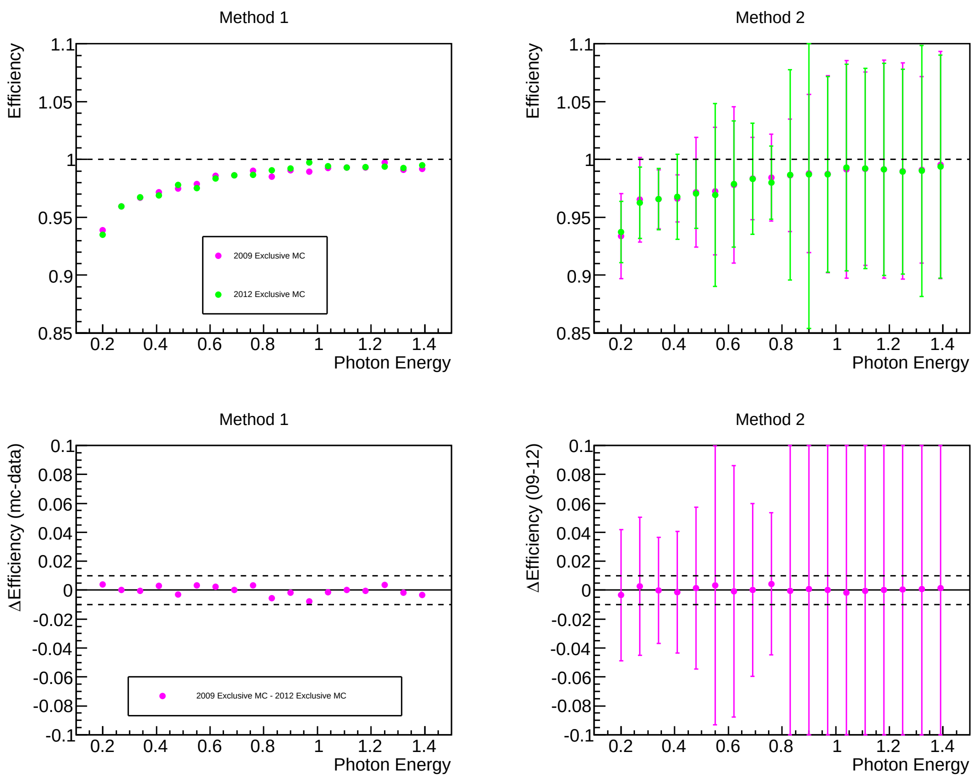

Figure C.10: These plots show the results of fits in each bin of photon energy. The photon detection efficiency for inclusive MC (black histogram), old J/ψ data (red markers) and new J/ψ data (green markers) are shown in the top two plots. The difference between the MC and the data is plotted in the bottom two plots for the old (red) and new (green) data samples.

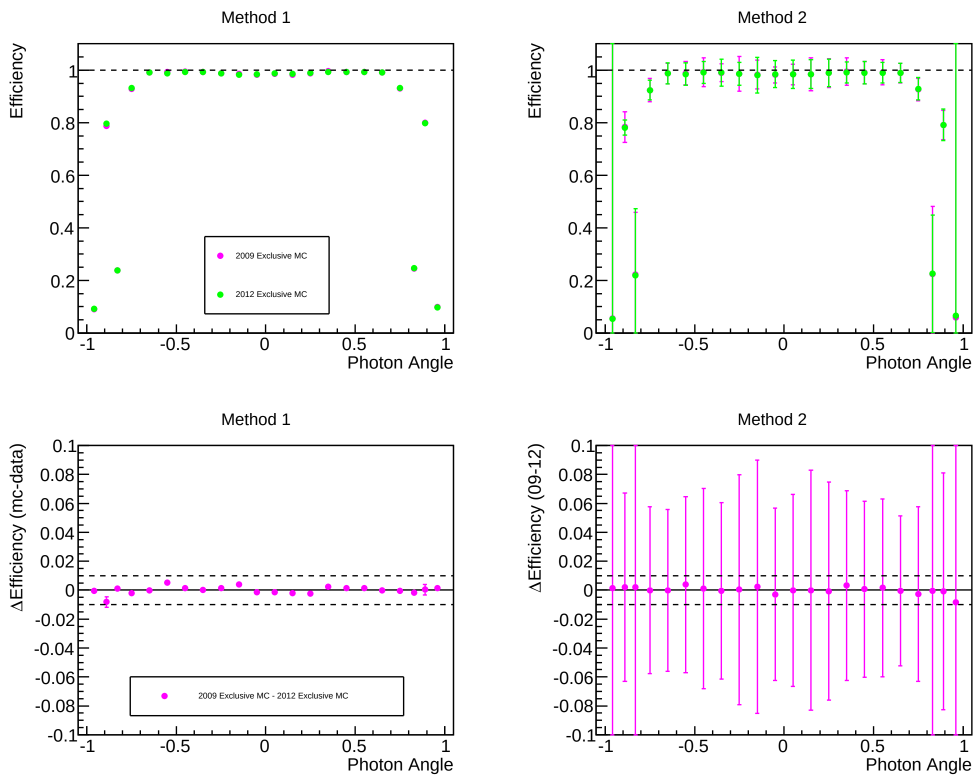

Figure C.11: These plots show the results of fits in each bin of photon angle. The photon detection efficiency for inclusive MC (black histogram), old J/ψ data (red markers) and new J/ψ data (green markers) are shown in the top two plots. The difference between the MC and the data is plotted in the bottom two plots for the old (red) and new (green) data samples.

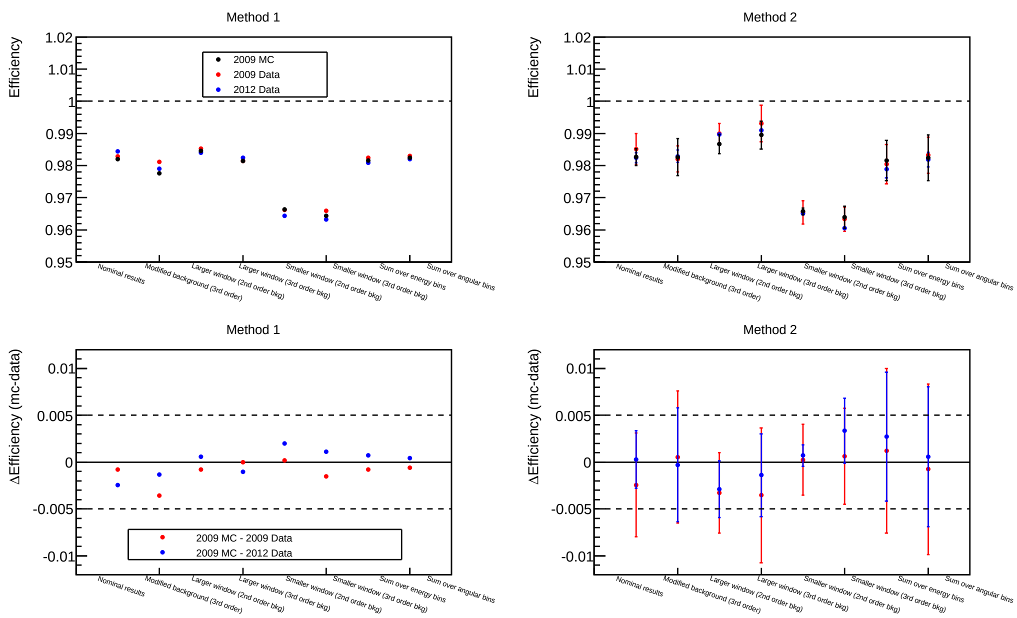

Figure C.12: These plots show a comparison of the photon energy distributions for the inclusive MC and data samples. The black histogram shows the distribution for the inclusive MC sample, the red markers show this distribution for the old J/ψ data, and the green markers show the same for the new J/ψ data.

C.4 Conclusions

This study of the BESIII detector shows that differences in the photon detection efficiency between the inclusive MC sample and the data are less than 0.5%. This is a significant improvement upon the commonly referenced 1.0% systematic error from a previous study at BESIII. In addition to the global analysis over all energies and angles, the photon detection efficiency is also analyzed in bins of photon energy and angle. The detection efficiency for these distributions is consistent between the MC sample and the data. The total photon detection efficiency from the MC sample and the data, summed over these energy and angle bins, are consistent within 0.5%.